THE MAGELLANIC CORONA AND ITS ROLE IN THE EVOLUTION OF THE MAGELLANIC STREAM

by

SCOTT LUCCHINI

A dissertation submitted in partial fulfillment of
the requirements for the degree of

DOCTOR OF PHILOSOPHY
(PHYSICS)

at the

UNIVERSITY OF WISCONSIN-MADISON
2023

Date of final oral examination: June 5, 2023

The dissertation is approved by the following members of the Final Oral Committee:
- Elena D'Onghia, Professor, Astronomy
- Keith Bechtol, Assistant Professor, Physics
- Robert A. Benjamin, Professor, Astronomy
- Peter Timbie, Professor, Physics

Abstract

The Magellanic System is the perfect opportunity to explore many aspects of astrophysics right on our Galaxy's doorstep. Two dwarf galaxies, the Large and Small Magellanic Clouds (LMC, SMC) are interacting with each other and with the Milky Way to form the Magellanic Stream, a multiphase gaseous tail of intertwined filaments trailing behind the Clouds. Here we can study galactic dynamics, gas dynamics, turbulent processes, gas cooling and mixing, metal transport, and more. However, there are two outstanding mysteries as to how the Magellanic System came to be – its large amount of ionized gas, and the high mass of the LMC. To solve both these discrepancies simultaneously, we introduce the Magellanic Corona. This warm, ionized circumgalactic medium should surround the LMC as it interacts with the SMC and the Milky Way. Throughout my thesis work, I have used high-resolution numerical simulations of the formation of the Magellanic Stream to test this new model including the Magellanic Corona. We can account for both the neutral and ionized components of the Stream while also reproducing the present-day positions and velocities of the LMC and the SMC. We have also found a new family of orbital histories for the Clouds that result in the neutral Stream being significantly closer than previous models predicted. The Magellanic Corona seems to be the key to the formation of the Magellanic Stream and has many implications throughout galaxy evolution.

ACKNOWLEDGEMENTS

As much as receiving my PhD has been an incredible scientific venture, the past six years have marked many personal milestones as well. Here I hope to express my gratitude to those who have made my time in Madison particularly meaningful.

First and foremost, I must thank my advisor, Elena D'Onghia. I am so glad that you accepted me as your student. I have learned so much not only about numerical simulations and galactic dynamics, but also about academia and life as a scientist. I am especially grateful for your flexibility and understanding as I worked to balance my academic pursuits with family life.

Additionally, I certainly would not have ended up where I am today without the encouragement and mentorship I received from Andy Fox. Thank you Andy, for consistently being the voice of reason in our meetings. Your invaluable guidance and expertise has been instrumental in shaping my research direction.

My early years in the physics department, taking classes and teaching, were largely shaped by three individuals – Jeff Schmidt, Lisa Everett, and Ben Spike. Thank you Jeff, for showing me the power of theoretical physics and instilling in me a desire to never stop reading textbooks. Even if your dynamics problem sets took me 20 hours to complete. Thank you Lisa, for providing the support that I needed at the beginning of the program, and for advocating for me as I explored research opportunities within the department. And thank you Ben, for providing me not only with excellent teaching opportunities, but also for showing me the tools of modern physics instruction (so much more than chalk and a blackboard).

And to my friends – Chad Bustard, Alex Pizzuto, Rob Morgan, and Rachel McClure. Thank you Chad, for all of our coffee shop "group meetings" in the early days of my work with Elena. Alex and Rob, thank you for your friendship through the highs and lows: long hours trudging through

problem sets, and the wonderful afternoons getting pints at the Olbrich Biergarten. And thank you Rachel, for welcoming me into the astronomy department and making Elena's growing group feel like a real family.

Finally, I would not be who I am without my family. Thank you to my parents, Pete and Lynn, who have always done everything in their power to support me and help me succeed. Thank you to my sister, Sara, for your camaraderie and friendship over the years.

And to my wife, Amanda – none of this would have been possible without your unwavering support and love. Science may be my passion, but our family is my purpose on this planet. I am grateful for all that we have built together.

Contents

List of Figures

List of Tables

CHAPTER 1

INTRODUCTION

Looking at a tiny patch of black sky, the *Hubble Space Telescope's* "deep field" images revealed thousands of galaxies across cosmic time (Williams, 1996). For the first time, scientists were able to see what galaxies looked like very early on in the universe and the huge variety in their properties and appearances blew open the field of galaxy formation and evolution. More recently, *Hubble*'s "ultra deep field" in 2006, and the launch of JWST in 2021 have given us more incredible insights in to galaxies in the early universe (e.g. Ferreira et al. 2022). Through these observational data, theoretical modeling, and computer simulations, astronomers have managed to put together a cohesive picture of a galaxy's life cycle – from the Big Bang to now. Subtle overdensities of dark matter in the early universe gradually coalese and grow, forming halos of dark matter that attract and accumulate gas. This continues for billions of years and through this process of gas and dark matter accretion, galaxies can grow, form stars, and become the beautiful structures that we see in the night sky today. One specific avenue for gas accretion is through merger events in which two or more galaxies violently come together and coalesce. The *Hubble Space Telescope* has photographed beautiful ongoing mergers in other galaxies, and computer simulations have also shown us that this is an effective method for gas acquisition in galaxy evolution.

Our own Milky Way (also referred to as "the Galaxy") is in fact undergoing a gas-rich merger event right now. Looking up into the night sky (from the Southern hemisphere), you may be able to barely see two smudges off to the side of the Milky Way's brilliant disk. These smudges are two of our most significant galactic neighbors, the Large and Small Magellanic Clouds (LMC, SMC), two "dwarf galaxies" that have just recently approached our Galaxy. If instead of looking at the stars, we were to use a radio telescope to observe the cold gas in the night sky, we would see something much more striking – a huge tail of gas trailing behind the Magellanic Clouds covering over 200 degrees on the sky, dubbed the Magellanic Stream (or "the Stream"). Figure 1.1 shows how the Stream would appear overlaid onto a photograph of the Milky Way disk and Magellanic Clouds taken in Australia.

1.1 The Magellanic System

The Magellanic System consists of the the two dwarf galaxies, the Large and Small Magellanic Clouds, the Trailing Stream extending behind the Clouds, as well as the Leading Arm, and the

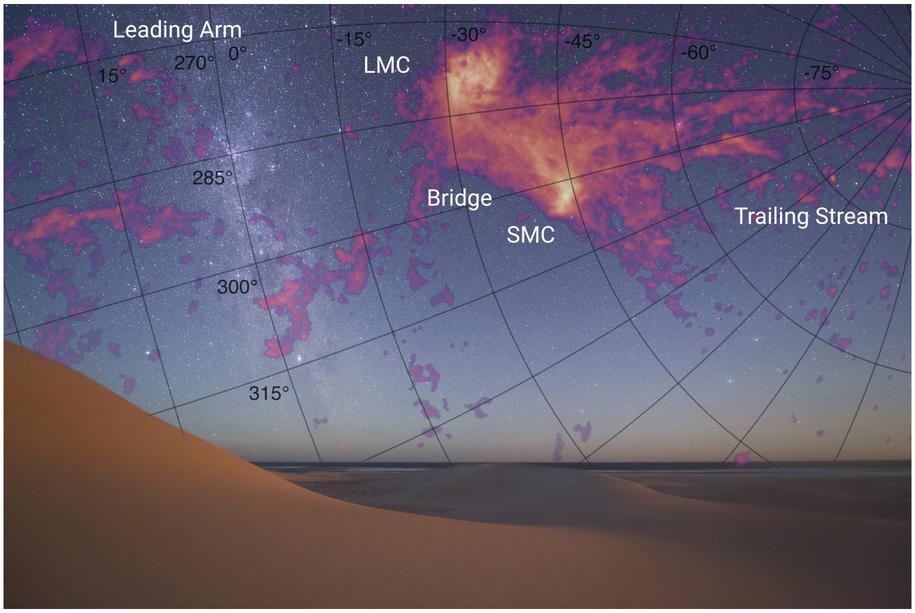

Figure 1.1: The Magellanic System as it would appear on the sky. The background is a photograph taken by Colin Legg in Australia showing the Milky Way disk on the left with the Magellanic Clouds at the center. The purple and orange overlay shows the 21 cm neutral hydrogen emission from the Magellanic System with a grid in Galactic coordinates. The LMC, Bridge, and SMC are labelled in the center of the image. The Clouds are travelling to the left on the sky and we can see a very extended tail of gas extending behind the Clouds in their orbits, labelled "Trailing Stream." There is also some material out ahead of the LMC and the SMC, labelled "Leading Arm." This image only shows $\sim$ 50% of the length of the Trailing Stream which covers over 100° on the sky in total.

Magellanic Bridge. Figure 1.1 is labelled with these different components. Many features of the galaxies show evidence of past interactions. For example, the LMC contains a lopsided bar and a single spiral arm (D'Onghia and Fox, 2016). There are also numerous star forming regions including 30 Doradus which hosts massive, very young star clusters (Crowther et al., 2016; Kalari et al., 2022). The SMC is a dwarf irregular galaxy with a cigar-shaped structure elongated along the line of sight (Subramanian and Subramaniam, 2012; Graczyk et al., 2020) with two distinct velocity components (Murray et al., 2019). The gas and stellar populations exhibit different morphologies, possibly due to the intense interactions between the SMC and the LMC in the past (Stanimirović et al., 2004; Zaritsky et al., 2000; Cioni et al., 2000). The LMC has a stellar mass of 3.2×10^9 $M_\odot$ (van der Marel et al., 2009) and a neutral gas mass of 4.4×10^8 $M_\odot$ (Brüns et al., 2005). The SMC's stellar and gas masses are 3.1×10^8 $M_\odot$ (Stanimirović et al., 2004) and 4.0×10^8 $M_\odot$ (Brüns et al., 2005), respectively.

The Magellanic Stream is the largest extragalactic gaseous structure in our night sky. It is an extended network of interwoven clumpy filaments of gas that originate from within the Magellanic Clouds. Originally detected in 21 cm observations of neutral hydrogen (Mathewson et al., 1974), these H I maps still provide a wealth of information on the morphology and velocity of the Stream. Modern all-sky H I surveys are able to resolve structures as small as ~ 250 pc (16.2' resolution at 55 kpc; Westmeier, 2018) with resolution down to tens of parsecs in upcoming data (GASKAP; Pingel et al., 2022). In addition to hundreds of head-tail clouds and intricate turbulent structures (For et al., 2014), these data have shown that there are two spatially and kinematically distinct intertwined filaments in the Trailing Stream (Cohen, 1982; Morras, 1983; Nidever et al., 2008).

Moreover, absorption line spectroscopy studies have characterized the chemical composition and ionization state of the Stream along dozens of sightlines (Lu et al., 1994; Gibson et al., 2000; Sembach et al., 2003; Fox et al., 2010; Fox et al., 2013; Richter et al., 2013; Fox et al., 2014). By analyzing the spectrum of a background source, we can detect very low-density gas that exists between us and the source based on how much light has been absorbed since it was emitted. Spectroscopy gives us the intensity of detected light as a function of frequency, so we are able to identify what chemical elements exist along our line of sight by cross-matching the frequencies of absorbed light with known atomic transitions. In the case of the Magellanic System, this has resulted in two important discoveries: (1) the two filaments are also chemically distinct indicating that there is both LMC and SMC gas in the Stream (Fox et al., 2013); and (2) the Stream is mostly ionized (Fox et al., 2014).

The Leading Arm is the counterpart to the Trailing Stream comprised of clumpy clouds of gas out ahead of the LMC and SMC in their orbits (seen on the left side of Figure 1.1). Due to their very high velocities, consistent with the LMC and SMC, it was proposed that these features are tidal material that has been thrown out during the interactions between the Clouds (Putman et al., 1998; Besla et al., 2012; Pardy et al., 2018). Absorption line spectroscopy studies have also investigated the chemical composition of the Leading Arm clouds but the results are not able to conclusively point to a Magellanic origin (Lu et al., 1994; Sembach et al., 2001). An alternate explanation involves the Leading Arm being gas stripped from other dwarf galaxies that fell into the Milky Way ahead of the Magellanic Clouds (Yang et al., 2014). However, dwarf galaxy candidates with positions and velocities to make this a plausible scenario have yet to be found (Tepper-García et al., 2019).

The Magellanic Bridge is a gaseous and stellar structure connecting the LMC and the SMC. This structure has historically been considered separately from the Stream because it contains stars while the Stream does not, and the Bridge and the Stream likely formed at different times (D'Onghia and Fox, 2016). The stars and the gas in the Bridge have been well studied indicating a SMC-like metallicity (Lehner et al., 2008; Misawa et al., 2009), a flow of stars from the SMC to the LMC (Schmidt et al., 2020), and intricate tidal structures such as a counter-bridge (Dias et al., 2021). Based on the existence of this Bridge and its proper motions, as well as the observed velocities of the galaxies, it is very likely that the LMC and SMC experienced a direct collision within the past several hundred million years (Zivick et al., 2018; Zivick et al., 2019; Murray et al., 2019; Schmidt et al., 2020).

1.1.1 Modeling

Early on, it was assumed that the LMC and SMC were long-lived satellites of the Milky Way, and the Stream had been formed through repeated tidal encounters between the LMC and our Galaxy (Fujimoto and Sofue, 1976; Davies and Wright, 1977; Lin and Lynden-Bell, 1977). Significant computational effort went into determining a model that could reproduce the observations. However, Fujimoto and Sofue (1977) found that no parameters for the masses and orbits of the Clouds could reproduce the high negative radial velocity of the Stream. Moreover, Bregman (1979) discussed several alternative formation mechanisms and found that none of the proposed theories at that time were sufficient to explain the Stream.

The next piece of the puzzle came in the 1990s with proper motion measurements for the Clouds (Kroupa et al., 1994; Jones et al., 1994). Using *Hubble*, Kallivayalil et al. (2006) determined that the LMC's velocity was very high (comparable with the Milky Way's escape velocity). Besla et al. (2007) and Kallivayalil et al. (2013) subsequently showed that these new data indicate that the Clouds are most likely on their first approach to the Milky Way. Therefore, previous tidal models were no longer viable. However, Besla et al. (2010) proposed a new paradigm for the tidal formation of the Stream in which the material is stripped out of the SMC through interactions with the LMC before they approach our Galaxy (Besla et al., 2012; Pardy et al., 2018). This has been widely considered the prevailing model for the formation of the Stream.

Throughout this exploration, cutting edge computer simulations have allowed researchers to run these experiments and test their models. Test particle studies in which massless particles move within constant gravitational potentials allowed for the exploration of tidal features (e.g. Fujimoto and Sofue, 1977; Murai and Fujimoto, 1980). However, the limited resolution (only using a few hundred particles) and the fact that the gravitational potentials couldn't deform limited their accuracy. Self-consistent N-body simulations which discretized the galaxies into a large number of massive particles were a significant step forward, however total particle numbers were still limited until the mid 2000s (Gardiner and Noguchi, 1996; Connors et al., 2006).

Another key development in the accuracy of the simulations was the inclusion of gas physics and hydrodynamic effects. All the models listed above simply used collisionless particles to trace the SMC's tidal tails. However, in reality these are gaseous tails which would experience ram pressure, friction, cooling, and heating. These effects had been considered in "ram-pressure" models of the Stream in which the trailing material is pushed out of the Magellanic disks through interactions with an extended gaseous halo around the Milky Way (Meurer et al., 1985; Moore and Davis, 1994; Sofue, 1994). However, these efforts were largely analytic due to the limited computational resources of the time. The development of hydrodynamics simulation codes allowed for the full, self-consistent exploration of both the tidal and ram pressure models.

With these advanced new codes and dramatic increases in computation power, modern simulations have come a long way. We can track $> 10^7$ massive particles while considering self-consistent hydrodynamics with radiative cooling, star formation, stellar feedback, and metallicity (Mastropietro et al., 2005; Besla et al., 2012; Hammer et al., 2015; Pardy et al., 2018; Tepper-García et al., 2019; Wang et al., 2019). These techniques have been used to test our models, and there are currently two leading theories for the formation of the Magellanic Stream. As mentioned above, the original tidal model has evolved into a scenario in which the LMC and SMC are orbiting around each other and the gravitational forces between the Clouds tidally strip material before they fall towards the Milky Way (Besla et al., 2012; Pardy et al., 2018). In addition, the ram pressure model proposes that the Stream material is pushed out of the disks of the Magellanic Clouds through hydrodynamical interactions with the Milky Way's hot gaseous halo. This model is also able to reproduce many of the features of the Trailing Stream (Hammer et al., 2015; Wang et al., 2019).

Just as the measurement of the proper motions of the Clouds ruled out multiple-passage models of the formation of the Stream, recent observations have been shown to be in conflict with these two existing models – (1) the Magellanic System is mostly ionized (Fox et al., 2014), and (2) the LMC has a total mass $> 10^{11}$ $M_\odot$ (e.g. Peñarrubia et al., 2016; Erkal and Belokurov, 2020; Petersen and Peñarrubia, 2021). While the tidal model requires a high LMC mass, it alone can't explain the ionized gas mass (Pardy et al., 2018); and the ram pressure model can form the ionized material, but it requires a very low mass for the LMC (Wang et al., 2019). These dilemmas are discussed below.

1.1.2 Magellanic Ionization Fraction

As mentioned above, absorption line spectroscopy has revolutionized our understanding of the Magellanic System. By characterizing its chemical composition and ionization state, we have arrived at a completely new picture of the Stream (Lu et al., 1994; Sembach et al., 2003; Fox et al., 2013; Richter et al., 2013; Fox et al., 2014). Figure 1.2 shows the neutral Stream detected in 21 cm H I in blue (from the HI4PI survey; Westmeier, 2018) overlaid with the locations of 53 sightlines used in Fox et al. (2014) to measure the total ionized gas associated with the Stream. They are colored by C IV column density and open circles represent upper limits. From these observations, they were able to estimate the total ionized gas mass at $\sim 1.5 \times 10^9$ $M_\odot$ (compared with 4.9×10^8 $M_\odot$ of neutral H I) and the average ionization fraction along the length of the Stream at 73%.

Building off of the work of Besla et al. (2012), Pardy et al. (2018) explored new, first-passage, tidal models of Stream formation attempting to account for this incredibly large amount of gas. However, even by dramatically increasing the initial gas masses of the LMC and SMC, they were unable to strip more than 10^9 $M_\odot$. For the tidal model to explain the observed ionized gas, the material can't come from the disks of the Clouds. On the other hand, ram-pressure models are able to form a large amount of ionized material in the Trailing Stream through dissolution of the neutral phase through instabilities such as the Kelvin-Helmholtz instability (Hopkins, 2015; Wang et al., 2019). However, these models require a very low LMC mass inconsistent with observations. This is discussed in the next section.

1.1.3 Total Mass of the LMC

Original estimates of the total masses of the Magellanic Clouds came from their rotation curves (van der Marel et al., 2002; Stanimirović et al., 2004; van der Marel and Kallivayalil, 2014; Di

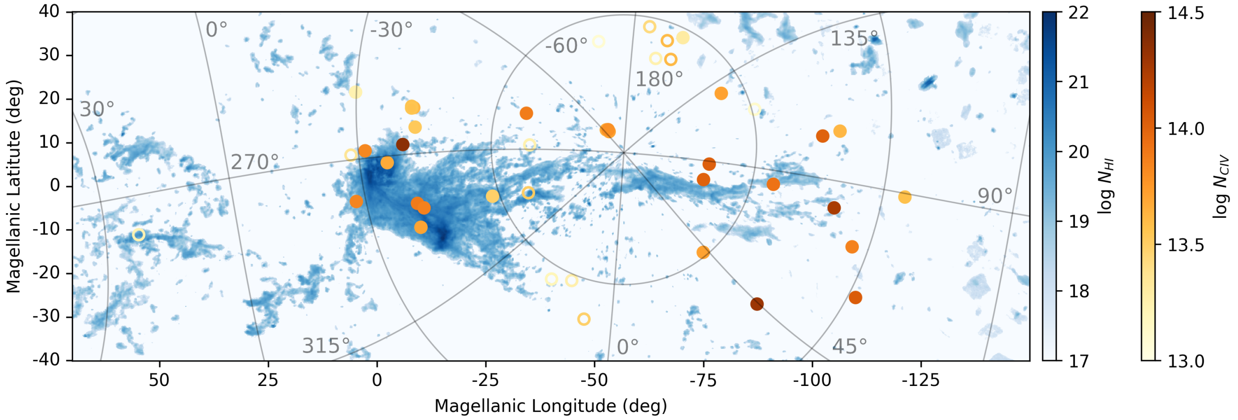

Figure 1.2: The neutral and ionized Stream in Magellanic Coordinates. The blue background shows the 21 cm neutral hydrogen emission from the HI4PI survey (Westmeier, 2018). The data is presented in Magellanic Coordinates (Nidever et al., 2008) with the Leading Arm on the left, the LMC and SMC in the center, and the Trailing Stream extending out to the right. Galactic coordinates are overlaid. The orange dots show the sightlines used in Fox et al. (2014) to detect the ionized component of the Stream. Each dot is colored by the column density of ionized carbon (C IV) with open circles representing lower limits. They estimated that 73% of the Stream is ionized with a total mass of $\sim 2 \times 10^9$ $M_\odot$ (Fox et al., 2014).

Teodoro et al., 2019). By measuring the velocities of stars or gas in the outer disks of the LMC and the SMC, scientists were able to estimate the total mass enclosed within these radii. However, these measurements could only reach out to 8.7 and 4 kpc for the LMC and the SMC, respectively, while their tidal radii and virial radii extend out tens of kpc. Thus, these must be taken as lower limits for the total masses of these galaxies. These methods give total masses of $1.7 \pm 0.7 \times 10^{10}$ $M_\odot$ for the LMC (van der Marel and Kallivayalil, 2014), and $1.25 \pm 0.25 \times 10^9$ $M_\odot$ for the SMC (Di Teodoro et al., 2019). By assuming a dark matter halo profile for the galaxies, their total virial masses can be estimated by extrapolating these observed values out to larger distances. However, it is unclear how reliable these estimates are due to the close proximity and probable past interactions between the LMC, SMC, and MW.

Recently, astronomers have also been able to infer the mass of the LMC indirectly through a variety of methods. The six methods outlined below are independent ways to determine the original mass of the LMC.

1. *Abundance Matching.* Through statistics of many observations, we can assign a total mass to a galaxy based on its stellar mass alone (Behroozi et al., 2010; Guo et al., 2010). For the LMC's stellar mass of 3.2×10^9 $M_\odot$ (van der Marel et al., 2009), we obtain a pre-infall total mass of $\sim 1.6 \times 10^{11}$ $M_\odot$ (Garavito-Camargo et al., 2019). Alternatively, Read and Erkal

(2019) found a better correspondence between star formation rate and total mass giving a value of $1.99 \pm 0.34 \times 10^{11}$ $M_\odot$.

2. *Milky Way Reflex Motion.* The fact that the Clouds are their first infall, combined with the possibility of a high LMC mass, meant that the approach of the Magellanic System could significantly distort our Galaxy. One such implication is that the inner parts of the Milky Way are no longer in alignment with the outer regions (Gómez et al., 2015; Petersen and Peñarrubia, 2020; Petersen and Peñarrubia, 2021). As the LMC approaches us, the Milky Way will be pulled towards it, leading to an offset between the inner and outer parts of the galaxy. Recently, this reflex motion has been detected in observations of the outer stellar halo, requiring that the LMC's total mass be $> 10^{11}$ $M_\odot$ (Petersen and Peñarrubia, 2021).

3. *Dark Matter Wake.* In addition to shifting the inner Galaxy with respect to the outer Galaxy, a first-infall model of the LMC's approach will induce a more complex "wake" in the dark matter distribution of the Milky Way. This effect is comprised of the traditional dynamical friction (Chandrasekhar, 1943) combined with a *collective* response visible throughout the Galaxy caused by the resonant responses of the LMC's first passage (Garavito-Camargo et al., 2019). This effect has been investigated in simulations (Garavito-Camargo et al., 2019) and detected in observations (Conroy et al., 2021), however further work is required to conclusively attribute this effect to the LMC.

4. *LMC's Satellite Population.* Based on their proper motions, Kallivayalil et al. (2013) found that the LMC would need to be $> 10^{11}$ $M_\odot$ in order for the Magellanic Clouds to remain bound to each other for at least 2 Gyr. In addition to the SMC, the LMC seems to have several other satellites that it is bringing in towards the Milky Way (D'Onghia and Lake, 2008; Bechtol et al., 2015; Nichols et al., 2011; Pardy et al., 2020; Patel et al., 2020). Erkal and Belokurov (2020) found that, in addition to the SMC, there are six dwarfs likely accreted with the LMC which would require a mass of at least 1.24×10^{11} $M_\odot$.

5. *Timing Argument.* Due to the expansion of the universe, one can back out the mass of a group of galaxies based on their relative velocities and the fact that their mutual gravitational force has kept them together throughout the age of the universe (Lynden-Bell, 1981; Sandage, 1986;

Partridge et al., 2013). If the LMC is massive, it will necessarily play a role in this evolution and must be considered (Gómez et al., 2015; Peñarrubia et al., 2016). The timing argument indicates a mass of $2.5^{+0.09}_{-0.08} \times 10^{11}$ M$_\odot$ (Peñarrubia et al., 2016). However, the inclusion of the Milky Way's reflex motion reduces the estimated mass of our Local Group by $\sim 10\%$ (Chamberlain et al., 2023).

6. *Stellar Streams.* The explosion in stellar astrometry from *Gaia* (Gaia Collaboration et al., 2016) has allowed for unprecedented exploration of the Milky Way's stellar halo. The discovery of numerous stellar streams, tidal remnants of disrupted dwarf galaxies, have given us important insight into the gravitational potential (Ibata et al., 1994; Odenkirchen et al., 2003; Belokurov et al., 2006). The deviation from their expected orbits can't be explained by the Milky Way's potential alone, so by accounting for the LMC's effects we can constrain its mass to $1 - 2 \times 10^{11}$ M$_\odot$ (Erkal et al., 2019; Shipp et al., 2021; Vasiliev et al., 2021).

Prior to Besla et al. (2010), models of the formation of the Magellanic Stream used a low mass value for the LMC: $2 - 3 \times 10^{10}$ M$_\odot$. This was because it was believed to have been tidally truncated through its repeated interactions with the Milky Way. Due to significantly increased proper motion observations in Kallivayalil et al. (2006) and Kallivayalil et al. (2013), a first-passage scenario became more likely (Besla et al., 2007). Before its approach to the MW, the LMC would not have been tidally truncated, so Besla et al. (2010) used the total primordial mass estimate of 1.8×10^{11} M$_\odot$. Subsequent first-infall tidal models have used similar values (Besla et al., 2012; Pardy et al., 2018; Lucchini et al., 2020; Lucchini et al., 2021).

Ram pressure models, on the other hand, require a low LMC mass. In order for the stripping to be efficient, the LMC's disk gas must be loosely bound. This requires a total mass $< 2 \times 10^{10}$ M$_\odot$ (Hammer et al., 2015; Wang et al., 2019). Therefore, these models are inconsistent with the recent indications of a high LMC mass.

Figure 1.3 summarizes the different LMC mass estimates from various studies. Two references give estimates within a given radius ($1.7 \pm 0.7 \times 10^{10}$ M$_\odot$ within 8.7 kpc, van der Marel and Kallivayalil, 2014; $7.02 \pm 0.9 \times 10^{10}$ M$_\odot$ within 32.8 kpc, Koposov et al., 2023), three references give lower (or upper) limits (Kallivayalil et al., 2013; Wang et al., 2019; Erkal and Belokurov, 2020; Petersen and Peñarrubia, 2021), and four give total mass estimates (Peñarrubia et al., 2016; Read

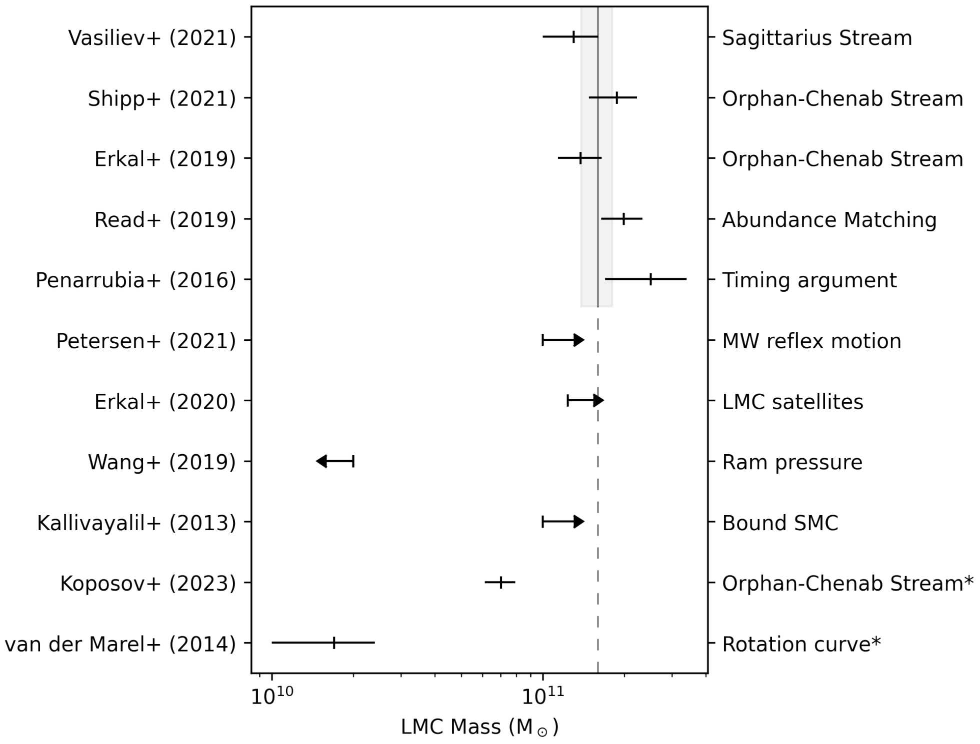

Figure 1.3: Observational LMC mass estimates. Literature estimates for the mass of the Large Magellanic Cloud. van der Marel and Kallivayalil (2014) and Koposov et al. (2023) (denoted with asterisks) provide constraints on the mass within 8.7 and 32.4 kpc, respectively, whereas all other estimates plotted are for the total virial LMC mass. Kallivayalil et al. (2013), Erkal and Belokurov (2020), and Petersen and Peñarrubia (2021) provide lower limits, and Wang et al. (2019) provides an upper limit. The remaining references (Peñarrubia et al., 2016; Read and Erkal, 2019; Erkal et al., 2019; Shipp et al., 2021; Vasiliev et al., 2021) give estimates of the total LMC mass with uncertainties. The error weighted average of these five values is $1.57 \pm 0.21 \times 10^{11}$ shown as the vertical line (extended to the bottom of the plot as a dashed line for comparison). The one-sigma errors are shown as a shaded region. The method for determining the LMC mass estimate from each paper is listed on the right edge of the plot.

and Erkal, 2019; Erkal et al., 2019; Shipp et al., 2021; Vasiliev et al., 2021). Taking the error weighted average of the five total mass measurements, we obtain a value of $1.57 \pm 0.21 \times 10^{11}$ $M_\odot$ shown by the vertical line and shaded region.

This new data requires that a new paradigm for the formation of the Stream be developed. Both tidal interactions and ram pressure forces must play a role in order to accurately reproduce all the available data. The combination of these new observations with incredible advancements in simulation technology has brought the field to a place where these new models can now be explored.

1.2 Thesis Outline

This thesis will present a complete picture of the formation of the Magellanic Stream, consistent with both the ionized gas observations and a high LMC mass. I have run numerical simulations of the interactions between the Magellanic Clouds and the Milky Way while including two additional components of these galaxies – a hot gaseous halo around the Milky Way, and the Magellanic Corona, a warm gaseous halo around the LMC. In Chapter 2, I outline the motivation for the Magellanic Corona and show that it can provide the ionized gas mass that we observe in the Magellanic System today.

In Chapter 3, I explore the implication of this Magellanic Corona on the orbital history of the Magellanic Clouds. As the SMC orbits around the LMC, it is now moving through this warm gaseous medium, experiencing hydrodynamical drag. Thus previous orbits for the Clouds are no longer consistent with their present-day positions and velocities. In this chapter, I present a new orbital model consistent with the locations and proper motions of the Clouds today that is able to reproduce the Trailing Stream while including the Magellanic Corona and a hot gas halo around the Milky Way. Specifically, these requirements result in a Stream that is a factor of 5 closer to the Sun than previous models predicted.

In Chapter 4, I discuss estimates of the properties of the Magellanic Corona and Milky Way's circumgalactic gas based on simulations of the formation of the Stream. We are able to constrain the total mass and temperature of the Magellanic Corona by requiring its long-term stability and existence around the LMC and through comparisons with observational data. The Milky Way's gaseous halo plays a strong role in determining the distribution of the ionized material on the sky and the length and morphology of the Trailing Stream. This allows us to also place constraints on its total mass and distribution.

Chapter 5 presents my work and main results for non-science audiences. With the support of the Wisconsin Initiative for Science Literacy, I developed this chapter to better share my work with friends and family and continue to improve my communication skills. I found it very enjoyable to approach the discussion of my research from a different perspective.

Chapter 6 summarizes my results and discusses next steps and continuing work.

REFERENCES

Bechtol, K., et al. 2015, *ApJ*, 807, 50, `10.1088/0004-637X/807/1/50`.

Behroozi, P. S., Conroy, C., and Wechsler, R. H. 2010, *ApJ*, 717, 379–403, `10.1088/0004-637X/717/1/379`.

Belokurov, V., et al. 2006, *ApJ Letters*, 642, L137–L140, `10.1086/504797`.

Besla, G., et al. 2010, *ApJ*, 721, L97–L101, `10.1088/2041-8205/721/2/L97`.

Besla, G., et al. 2007, *ApJ*, 668, 949–967, `10.1086/521385`.

Besla, G., et al. 2012, *MNRAS*, 421, 2109–2138, `10.1111/j.1365-2966.2012.20466.x`.

Bregman, J. N. 1979, *ApJ*, 229, 514–523, `10.1086/156984`.

Brüns, C., et al. 2005, *A&A*, 432, 45–67, `10.1051/0004-6361:20040321`.

Chamberlain, K., et al. 2023, *ApJ*, 942, 18, `10.3847/1538-4357/aca01f`.

Chandrasekhar, S. 1943, *ApJ*, 97, 255, `10.1086/144517`.

Cioni, M. .-. L., Habing, H. J., and Israel, F. P. 2000, *A&A*, 358, L9–L12, `10.48550/arXiv.astro-ph/0005057`.

Cohen, R. J. 1982, *MNRAS*, 199, 281–293, `10.1093/mnras/199.2.281`.

Connors, T. W., Kawata, D., and Gibson, B. K. 2006, *MNRAS*, 371, 108–120, `10.1111/j.1365-2966.2006.10659.x`.

Conroy, C., et al. 2021, *Nature*, 592, 534–536, `10.1038/s41586-021-03385-7`.

Crowther, P. A., et al. 2016, *MNRAS*, 458, 624–659, `10.1093/mnras/stw273`.

D'Onghia, E. and Fox, A. J. 2016, *ARA&A*, 54, 363–400, `10.1146/annurev-astro-081915-023251`.

D'Onghia, E. and Lake, G. 2008, *ApJ*, 686, L61, `10.1086/592995`.

Davies, R. D. and Wright, A. E. 1977, *MNRAS*, 180, 71–88, `10.1093/mnras/180.2.71`.

Di Teodoro, E. M., et al. 2019, *MNRAS*, 483, 392–406, `10.1093/mnras/sty3095`.

Dias, B., et al. 2021, *A&A*, 647, L9, `10.1051/0004-6361/202040015`.

Erkal, D., et al. 2019, *MNRAS*, 487, 2685–2700, `10.1093/mnras/stz1371`.

Erkal, D. and Belokurov, V. A. 2020, *MNRAS*, 495, 2554–2563, `10.1093/mnras/staa1238`.

Ferreira, L., et al. 2022, *ApJ Letters*, 938, L2, `10.3847/2041-8213/ac947c`.

For, B.-Q., et al. 2014, *ApJ*, 792, 43, `10.1088/0004-637X/792/1/43`.

Fox, A. J., et al. 2010, *ApJ*, 718, 1046–1061, `10.1088/0004-637X/718/2/1046`.

Fox, A. J., et al. 2013, *ApJ*, 772, 110, `10.1088/0004-637X/772/2/110`.

Fox, A. J., et al. 2014, *ApJ*, 787, 147, `10.1088/0004-637X/787/2/147`.

Fujimoto, M. and Sofue, Y. 1976, *A&A*, 47, 263–291.

———. 1977, *A&A*, 61, 199–215.

Gaia Collaboration, et al. 2016, *A&A*, 595, A1, `10.1051/0004-6361/201629272`.

Garavito-Camargo, N., et al. 2019, *ApJ*, 884, 51, `10.3847/1538-4357/ab32eb`.

Gardiner, L. T. and Noguchi, M. 1996, *MNRAS*, 278, 191–208, `10.1093/mnras/278.1.191`.

Gibson, B. K., et al. 2000, *AJ*, 120, 1830–1840, `10.1086/301545`.

Gómez, F. A., et al. 2015, *ApJ*, 802, 128, `10.1088/0004-637X/802/2/128`.

Graczyk, D., et al. 2020, *ApJ*, 904, 13, `10.3847/1538-4357/abbb2b`.

Guo, Q., et al. 2010, *MNRAS*, 404, 1111–1120, `10.1111/j.1365-2966.2010.16341.x`.

Hammer, F., et al. 2015, *ApJ*, 813, 110, `10.1088/0004-637X/813/2/110`.

Hopkins, P. F. 2015, *MNRAS*, 450, 53–110, `10.1093/mnras/stv195`.

Ibata, R. A., Gilmore, G., and Irwin, M. J. 1994, *Nature*, 370, 194–196, `10.1038/370194a0`.

Jones, B. F., Klemola, A. R., and Lin, D. N. C. 1994, *AJ*, 107, 1333, `10.1086/116947`.

Kalari, V. M., et al. 2022, *ApJ*, 935, 162, `10.3847/1538-4357/ac8424`.

Kallivayalil, N., et al. 2006, *ApJ*, 638, 772–785, `10.1086/498972`.

Kallivayalil, N., et al. 2013, *ApJ*, 764, 161, `10.1088/0004-637X/764/2/161`.

Koposov, S. E., et al. 2023, *MNRAS*, `10.1093/mnras/stad551`.

Kroupa, P., Röser, S., and Bastian, U. 1994, *MNRAS*, 266, 412–420, `10.1093/mnras/266.2.412`.

Lehner, N., et al. 2008, *ApJ*, 678, 219–233, `10.1086/529574`.

Lin, D. N. C. and Lynden-Bell, D. 1977, *MNRAS*, 181, 59–81, `10.1093/mnras/181.2.59`.

Lu, L., Savage, B. D., and Sembach, K. R. 1994, *ApJ Letters*, 437, L119, `10.1086/187697`.

Lucchini, S., D'Onghia, E., and Fox, A. J. 2021, *ApJ Letters*, 921, L36, `10.3847/2041-8213/ac3338`.

Lucchini, S., et al. 2020, *Nature*, 585, 203–206, `10.1038/s41586-020-2663-4`.

Lynden-Bell, D. 1981, *The Observatory*, 101, 111–114.

Mastropietro, C., et al. 2005, *MNRAS*, 363, 509–520, `10.1111/j.1365-2966.2005.09435.x`.

Mathewson, D. S., Cleary, M. N., and Murray, J. D. 1974, *ApJ*, 190, 291–296, `10.1086/152875`.

Meurer, G. R., Bicknell, G. V., and Gingold, R. A. 1985, *PASA*, 6, 195–198, `10.1017/S1323358000018075`.

Misawa, T., et al. 2009, *ApJ*, 695, 1382–1398, `10.1088/0004-637X/695/2/1382`.

Moore, B. and Davis, M. 1994, *MNRAS*, 270, 209–221, `10.1093/mnras/270.2.209`.

Morras, R. 1983, *AJ*, 88, 62–66, `10.1086/113287`.

Murai, T. and Fujimoto, M. 1980, *PASJ*, 32, 581–603.

Murray, C. E., et al. 2019, *ApJ*, 887, 267, `10.3847/1538-4357/ab510f`.

Nichols, M., et al. 2011, *ApJ*, 742, 110, `10.1088/0004-637X/742/2/110`.

Nidever, D. L., Majewski, S. R., and Butler Burton, W. 2008, *ApJ*, 679, 432–459, `10.1086/587042`.

Odenkirchen, M., et al. 2003, *AJ*, 126, 2385–2407, `10.1086/378601`.

Pardy, S. A., D'Onghia, E., and Fox, A. J. 2018, *ApJ*, 857, 101, `10.3847/1538-4357/aab95b`.

Pardy, S. A., et al. 2020, *MNRAS*, 492, 1543–1549, `10.1093/mnras/stz3192`.

Partridge, C., Lahav, O., and Hoffman, Y. 2013, *MNRAS*, 436, L45–L48, `10.1093/mnrasl/slt109`.

Patel, E., et al. 2020, *ApJ*, 893, 121, `10.3847/1538-4357/ab7b75`.

Peñarrubia, J., et al. 2016, *MNRAS*, 456, L54–L58, `10.1093/mnrasl/slv160`.

Petersen, M. S. and Peñarrubia, J. 2020, *MNRAS*, 494, L11–L16, `10.1093/mnrasl/slaa029`.

———. 2021, *Nature Astronomy*, 5, 251–255, `10.1038/s41550-020-01254-3`.

Pingel, N. M., et al. 2022, *PASA*, 39, e005, `10.1017/pasa.2021.59`.

Putman, M. E., et al. 1998, *Nature*, 394, 752–754, `10.1038/29466`.

Read, J. I. and Erkal, D. 2019, *MNRAS*, 487, 5799–5812, `10.1093/mnras/stz1320`.

Richter, P., et al. 2013, *ApJ*, 772, 111, `10.1088/0004-637X/772/2/111`.

Sandage, A. 1986, *ApJ*, 307, 1, `10.1086/164387`.

Schmidt, T., et al. 2020, *A&A*, 641, A134, `10.1051/0004-6361/202037478`.

Sembach, K. R., et al. 2003, *ApJ Supplement*, 146, 165–208, `10.1086/346231`.

Sembach, K. R., et al. 2001, *AJ*, 121, 992–1002, `10.1086/318777`.

Shipp, N., et al. 2021, *ApJ*, 923, 149, `10.3847/1538-4357/ac2e93`.

Sofue, Y. 1994, *PASJ*, 46, 431–440, `10.48550/arXiv.astro-ph/9403041`.

Stanimirović, S., Staveley-Smith, L., and Jones, P. A. 2004, *ApJ*, 604, 176–186, `10.1086/381869`.

Subramanian, S. and Subramaniam, A. 2012, *ApJ*, 744, 128, `10.1088/0004-637X/744/2/128`.

Tepper-García, T., et al. 2019, *MNRAS*, 488, 918–938, `10.1093/mnras/stz1659`.

van der Marel, R. P. and Kallivayalil, N. 2014, *ApJ*, 781, 121, `10.1088/0004-637X/781/2/121`.

van der Marel, R. P., Kallivayalil, N., and Besla, G. "The Magellanic System: Stars, Gas, and Galaxies". *The Magellanic System: Stars, Gas, and Galaxies.* Ed. by J. T. Van Loon and J. M. Oliveira, 2009, 81–92, `10.1017/S1743921308028299`.

van der Marel, R. P., et al. 2002, *AJ*, 124, 2639–2663, `10.1086/343775`.

Vasiliev, E., Belokurov, V., and Erkal, D. 2021, *MNRAS*, 501, 2279–2304, `10.1093/mnras/staa3673`.

Wang, J., et al. 2019, *MNRAS*, 486, 5907–5916, `10.1093/mnras/stz1274`.

Westmeier, T. 2018, *MNRAS*, 474, 289–299, `10.1093/mnras/stx2757`.

Williams, R. 1996 , `hubblesite.org/contents/news-releases/1996/news-1996-01.html`. Accessed 5/5/2023.

Yang, Y., et al. 2014, *MNRAS*, 442, 2419–2433, `10.1093/mnras/stu931`.

Zaritsky, D., et al. 2000, *ApJ Letters*, 534, L53–L56, `10.1086/312649`.

Zivick, P., et al. 2018, *ApJ*, 864, 55, `10.3847/1538-4357/aad4b0`.

Zivick, P., et al. 2019, *ApJ*, 874, 78, `10.3847/1538-4357/ab0554`.

CHAPTER 2

THE MAGELLANIC CORONA AND THE FORMATION OF THE MAGELLANIC STREAM

A version of this chapter has previously appeared in Nature

Lucchini, et al. Nature, 585, 2. (2020)

Abstract

The dominant gas structure in the Galactic halo is the Magellanic Stream, an extended network of neutral and ionized filaments surrounding the Large and Small Magellanic Clouds (LMC/SMC), the two most massive satellite galaxies of the Milky Way (Mathewson et al., 1974; Nidever et al., 2008). Recent observations indicate that the Clouds are on their first passage around our Galaxy (Kallivayalil et al., 2013), the Stream is made up of gas stripped from both the LMC and the SMC (Nidever et al., 2008; Fox et al., 2013; Richter et al., 2013), and the majority of this gas is ionized (Fox et al., 2014; Barger et al., 2017). While it has long been suspected that tidal forces (Besla et al., 2012; Pardy et al., 2018) and ram-pressure stripping (Hammer et al., 2015; Wang et al., 2019) contributed to the Stream's formation, a full understanding of its origins has defied modelers for decades (D'Onghia and Fox, 2016). The recently-determined high mass of the LMC (Peñarrubia et al., 2016) and the detection of highly ionized gas toward stars in the LMC (Wakker et al., 1998; Lehner et al., 2009) suggest the existence of a halo of warm ionized gas around the LMC. Here we show that by including this "Magellanic Corona" in our hydrodynamic simulations of the Magellanic Clouds falling onto the Galaxy, we can simultaneously reproduce the Stream and its Leading Arm. Our simulations explain the Stream's filamentary structure, spatial extent, radial velocity gradient, and total ionized gas mass. We predict that the Magellanic Corona will be unambiguously observable via high-ionization absorption lines in the ultraviolet spectra of background quasars lying near the LMC. This prediction is directly testable with the Cosmic Origins Spectrograph on the Hubble Space Telescope.

2.1 Introduction

Our Galaxy is accompanied by two fairly massive dwarf galaxies, the Large and Small Magellanic Clouds, and a massive gaseous tail trailing behind them, the Magellanic Stream. The Stream is an interwoven tail of filaments pulled out of the Magellanic Clouds (MCs) in their orbit around the Milky Way (MW; Mathewson et al., 1974; Brüns et al., 2005; Nidever et al., 2008). When considered together with its Leading Arm (LA) – the Stream's counterpart in front of the MCs – the Stream stretches over 200 degrees on the sky (see Figure 2.4a; Nidever et al., 2010. With a total mass of $\sim 1-2\times 10^9$ $\mathrm{M}_\odot$ (consisting of $\sim 2\times 10^8$ $\mathrm{M}_\odot$ neutral hydrogen and the remainder in ionized gas; Fox et al., 2014; Barger et al., 2017) the Magellanic Stream dominates all the other gas clouds in the Galactic halo, both in terms of gas mass and gas inflow rate. Therefore understanding the Stream is essential to a global picture of the Galaxy's circumgalactic medium (D'Onghia and Fox, 2016).

The current paradigm of Stream formation is known as the first-infall model (Besla et al., 2007; Besla et al., 2012). In this scenario, tidal forces from the LMC acting on the SMC when the Clouds are at their first pericentric passage around the MW lead to the formation of the Stream. This model is motivated by the high tangential velocities of the Clouds (Kallivayalil et al., 2013) and the strong morphological disturbances observed in the SMC (Brüns et al., 2005; Besla et al., 2012; Pardy et al., 2018). This model successfully reproduces the size and shape of the Stream, but several difficulties remain (D'Onghia and Fox, 2016): *(i)* the observed Stream is significantly more extended spatially and a factor of up to ten more massive than the simulated Stream, especially when including its ionized component, which dominates the mass budget (Fox et al., 2014); *(ii)* the fragmented structure of the Stream and Leading Arm indicates that the interaction with the MW gas corona plays a significant role and cannot be ignored; *(iii)* the Stream is bifurcated, with kinematic and chemical analyses indicating that gas from both the LMC and SMC is present (Nidever et al., 2008; Fox et al., 2013; Richter et al., 2013). This indicates that the Stream has a dual origin, whereas tidal models predict an SMC origin because of the shallower potential well of the SMC.

The discovery of several ultra-faint dwarfs around the LMC (Bechtol et al., 2015) indicates that the LMC and SMC likely entered the MW recently as part of a system of dwarf galaxies (the

Magellanic Group), with the LMC as its largest member (D'Onghia and Lake, 2008; Nichols et al., 2011). Given the LMC dark matter halo mass of $\sim 2 \times 10^{11}$ $M_\odot$ (Peñarrubia et al., 2016), the virial temperature is $\sim 5 \times 10^5$ K, so the Magellanic Group is expected to contain a warm gas corona at this temperature. Furthermore, cosmological simulations of MW-sized galaxies with LMC-like dwarf satellites (Pardy et al., 2020) predict the existence of ionized gas halos surrounding those satellites (Hafen et al., 2019). The presence of an LMC corona is also motivated by detections of absorption from highly-ionized carbon in "down-the-barrel" spectroscopic observations of hot stars in the LMC (Wakker et al., 1998; Lehner et al., 2009). Such coronae are likely kept warm via energy input from stellar feedback and outflows.

Here we show that by including this "Magellanic Corona" in hydrodynamic simulations of Stream formation, the mass budget discrepancy of the Stream can be solved. Crucially, we reproduce the ionized component for the first time. The Magellanic Corona appears to be the key missing ingredient in models of Stream formation.

2.2 Methods

This work employs the GIZMO Hydrodynamic N-body code (Hopkins, 2015). GIZMO includes hydrodynamics schemes that can follow large bulk velocities and large dynamic ranges in density, making it an appropriate tool to model the hydrodynamic evolution of gas disks in isolation and when subjected to gravitational interactions. The Lagrangian meshless finite-mass method implemented in the code allows the tracking of fluid elements while capturing in detail the Kelvin-Helmholtz instabilities and shocks when the resolution is properly increased (Hopkins, 2015). The simulations also used the adaptive gravitational softening lengths for gas particles available in GIZMO. The softening lengths are determined by the hydrodynamic smoothing lengths to ensure consistency between the gravitational and the hydrodynamic calculations. These smoothing lengths are calculated using the 32 nearest neighbors for each particle. For the dark matter (DM) component, the softening length adopted was 290 pc, and for the stellar component 100 pc was used. The simulations also implemented radiative heating and cooling (Katz et al., 1996; Hopkins et al., 2018) and star formation and feedback (Springel and Hernquist, 2003).

2.2.1 Initial set up and simulations

We created a set of N-body and hydrodynamic simulations of gaseous and stellar exponential disks embedded in a live NFW (Navarro–Frenk–White) dark matter halo of Magellanic-sized galaxies (Springel, 2005). The LMC progenitor galaxy has a total dark matter halo mass of 17.75×10^{10} $M_\odot$ (1.8×10^5 $M_\odot$ per particle), a stellar mass of 2.5×10^9 $M_\odot$ (4.2×10^3 $M_\odot$ per particle), and a disk gas mass of 2.2×10^9 $M_\odot$ (4.4×10^3 $M_\odot$ per particle). Similarly, the SMC progenitor assumes an initial total dark halo of 2.1×10^{10} $M_\odot$ (1.9×10^5 $M_\odot$ per particle), a stellar component of 3×10^8 $M_\odot$ (4.2×10^3 $M_\odot$ per particle), and a gaseous disk of 1.6×10^9 $M_\odot$ (4.4×10^3 $M_\odot$ per particle). This gives $\sim 2.6 \times 10^6$ total particles for the Magellanic Clouds combined. For the MW, a static Hernquist potential (Hernquist, 1990) has been assumed with a total mass of 10^{12} $M_\odot$ and a scale length of 29 kpc. A live MW stellar disk and bulge have also been included with masses of 4.8×10^{10} $M_\odot$ and 8×10^9 $M_\odot$ respectively following other recent simulations (D'Onghia and L. Aguerri, 2020). The disk has only been included in the full model with both coronae.

The LMC stellar disk has a scale length of 1.8 kpc while the initial gas disk is extended with a scale length of 4.8 kpc, in agreement with isolated gaseous dwarf irregular galaxies of comparable mass (de Blok and McGaugh, 1997). Similarly, the scale length of the SMC stellar disk is initially set to 1.1 kpc and the extended gaseous disk has a scale length of 3 kpc. The outer part of the LMC disk is truncated to 25 kpc. Runs performed with the LMC outer disk truncated to various radii produce comparable results. However, for the case reported in this study, the filamentary structure of the Trailing Arm from gas tidally removed from the LMC is present but more tenuous and less pronounced as compared to previous work where the LMC disk was not truncated (Pardy et al., 2018).

The Magellanic Corona is set up as a halo of warm gas surrounding the LMC, with a mass of $\sim 3 \times 10^9$ $M_\odot$ ($\sim$1.5% of the LMC total mass) and extends throughout the virial radius of the LMC ($\sim$100 kpc). Even though the LMC is a satellite galaxy, it is still massive enough (with total mass $> 10^{11}$ $M_\odot$; Erkal et al., 2018; Erkal et al., 2019) to carry a group of dwarfs that includes the SMC, Carina and Fornax (Pardy et al., 2020) and several additional ultra-faint dwarfs (Kallivayalil et al., 2018). Hence its hot corona should be at least 10^9 $M_\odot$ in mass (Hafen et al., 2019; Jethwa et al., 2016). A less massive LMC ($\sim 5 \times 10^{10}$ $M_\odot$ as inferred from the rotation curve within 8

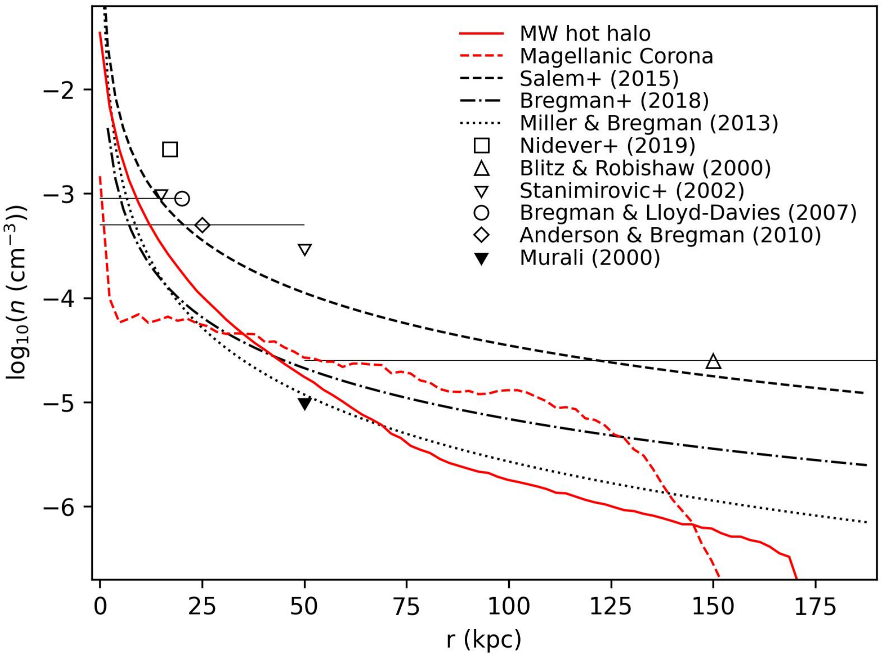

Figure 2.1: Radial gas density profile of the Magellanic Corona and MW hot corona. The number density of gas in the models of the Magellanic Corona (marked by the dashed red line) and the MW hot corona (the solid red line) are shown as a function of radius (from the center of the LMC and MW respectively). Estimates of the MW hot coronal density from observations are shown in black. The dotted and dot-dashed lines correspond to the functional form fit to data (Salem et al., 2015; Bregman et al., 2018; Miller and Bregman, 2013). The data points are labelled with their corresponding references, and are the same as those included in previous studies (Tepper-García et al., 2019). Downward (upward) pointing triangles indicate upper (lower) limits.

kpc from the center; Kallivayalil et al., 2013) would not harbor a warm corona and such an LMC would not be massive enough to carry the bright dwarfs as the observations suggest. Cosmological simulations confirm these estimates (Shen et al., 2014; Anglés-Alcázar et al., 2017; Jahn et al., 2019), and dwarf galaxies in the field have been shown to have circumgalactic gas extending out to a significant fraction of their virial radii (Bordoloi et al., 2014; Johnson et al., 2017; Sokołowska et al., 2016). Furthermore, a conservative observational estimate of the MW suggests that the circumgalactic gas is at least ∼1% of the total Galactic mass. The observed mass in baryons (stars and the interstellar medium) constitutes ∼10% of the total mass, and it is proposed that the other half of the baryons be found in the hot corona (Fukugita and Peebles, 2006). In addition, absorption line studies show that the mass of the circumgalactic gas inside the virial radius is similar to the stellar mass (Bregman et al., 2018; Lehner and Howk, 2007). Therefore, the total mass of the Magellanic Corona adopted in this work (1.5% of the LMC mass) should be considered a lower limit.

In this model, the gas properties of the Magellanic Corona surrounding the LMC are extracted from the Auriga simulations (Grand et al., 2017), a set of cosmological simulations of MW-type galaxies that contain LMC-sized satellites. The LMC analogs identified in the Auriga have proper motions similar to the *Hubble Space Telescope* (*HST*) data reported for the Clouds and do have an associated warm gas corona (Pardy et al., 2020), whose properties (temperature of $\sim 5 \times 10^5$ K, density and radial profile) are used as initial conditions for this numerical experiment. The density profile (the red dashed line reported in Figure 2.1) decreases at larger radii with a radial profile similar to recent results (Salem et al., 2015; Bregman et al., 2018; Miller and Bregman, 2013) for the MW. The LMC gas Corona is made up of particles with masses of 4.4×10^3 $M_\odot$. Velocities are assigned to gas particles according to a Maxwell-Boltzmann distribution (as in the isothermal sphere) with $f(v) \propto e^{-\frac{mv^2}{kT}}$ where m is the mean mass per particle, k is Boltzmann's constant, and for T half the virial temperature was assumed.

We note that at $T \sim 5 \times 10^5$ K, the Magellanic Corona is above the peak range of the cooling curve. Although the gaseous coronae in our models are relatively stable due to the inclusion of radiative heating and cooling, star formation and feedback, there may be additional physical processes included in cosmological simulations (Hafen et al., 2019; Grand et al., 2017), such as AGN feedback, photoionization heating, and cosmic ray heating, that affect the stability and temperature of the circumgalactic gas (Bustard et al., 2018; Bustard et al., 2020; Gronke and Oh, 2020).

In addition, a gas corona was set up around the Milky Way assuming an isothermal sphere of gas at $T = 1.6 \times 10^6$ K (the Galactic virial temperature) using the DICE code (Perret et al., 2014). The MW gas corona does not rotate in this model and we find that the infall of the Magellanic System does not affect the large-scale rotation of the coronal gas. As shown in previous work (Tepper-García et al., 2019), the rotation of the MW hot corona can have effects on the morphology and structure of the Stream, however for this study we are investigating the macroscopic properties of the Stream which should not be affected by the MW corona's rotation. The hot corona has a total mass of $\sim 2 \times 10^9$ $M_\odot$ made up of particles with masses of 4.5×10^3 $M_\odot$. It was allowed to equilibrate in isolation (with the static MW DM potential) for ~ 1 Gyr before the MCs fell in. The gas density profile assumed for the final run follows the distribution reported in previous studies (Salem et al., 2015; Bregman et al., 2018; Faerman et al., 2020) and is displayed in Figure 2.1

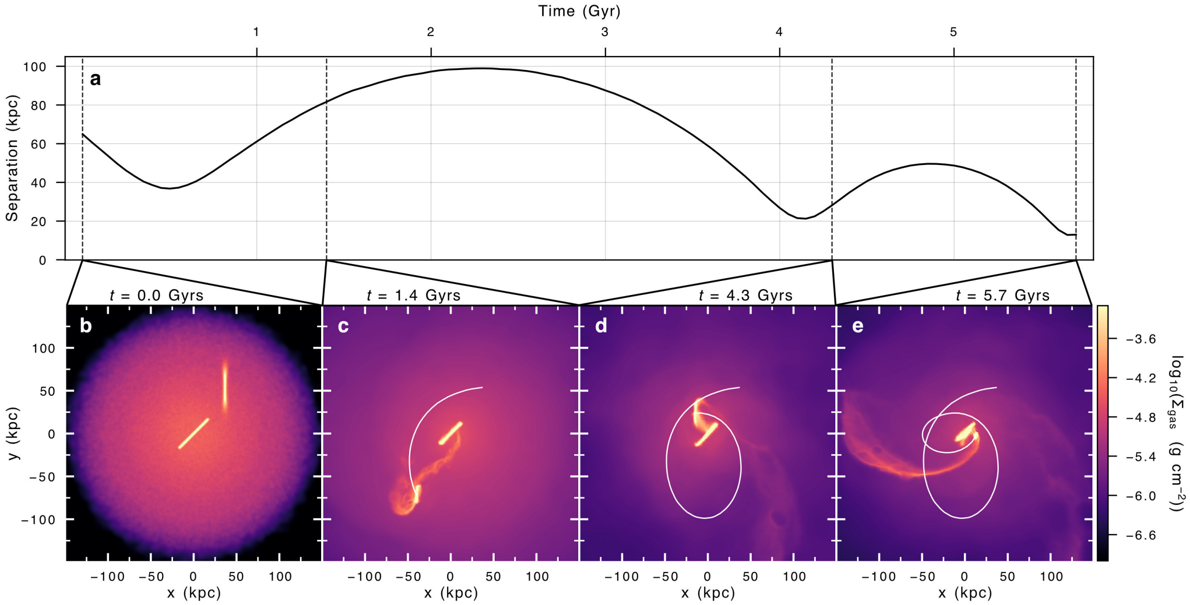

Figure 2.2: Orbital histories of the Large and Small Magellanic Clouds. **a**, Time evolution of the distance between the center of mass of the LMC and the center of mass of the SMC. The clouds interact gravitationally for a period of 5.7 Gyrs (three close encounters) before falling into the MW potential. **b-e**, Gas column density at various times during the Clouds' mutual interactions (at the initial time, after 1.4, 4.3, and 5.7 Gyrs; marked on the top plot with dotted vertical lines). Displayed is the gas tidally removed from the LMC and SMC in addition to the Magellanic Coronal gas.

(solid red line). The Magellanic Corona and MW hot gas corona constitute an additional 2×10^6 particles in the simulation.

2.2.2 Magellanic Cloud Orbital Parameters

A parameter study of the orbital configurations of the Clouds was carried out. Consistent with the findings of previous works (Diaz and Bekki, 2012; Besla et al., 2010; Besla et al., 2012; Pardy et al., 2018; D'Onghia et al., 2009; D'Onghia et al., 2010), the orbits for the LMC and SMC were set such that the Clouds experience three mutual gravitational encounters before falling into the MW potential. Note that the orbital configuration parameters were set to reproduce the bifurcation of the Stream and the H I component which is only 10-20% of its total mass. In the model shown here the Magellanic Corona is the dominant source of the total Stream mass. This result is independent on the number of encounters between the Clouds and their structural parameters. The LMC orbit is obtained first by solving the differential equation of motion assuming a mass of 2×10^{11} $M_\odot$ for the LMC before the infall and a MW mass of $\sim 10^{12}$ $M_\odot$. By imposing the current observed

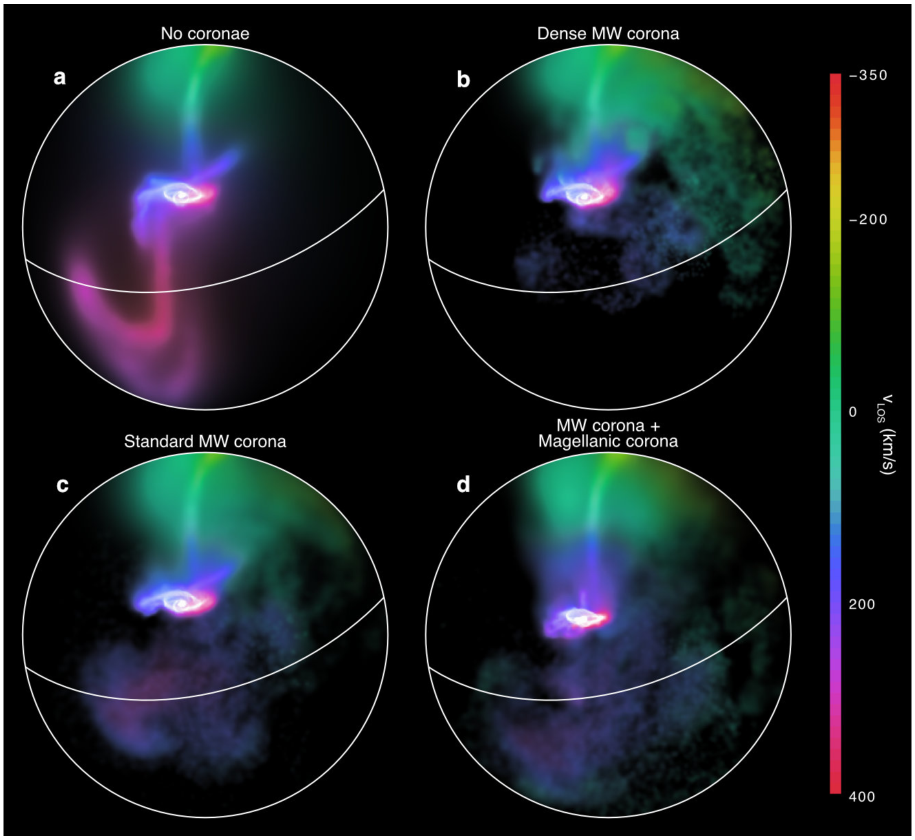

Figure 2.3: The effect of the warm and hot gas on the formation of the Leading Arm. Column density (brightness) and line-of-sight velocity (color) for four different models for the formation of the Magellanic Stream. These four models are the same as those in Figure 2.6 of the main article. In all four plots only the gas originating in the gaseous disks of the Magellanic Clouds is displayed. **a**, Fiducial model, without the MW corona or Magellanic Corona (tidal forces only). **b**, A MW coronal mass of 5×10^9 $M_\odot$ is included but the Magellanic Corona is not present. The Leading Arm does not survive, in agreement with previous studies (Tepper-García et al., 2019). **c**, Same as **b** except with the total mass of the MW hot corona lowered to 2×10^9 $M_\odot$ (see Figure 2.1), allowing the Leading Arm to survive. **d**, Same as **c** except with the addition of the Magellanic Corona. This model provides the best match to observations.

velocities and positions for the LMC as inferred by *HST* data, differential equations of motion are used to determine the position and velocities of the LMC at earlier times. Following previous studies (Pardy et al., 2018) the SMC is initially placed 65 kpc away from the LMC on a Keplerian orbit with eccentricity $e = 0.65$, and minimum separation of 25 kpc from the LMC. The orbital history of the Clouds and their mutual interactions away from the Milky Way are illustrated in Figure 2.2.

After the Clouds have had three close encounters, over a time period of 5.7 Gyrs, the LMC and SMC are placed 220 kpc away from the center of the MW on a first pericentric passage around the Galaxy. The LMC-SMC system is rotated by 180° around the z-axis, then 100° around the y-axis, then -50° around the x-axis. Then the LMC's center of mass is placed at $(x, y, z) = (-22, 217, 32)$ kpc (where the MW hot corona and DM potential are centered at the origin) with a velocity of $(v_x, v_y, v_z) = (18.6, -88.6, -109)$ km/s. The SMC's position and velocity were unchanged relative to the LMC for the first 5.7 Gyrs in isolation. Once the Clouds fall into the MW, they reach their present day positions after 1.3 Gyrs with velocities consistent with current observations (Kallivayalil et al., 2006; Kallivayalil et al., 2013). The Stream at present day is displayed in ZEA coordinates in Figure 2.3. A fiducial model where the Stream is formed by the mutual interaction between the Clouds without the inclusion of the warm and hot corona was run first (Figure 2.3a; Pardy et al., 2018). Subsequently, the same model assumed for the Clouds is carried out with the inclusion of a high-density (Figure 2.3b) or low-density MW hot gas corona (Figure 2.3c,d). This experiment allowed us to determine that the Leading Arm survives in this model if the MW gas corona has a density of $n \sim 1.7 \times 10^{-5}$ cm^{-3} at a distance of 50 kpc, in agreement with the observational estimates (Salem et al., 2015) and previous studies (Tepper-García et al., 2019). The final run included the model of the Clouds with the inclusion of both the Magellanic Corona and the MW hot halo (Figure 2.3d).

2.2.3 Analysis

A particle tracer that allows us to follow each gas particle with its temperature and density was employed to compute the mass of the Magellanic Stream. In these numerical experiments the Stream consists of gas particles stripped from the Clouds that are no longer bound to the main body of their host galaxy. The gravitational potential and its kinetic energy were calculated for each gas particle. Any particle that has a larger kinetic than potential energy was considered unbound. We then projected the locations of gas particles stripped from the Clouds into Magellanic Coordinates and summed up the masses. Based on the locations of the gas particles, they were included either in the Leading or the Trailing Stream. The pygad (Röttgers, 2018) library was adopted to perform density and temperature calculations and to deposit the particles onto a mesh for visualization. The model does not include the ionization corrections to convert the hydrogen gas into the ionized fraction. The cold gas stripped from the Clouds is assumed to trace the HI component, whereas the warm coronal gas is assumed to trace the ionized mass.

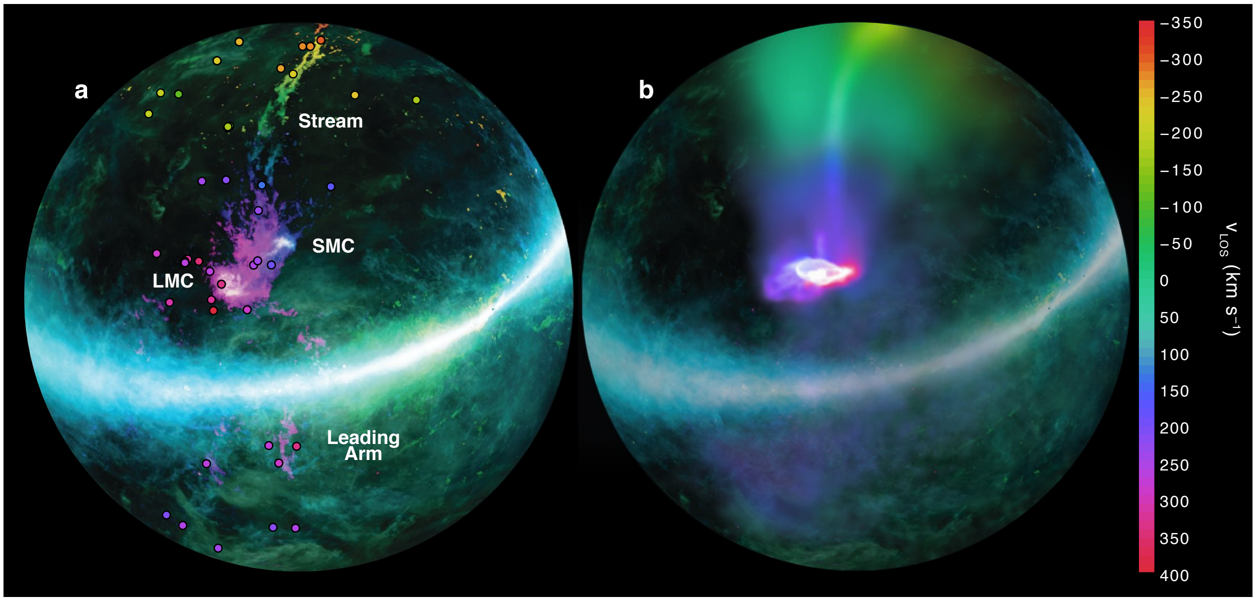

Figure 2.4: The Magellanic Stream in zenithal equal-area coordinates. **a**, Observed H I data (McClure-Griffiths et al., 2009) of the Magellanic Stream with line-of-sight velocity displayed by the color bar (from $-350\ \mathrm{km\,s^{-1}}$ to $400\ \mathrm{km\,s^{-1}}$) and brightness indicating the relative gas column density. The points represent the sightlines with UV-absorption-line observations from the *Hubble Space Telescope* (Fox et al., 2014) colored by their line-of-sight velocity. These points show the extent of the ionized gas associated with the Stream. **b**, The results of the model including the Magellanic Corona and the MW hot corona. Gas originating in both the LMC and SMC disks is shown in the model without separating the neutral gas from ionized gas. This affects the morphology of the Stream, causing the model to appear smoother and less fragmented than the data. However, the model reproduces the current spatial location and velocity of both Clouds, and the velocity gradient of the gas along the Stream. The Milky Way disk and background are extracted from real H I images (McClure-Griffiths et al., 2009).

2.3 Results

During the initial stages of the LMC-SMC tidal interaction, the pair lie outside the MW's gravitational influence. The cold gas in the extended disk of the SMC is tidally stripped through repeated encounters with the LMC (as illustrated in Figs. 2.2 and 2.7b) that occur over a period of 5.7 Gyrs. Because the model includes more massive and more extended disks for the Clouds than previous studies (Besla et al., 2012), these repeated orbits of the SMC around the LMC also result in gas extraction from the LMC (Pardy et al., 2018) by dwarf-dwarf galaxy interaction. However, this process acting on both Clouds only contributes 10–20% of the total Stream mass.

During the early period before the LMC-SMC pair fell into the MW, a Magellanic Corona of gas with $T \sim 5 \times 10^5$ K and $M \sim 3 \times 10^9\ \mathrm{M_\odot}$ surrounded the Magellanic System and extended out to the LMC's virial radius of 100 kpc. The Corona removes cold gas from the outer disk of the

SMC and heats it up by compression, as illustrated in Figure 2.7d. Later the Corona provides an additional source of ionized gas that contributes to the total mass in the Stream. The Corona is therefore a source of pressure, heating, and mass.

Once the Clouds fell into the MW and the MW hot corona, the Stream was amplified by the MW potential until it extended over 200 degrees in the sky, with both leading and trailing components. Figure 2.4 shows the Stream displayed at the present time in zenithal equal area (ZEA) projection in the numerical experiment (Figure 2.4b) as compared to the observed Stream (Figure 2.4a; McClure-Griffiths et al., 2009; Nidever et al., 2010). The MW hot corona included in this model has a total mass of $\sim 2 \times 10^9$ $M_\odot$ and does not rotate (see Methods). The presence of the hot MW gas and the Magellanic Corona have a large effect on the kinematics of the Stream. To illustrate this, Figure 2.4b displays a comparison of line-of-sight velocities of the Stream with the H I velocity gradient observed (Nidever et al., 2010) in the case when both the Magellanic and MW Coronae are included. The model shows a kinematic gradient from negative to positive velocities along the Stream ($v_{\rm LOS}$ from -350 to 400 $\rm km\,s^{-1}$), in good agreement with the observed data (Figure 2.4a). Whereas previous models found the gas to be moving $\sim$100 $\rm km\,s^{-1}$ faster than observations in the LA (Pardy et al., 2018) and slower in the Stream (Besla et al., 2012), the inclusion of coronal gas decelerates the LA to better match the observed velocity gradient. However the cold gas column density in this region is smoother than in observations, which indicate the LA is clumpy and fragmented (Brüns et al., 2005; Nidever et al., 2010; see Figure 2.5b).

In our model, both the LMC and the SMC contribute to the formation of the Stream. Most of the gas is pulled from the SMC, but there is also a tenuous filamentary contribution from the LMC, produced by tidal interactions with the MW and ram-pressure stripping in the MW hot corona. When the Magellanic System first falls into the MW, the Magellanic Corona is extended. Under the influence of the MW gravitational potential, $\sim$22% of the Magellanic Corona's initial mass becomes unbound from the LMC and incorporated into the Stream. Thus by mixing with the underlying MW hot gas, the Magellanic Corona contributes to the large ionized mass of the Stream. Figure 2.6 shows that the Magellanic Corona contributes $\sim$50% of the mass in the Leading Arm and more than 50% of the total ionized mass in the Stream. The other $\sim$50% of the mass (in both the Leading Arm and the Stream) is composed of gas extracted earlier from the SMC by its mutual interaction with the LMC with some gas heated by the Magellanic Corona before infall.

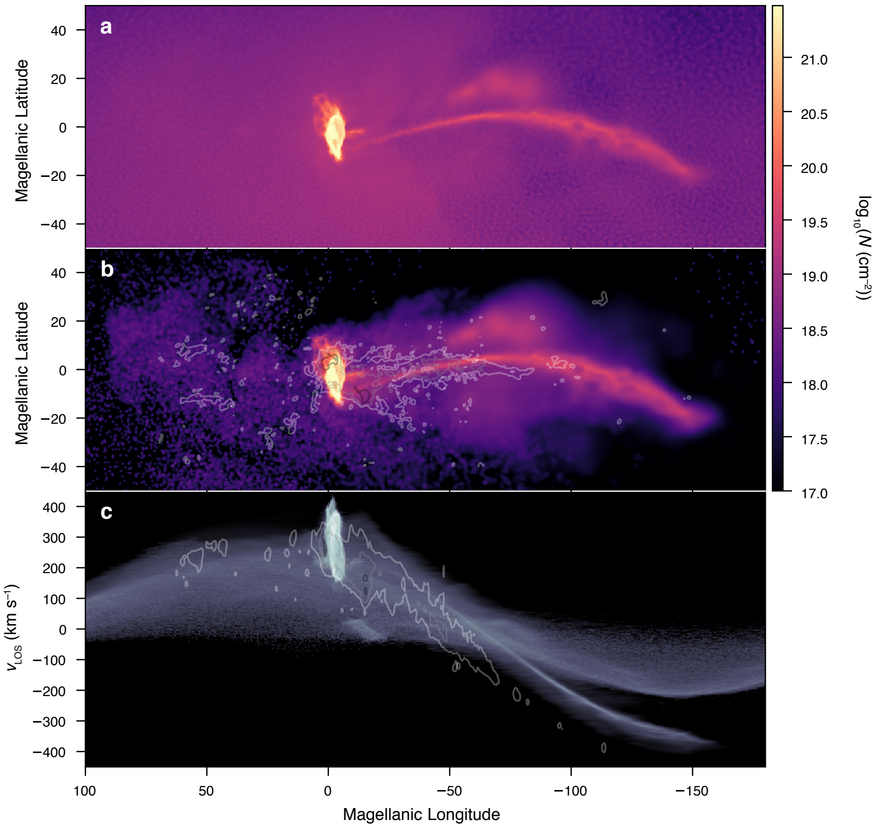

Figure 2.5: Gas column density and velocity in Magellanic Coordinates. **a**, The gas column density of the simulated Stream composed of the Magellanic Corona gas and cold disk gas stripped from the Clouds displayed in Magellanic coordinates. **b**, Column density only of the simulated cold gas Stream as compared to H I data (Nidever et al., 2010), with black, gray, white contours corresponding to the observed density of 10^{19}, 10^{20}, and 10^{21} cm^{-2} respectively. **c**, The line of sight velocity of the total Stream gas as a function of Magellanic longitude, with contours labeled as in **b** and lightness showing relative density.

This additional source of ionized gas has not been accounted for in previous theoretical work and reconciles the Stream's mass budget.

Another outcome of the model concerns the survivability of the Stream and its Leading Arm in the presence of a MW hot corona. H I studies (Putman et al., 1998; Brüns et al., 2005) show that the Leading Arm is fragmented, as expected by simulations of its passage through the Galactic halo (Heitsch and Putman, 2009), but yet it still survives. However, recent hydrodynamic simulations have challenged the overall survivability of the Leading Arm when the MW hot corona is included (Tepper-García et al., 2019). The numerical experiment reported here shows that the LA survives if the hot MW halo has a density $n \sim 1.7 \times 10^{-5}$ cm^{-3} at a distance of 50 kpc from Galactic center (see Figure 2.1). While the MW corona regulates the formation and morphology of the LA,

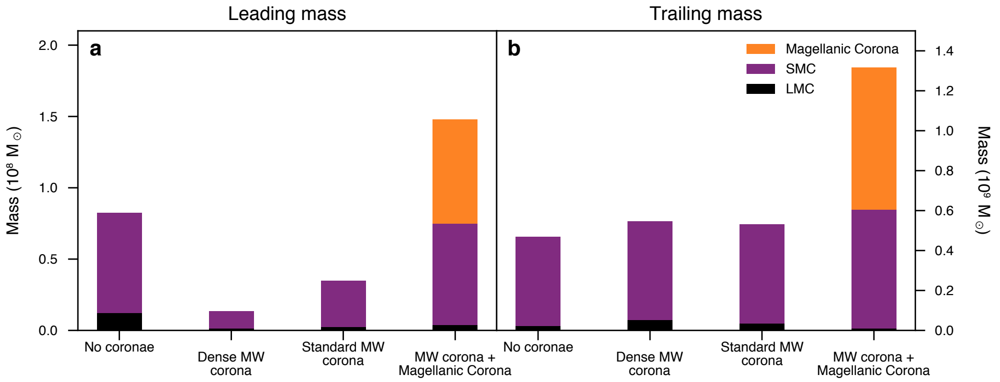

Figure 2.6: Stream mass budget. **a**, **b** Origin of the mass in the Leading Arm (**a**) and the Stream (**b**) at present day. Each column represents a model of the formation of the Stream: the fiducial dwarf-dwarf galaxy interaction model (first on the left); Besla et al., 2012; Pardy et al., 2018); a dwarf-dwarf galaxy interaction model with the inclusion of a high-density MW gas halo with total mass 5×10^9 M$_\odot$ that shows that the Leading Arm does not survive (second left column; see recent work (Tepper-García et al., 2019)); a dwarf-dwarf galaxy interaction model with the inclusion of a lower-density MW gas halo (total mass $\sim 2 \times 10^9$ M$_\odot$) still consistent with current estimates (Bregman et al., 2018; second to the right; see Figure 2.1); the model reported here of a dwarf-dwarf galaxy interaction including the lower-density MW gas halo in addition to the Magellanic Corona (right column). The inclusion of the Magellanic Corona shows that this gas contributes greatly to the total mass of the Stream: increasing it to values consistent with observations $\sim 1.3 \times 10^9$ M$_\odot$.

the inclusion of the Magellanic Corona affects its spatial extent (see Figure 2.3). The warm gas surrounding the Clouds provides a shield around the stripped gas to allow the LA gas to penetrate further into the MW hot corona. Even if the LA turns out to have a non-Magellanic origin, as recently suggested (Tepper-García et al., 2019), the inclusion of the Magellanic Corona still provides the bulk of the mass of the Trailing Stream, including its ionized component.

The inclusion of the Magellanic Corona is further supported by a recent estimate of the ambient gas density near the LA (Nidever et al., 2019). Following the discovery of stars formed in-situ in the LA (Price-Whelan et al., 2019), a recent study (Nidever et al., 2019) reports that the density of coronal gas required to separate these young stars from their proposed gaseous nursery (the region known as LA II) is an order of magnitude higher than existing measurements of the MW coronal density (Bregman et al., 2018). This discrepancy can be resolved by taking the Magellanic Corona into account, because the Magellanic Corona can add to the MW corona to yield the high total density needed to ram-pressure-strip the LA II region away from the nascent stars.

An additional consequence of this model is a possible explanation for the lack of a stellar component of the Stream. In tidal models, stars (in addition to gas) should be stripped from both Clouds due to the gravitational interactions they experience before falling in to the MW. Such

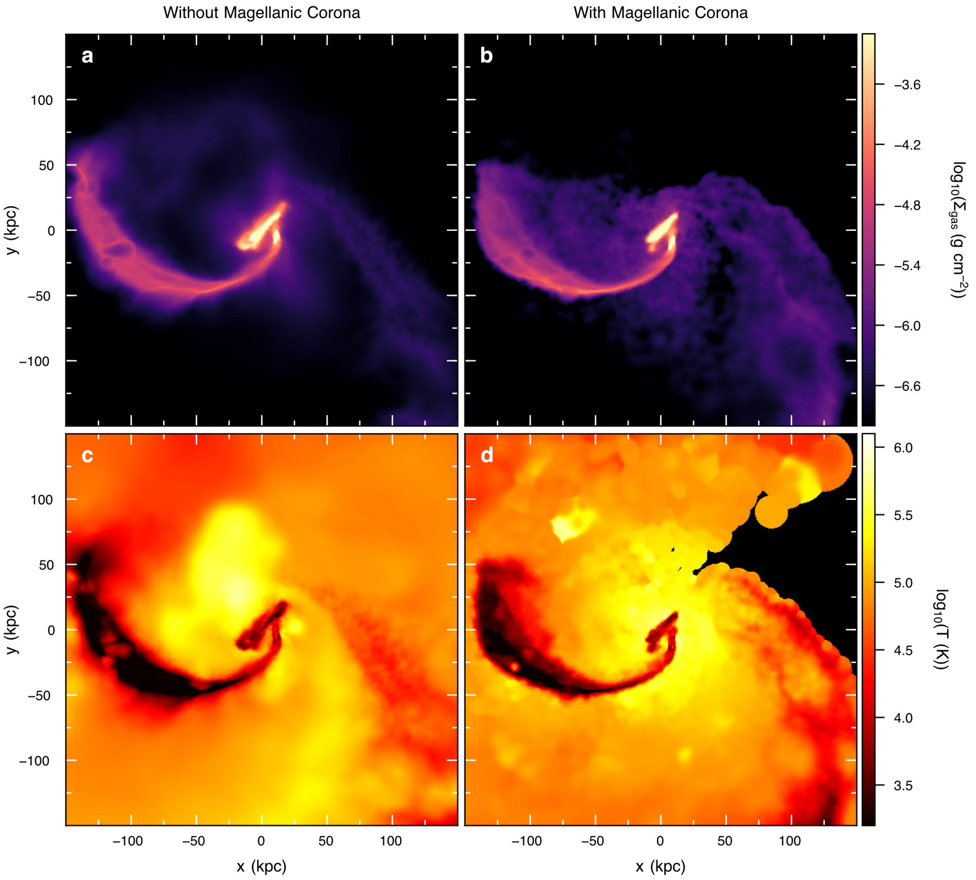

Figure 2.7: The effect of the Magellanic Corona on stripped gas temperature. The gas removed from the Magellanic Clouds after $\sim$ 5.7 Gyrs of mutual interactions (before infall into the MW potential) is shown in Cartesian coordinates projected along the z-axis onto the x-y plane. The LMC and SMC are at the center of each panel. **a, b**, The gas mass surface density of the gas originating the the disks of the Clouds. **c, d**, The gas temperature averaged along the projection axis. Shown both for models run with (**b, d**) and without (**a, c**) the Magellanic Corona included.

a stellar stream awaits discovery, even though sensitive searches have been conducted. However in our model, the Stream is mostly formed by the warm Magellanic Corona, therefore its stellar counterpart is negligible. Some stars were tidally stripped from the SMC when the Clouds were far from the MW, but they are either phase-mixed with the MW stellar halo or extended into a thin and low-density filament of 30 mag arcsec^{-2}, which is too faint to detect with current telescopes and instrumentation.

The Magellanic Corona will be unambiguously observable via absorption in highly-ionized states of carbon and silicon (C IV and Si IV) in the ultraviolet spectra of background quasars lying near the LMC on the sky. The high-ion column densities in the Corona should decrease with increasing angular separation (impact parameter) from the LMC. In contrast to the “down-the-barrel” studies of stars in the LMC (Wakker et al., 1998; Lehner et al., 2009) which pass through the interstellar medium of the LMC and may probe outflows close to the LMC disk, background-quasar sightlines offer the chance for unambiguous detections of the Corona, because they are uncontaminated by the LMC’s interstellar material.

REFERENCES

Anglés-Alcázar, D., et al. 2017, *MNRAS*, 470, 4698–4719, `10.1093/mnras/stx1517`.

Barger, K. A., et al. 2017, *ApJ*, 851, 110, `10.3847/1538-4357/aa992a`.

Bechtol, K., et al. 2015, *ApJ*, 807, 50, `10.1088/0004-637X/807/1/50`.

Besla, G., et al. 2010, *ApJ*, 721, L97–L101, `10.1088/2041-8205/721/2/L97`.

Besla, G., et al. 2007, *ApJ*, 668, 949–967, `10.1086/521385`.

Besla, G., et al. 2012, *MNRAS*, 421, 2109–2138, `10.1111/j.1365-2966.2012.20466.x`.

Bordoloi, R., et al. 2014, *ApJ*, 796, 136, `10.1088/0004-637X/796/2/136`.

Bregman, J. N., et al. 2018, *ApJ*, 862, 3, `10.3847/1538-4357/aacafe`.

Brüns, C., et al. 2005, *A&A*, 432, 45–67, `10.1051/0004-6361:20040321`.

Bustard, C., et al. 2018, *ApJ*, 863, 49, `10.3847/1538-4357/aad08f`.

Bustard, C., et al. 2020, *ApJ*, 893, 29, `10.3847/1538-4357/ab7fa3`.

D'Onghia, E. and Fox, A. J. 2016, *ARA&A*, 54, 363–400, `10.1146/annurev-astro-081915-023251`.

D'Onghia, E. and L. Aguerri, J. A. 2020, *ApJ*, 890, 117, `10.3847/1538-4357/ab6bd6`.

D'Onghia, E. and Lake, G. 2008, *ApJ*, 686, L61, `10.1086/592995`.

D'Onghia, E., et al. 2009, *Nature*, 460, 605–607, `10.1038/nature08215`.

D'Onghia, E., et al. 2010, *ApJ*, 725, 353–368, `10.1088/0004-637X/725/1/353`.

de Blok, W. J. G. and McGaugh, S. S. 1997, *MNRAS*, 290, 533–552, `10.1093/mnras/290.3.533`.

Diaz, J. D. and Bekki, K. 2012, *ApJ*, 750, 36, `10.1088/0004-637X/750/1/36`.

Erkal, D., et al. 2018, *MNRAS*, 481, 3148–3159, `10.1093/mnras/sty2518`.

Erkal, D., et al. 2019, *MNRAS*, 487, 2685–2700, `10.1093/mnras/stz1371`.

Faerman, Y., Sternberg, A., and McKee, C. F. 2020, *ApJ*, 893, 82, `10.3847/1538-4357/ab7ffc`.

Fox, A. J., et al. 2013, *ApJ*, 772, 110, `10.1088/0004-637X/772/2/110`.

Fox, A. J., et al. 2014, *ApJ*, 787, 147, `10.1088/0004-637X/787/2/147`.

Fukugita, M. and Peebles, P. J. E. 2006, *ApJ*, 639, 590–599, `10.1086/499556`.

Grand, R. J. J., et al. 2017, *MNRAS*, 467, 179–207, `10.1093/mnras/stx071`.

Gronke, M. and Oh, S. P. 2020, *MNRAS*, 492, 1970–1990, `10.1093/mnras/stz3332`.

Hafen, Z., et al. 2019, *MNRAS*, 488, 1248–1272, `10.1093/mnras/stz1773`.

Hammer, F., et al. 2015, *ApJ*, 813, 110, `10.1088/0004-637X/813/2/110`.

Heitsch, F. and Putman, M. E. 2009, *ApJ*, 698, 1485–1496, `10.1088/0004-637X/698/2/1485`.

Hernquist, L. 1990, *ApJ*, 356, 359, `10.1086/168845`.

Hopkins, P. F. 2015, *MNRAS*, 450, 53–110, `10.1093/mnras/stv195`.

Hopkins, P. F., et al. 2018, *MNRAS*, 480, 800–863, `10.1093/mnras/sty1690`.

Jahn, E. D., et al. 2019, *MNRAS*, 489, 5348–5364, `10.1093/mnras/stz2457`.

Jethwa, P., Erkal, D., and Belokurov, V. 2016, *MNRAS*, 461, 2212–2233, `10.1093/mnras/stw1343`.

Johnson, S. D., et al. 2017, *ApJ*, 850, L10, `10.3847/2041-8213/aa9370`.

Kallivayalil, N., et al. 2006, *ApJ*, 638, 772–785, `10.1086/498972`.

Kallivayalil, N., et al. 2013, *ApJ*, 764, 161, `10.1088/0004-637X/764/2/161`.

Kallivayalil, N., et al. 2018, *ApJ*, 867, 19, `10.3847/1538-4357/aadfee`.

Katz, N., Weinberg, D. H., and Hernquist, L. 1996, *ApJ Supplement*, 105, 19, `10.1086/192305`.

Lehner, N. and Howk, J. C. 2007, *MNRAS*, 377, 687–704, `10.1111/j.1365-2966.2007.11631.x`.

Lehner, N., Staveley-Smith, L., and Howk, J. C. 2009, *ApJ*, 702, 940–954, `10.1088/0004-637X/702/2/940`.

Mathewson, D. S., Cleary, M. N., and Murray, J. D. 1974, *ApJ*, 190, 291–296, `10.1086/152875`.

McClure-Griffiths, N. M., et al. 2009, *ApJ Supplement*, 181, 398–412, `10.1088/0067-0049/181/2/398`.

Miller, M. J. and Bregman, J. N. 2013, *ApJ*, 770, 118, `10.1088/0004-637X/770/2/118`.

Nichols, M., et al. 2011, *ApJ*, 742, 110, `10.1088/0004-637X/742/2/110`.

Nidever, D. L., Majewski, S. R., and Butler Burton, W. 2008, *ApJ*, 679, 432–459, `10.1086/587042`.

Nidever, D. L., et al. 2010, *ApJ*, 723, 1618–1631, `10.1088/0004-637X/723/2/1618`.

Nidever, D. L., et al. 2019, *ApJ*, 887, 115, `10.3847/1538-4357/ab52fc`.

Pardy, S. A., D'Onghia, E., and Fox, A. J. 2018, *ApJ*, 857, 101, `10.3847/1538-4357/aab95b`.

Pardy, S. A., et al. 2020, *MNRAS*, 492, 1543–1549, `10.1093/mnras/stz3192`.

Peñarrubia, J., et al. 2016, *MNRAS*, 456, L54–L58, `10.1093/mnrasl/slv160`.

Perret, V., et al. 2014, *A&A*, 562, A1, `10.1051/0004-6361/201322395`.

Price-Whelan, A. M., et al. 2019, *ApJ*, 887, 19, `10.3847/1538-4357/ab4bdd`.

Putman, M. E., et al. 1998, *Nature*, 394, 752–754, `10.1038/29466`.

Richter, P., et al. 2013, *ApJ*, 772, 111, `10.1088/0004-637X/772/2/111`.

Röttgers, B. 2018, *Astrophysics Source Code Library*, ascl:1811.014.

Salem, M., et al. 2015, *ApJ*, 815, 77, `10.1088/0004-637X/815/1/77`.

Shen, S., et al. 2014, *ApJ*, 792, 99, `10.1088/0004-637X/792/2/99`.

Sokołowska, A., et al. 2016, *ApJ*, 819, 21, `10.3847/0004-637X/819/1/21`.

Springel, V. 2005, *MNRAS*, 364, 1105–1134, `10.1111/j.1365-2966.2005.09655.x`.

Springel, V. and Hernquist, L. 2003, *MNRAS*, 339, 289–311, `10.1046/j.1365-8711.2003.06206.x`.

Tepper-García, T., et al. 2019, *MNRAS*, 488, 918–938, `10.1093/mnras/stz1659`.

Wakker, B., et al. 1998, *ApJ Letters*, 499, L87–L91, `10.1086/311334`.

Wang, J., et al. 2019, *MNRAS*, 486, 5907–5916, `10.1093/mnras/stz1274`.

CHAPTER 3

THE MAGELLANIC STREAM AT 20 KPC: A NEW ORBITAL HISTORY FOR THE MAGELLANIC CLOUDS

A version of this chapter has previously appeared as a Letter in the Astrophysical Journal

Lucchini, S., D'Onghia, E., & Fox, A. J. ApJL, 921, L36. (2021)

Abstract

We present new simulations of the formation of the Magellanic Stream based on an updated first-passage interaction history for the Magellanic Clouds, including both the Galactic and Magellanic Coronae and a live dark matter halo for the Milky Way. This new interaction history is needed because previously successful orbits need updating to account for the Magellanic Corona and the loosely bound nature of the Magellanic Group. These orbits involve two tidal interactions over the last 3.5 Gyr and reproduce the Stream's position and appearance on the sky, mass distribution, and velocity profile. Most importantly, our simulated Stream is only $\sim$20 kpc away from the Sun at its closest point, whereas previous first-infall models predicted a distance of $100-200$ kpc. This dramatic paradigm shift in the Stream's 3D position would have several important implications. First, estimates of the observed neutral and ionized masses would be reduced by a factor of $\sim$5. Second, the stellar component of the Stream is also predicted to be $<$20 kpc away. Third, the enhanced interactions with the MW's hot corona at this small distance would substantially shorten the Stream's lifetime. Finally, the MW's UV radiation field would be much stronger, potentially explaining the H α emission observed along most of the Stream. Our prediction of a 20 kpc Stream could be tested by searching for UV absorption lines toward distant MW halo stars projected onto the Stream.

3.1 Introduction

The Magellanic System is essential to our understanding of the ongoing formation and evolution of the Local Group. It consists of the two closest massive dwarf galaxies to the Milky Way (MW), the Large and Small Magellanic Clouds (LMC and SMC), and the Magellanic Stream, a massive network of gaseous filaments trailing behind the Clouds (see D'Onghia and Fox 2016 for a review). Significant theoretical and computational effort has gone into furthering our understanding of the origin and formation of the Magellanic Stream, beginning with simple analytical models (e.g. Fujimoto and Sofue, 1977), eventually including simple hydrodynamics and self-gravity e.g. Moore and Davis, 1994; Gardiner and Noguchi, 1996. Modern high-resolution simulations include live N-body models for both the LMC and the SMC as well as self-consistent hydrodynamics with radiative cooling and star formation (Besla et al. 2012, hereafter B12; Hammer et al. 2015; Pardy et al. 2018, hereafter P18; Wang et al. 2019). Most recently, Lucchini et al. (2020, hereafter L20) showed that including a Magellanic Corona of warm gas surrounding the LMC and SMC can explain the ionized gas component of the Magellanic Stream (Fox et al., 2014).

However, as these models have improved, one piece of the puzzle has remained unconstrained: the exact past orbits of the LMC and SMC. Proper motion (PM) measurements for the Magellanic Clouds have become very precise (Kallivayalil et al., 2013; Zivick et al., 2018), but the total mass of the MW and the LMC are still imprecisely known (Bland-Hawthorn and Gerhard, 2016; D'Onghia and Fox, 2016). The PM measurements favor a first-infall scenario (Besla et al., 2007), which is supported by the LMC's wake in the dark matter (DM) distribution of the MW halo (Conroy et al., 2021). The largest uncertainties in the orbits of the Clouds come from hydrodynamical effects including ram pressure and tidal energy losses, which are difficult to include in analytical integrators. Given the recent indications for the Magellanic Corona (see L20), as well as the need to include the MW's hot circumgalactic medium (CGM), these hydrodynamical effects will play a significant role in the orbital history of the Clouds. Upon the inclusion of the gaseous halos, we find that the Clouds can survive fewer recent interactions than previously thought (B12) if they are to remain separated at the present day. Additionally, evidence for a Magellanic Group (e.g. D'Onghia and Lake, 2008; Nichols et al., 2011) suggests that, being loosely bound, its two largest members should expect only a couple of direct interactions within the past $\sim$5$-$7 Gyr.

In this Letter we explore the large-scale structure and location of the Stream resulting from an alternate first-passage interaction history between the Clouds as motivated by the existence of the Magellanic Corona. Our new simulations are consistent with the observed PMs of the Clouds and have dramatic implications on the 3D location of the Magellanic Stream. In Section 3.2 we outline the methods and initial conditions used in our simulations. In Section 3.3 we discuss our main results, and in Section 3.4 we dissect the significant outcomes and implications of the model.

3.2 Methods

For this work, we used the GIZMO massively parallel, multiphysics code (Hopkins, 2015; Springel, 2005). GIZMO employs a Lagrangian meshless finite-mass (MFM) hydrodynamics scheme that is ideal for simulations with large bulk velocities and large dynamic ranges in density. The MFM scheme provides the ability to track individual fluid elements while still capturing Kelvin-Helmholtz instabilities and shocks (Hopkins, 2015). We used adaptive gravitational softening lengths for gas particles, and softening lengths of 350 and 100 pc for the DM and stellar components, respectively. Additionally, the default cooling (see Appendix B of Hopkins et al., 2018) and star formation (Springel and Hernquist, 2003) routines in GIZMO were included.

We do not include metal-line cooling, time-variable ionizing radiation from the MW disk, or UV background radiation in our model, because although these complex mechanisms would influence the Stream's thermal state and ionization level, we expect they would not affect its location, which is the focus of this Letter. Following L20, we assume the cold material (the H I Stream) originates from the disks of the LMC and SMC (the Magellanic ISM), whereas the warm ionized material originates from the Magellanic Corona.

3.2.1 Initial Conditions

The simulation presented here contains the same components as those used in L20, except we have added a live DM halo for the MW. In brief, those components are galaxies with stellar and gaseous exponential disks embedded in live Hernquist profile DM halos following the methods outlined in Springel (2005), and gaseous coronae around the LMC and MW. Table 3.1 outlines the parameters used to generate the initial setup of the simulation.

Table 3.1: Initial and Final Properties of the Galaxies in the Simulation.

	MW	LMC	SMC
v_{200} (km s^{-1})	166.1	92.72	45.22
DM Concentration[a]	12	9	15
DM Mass (M$_\odot$)	10^{12}	1.8×10^{11}	1.9×10^{10}
Stellar Mass (M$_\odot$)	4.8×10^{10}	5×10^{9}	2.6×10^{8}
Stellar Scale Length (kpc)	2.4	0.9	0.8
Disk Gas Mass (M$_\odot$)	10^{10}	5×10^{9}	1.6×10^{9}
Gas Scale Length (kpc)	7.0	2.8	2.0
Corona Mass (M$_\odot$)	4×10^{10}	8.3×10^{9}	–
Corona Temp (K)	2.4×10^{6}	2.4×10^{5}	–
N Particles	7.8×10^{6}	2.6×10^{6}	5.3×10^{5}
Initial Position (kpc)	(0, 0, 0)	(47.36, 546.38, 150.52)	(−19.79, 412.29, 183.75)
Initial Velocity (km s^{-1})	(0, 0, 0)	(1.71, −99.02, −63.73)	(13.43, −77.21, −80.33)
Sim Position (kpc)	–	(2.0, −40.8, −31.0)	(13.3, −39.3, −45.4)
Observed Position (kpc)	–	(−1.0, −40.9, −27.7)[e]	(14.9, −38.1, −44.2)[e]
Sim Velocity (km s^{-2})	–	(−101.1, −275.8, 229.2)	(−89.8, −300.1, 168.6)
Observed Velocity (km s^{-1})	–	(-57 ± 13, -226 ± 15, 221 ± 19)[e]	(18 ± 6, -179 ± 16, 174 ± 13)[f]
Sim PM[b,c] (mas yr^{-1})	–	($-2.18 \pm 0.02 \pm 0.23$, $0.20 \pm 0.01 \pm 0.28$)	($-1.10 \pm 0.02 \pm 0.45$, $-0.93 \pm 0.02 \pm 0.49$)
Observed PM[b] (mas yr^{-1})	–	(-1.91 ± 0.02, 0.23 ± 0.05)[e]	(-0.83 ± 0.12, -1.21 ± 0.04)[f]
Sim RV[d] (km s^{-1})	–	$262.2 \pm 6.2 \pm 12.5$	$165.8 \pm 5.0 \pm 32.0$
Observed RV (km s^{-1})	–	262.2 ± 3.4[g]	145.6 ± 0.6[h]

Notes. The resultant galaxies have rotation curve peaks of ~240, ~120, and ~65 km s^{-1} at 12, 8.5, and 5 kpc for the MW, LMC, and SMC respectively.

[a] The DM concentration parameter, c, is defined as the ratio of the virial radius, R_{vir}, to the Navarro-Frenk-White (NFW) scale radius, R_s: $R_{\mathrm{vir}} = cR_s$. The NFW scale radius is then converted into a Hernquist scale radius with $a = R_s\sqrt{2\left(\log(1+c) - c/(1+c)\right)}$.

[b] Proper motions given as (μ_W, μ_N) following the convention in Kallivayalil et al. (2013).

[c] Simulation PM errors are given as ($\mu_{W,N} \pm \mathrm{err}_\odot \pm \mathrm{err}_{\mathrm{res}}$), where $\mathrm{err}_\odot$ is the error due to the propagation of the uncertainties in the observed solar velocity and location via the bootstrapping method (solar values and errors from Kallivayalil et al. 2013, section 5). $\mathrm{err}_{\mathrm{res}}$ is an approximation of the variability in kinematics of the Clouds due to small-scale power effects, which change with the numerical resolution. It is computed by measuring the standard deviation of the resultant PMs and RVs in simulations of three different resolutions.

[d] Simulation radial velocity errors are given as ($v_{\mathrm{rad}} \pm \mathrm{err}_\odot \pm \mathrm{err}_{\mathrm{res}}$) with $\mathrm{err}_\odot$ and $\mathrm{err}_{\mathrm{res}}$ as defined above in c.

[e] Kallivayalil et al. (2013); [f] Zivick et al. (2018); [g] van der Marel et al. (2002); [h] Harris and Zaritsky (2006)

Based on recent measurements (Peñarrubia et al., 2016; Erkal et al., 2019), and the mounting evidence for a Magellanic Group (e.g. D'Onghia and Lake, 2008; Nichols et al., 2011), we include a high-mass LMC in our model. It has a total DM mass of 1.8×10^{11} M$_\odot$. Our SMC is consistent with previous works (P18; L20) with a DM mass of 1.9×10^{10} M$_\odot$. We use the MW model of D'Onghia and L. Aguerri (2020) with a gaseous component added to the disk. The total number of particles used for each galaxy is given in row 10 of Table 3.1, and leads to masses per particle ranging from 1.8×10^5 to 7.0×10^5 M$_\odot$ for DM, 4.2×10^3 to 1.6×10^4 M$_\odot$ for stars, and 4.3×10^3 to 1.8×10^4 M$_\odot$ for gas.

Following L20, we included a Magellanic Corona around the LMC and SMC by extracting the radial density profile from an LMC analog in the Auriga cosmological simulations (Grand et al., 2017), although we used slightly different selection criteria. Specifically, we selected all gas with

$T > 2.5 \times 10^4$ K, the lowest temperature at which the galaxy's disk gas was excluded from the selection. The corona was then added around our LMC with its total mass scaled by the ratio between the Auriga LMC analog's total mass and our LMC's total mass, leading to a mass of 8.3×10^9 $\mathrm{M}_\odot$ in the Magellanic Corona and a density of 10^{-4} cm^{-3} at 50 kpc from the LMC. Finally the corona's temperature was set to 2.4×10^5 K, the expected virial temperature of the LMC. These values are also consistent with other recent cosmological simulations (Hafen et al., 2019; Jahn et al., 2021). Run in isolation for 4 Gyr, the LMC and Magellanic Corona remain stable.

Around the MW, we initially included a gaseous corona following the "fiducial" density profile in Salem et al. (2015): a β-profile with $n_0 = 0.46$ cm^{-3}, $r_c = 0.35$ kpc, and $\beta = 0.559$. The maximum density was capped within 13 kpc from the Galactic Center where the corona overlapped with the gaseous disk. Additionally, the profile exponentially declines for $r > r_{\mathrm{vir}} = 166$ kpc. This initial simulation was unable to reproduce the velocity profile of the Stream (see Section 3.3), so in the final simulation presented here, the total mass was increased by a factor of two to 4×10^{10} $\mathrm{M}_\odot$, which solved the kinematic discrepancy. This increased the MW halo density at 50 kpc from 1.1×10^{-4} to 2.0×10^{-4} cm^{-3}, still consistent with current data (e.g. Anderson and Bregman 2010; Li and Bregman 2017). We acknowledge that the Galactic and Magellanic Coronae included in these simulations are simplified when compared with the complex multiphase intricacies known to exist in circumgalactic media (van de Voort et al., 2019).

3.2.2 Orbits

The orbits used in previous simulations of Magellanic Stream formation were established without the Galactic or Magellanic Coronae included (B12; P18). While the Cloud orbits will clearly require modification due to the changes in total masses of the galaxies due to these added components, the increased friction and ram pressure that the Clouds experience as they move through these media also play a significant role. Therefore, to match the observed positions and velocities of the Magellanic Clouds while including the Galactic and Magellanic Coronae in our simulations, we need to determine an alternate orbital history with fewer recent interactions between the Clouds.

To do this, we analytically integrated the orbits of the LMC, SMC, and MW backward in time starting from their present-day observed positions and velocities. We included radially extended

Hernquist DM halos including dynamical friction and represented the stellar and gaseous disks as point particles. By varying the present-day velocities within the observed errors, we obtained a suite of 1458 possible orbits. We filtered these to select first-passage orbits with multiple interactions between the Clouds. These orbits are generally consistent with the results found with previous analytic integrations after accounting for differences in LMC mass and live versus static MW DM halos (Besla et al., 2007; Kallivayalil et al., 2013; Garavito-Camargo et al., 2019). We then chose 10 of these orbits sampling the parameter space with varying morphologies to run in full N-body hydrodynamical simulations. Due to the effects of tidal stripping, ram pressure, and friction, the initial conditions required modification to match the present-day observations of the Clouds. For 9 of the 10 chosen orbits, we were unable to modify them such that they reproduced the present-day observations. However, after a few iterations on one of the orbits, we found a solution that could match the Clouds' observed kinematic properties, which we present in this Letter. The initial positions and velocities used for the orbits in this simulation are given in rows 11 and 12 of Table 3.1.

Given the backward-integrated orbits, we had to choose when to begin the N-body simulation. We chose the apocenter between the Clouds after their second interaction (3.5 Gyr ago). While the Clouds would have another encounter if we integrate these orbits further back in time, this interaction would occur 7 Gyr ago (5.5 Gyr before their next interaction) at a distance of 0.9 Mpc away from the MW. Any gas stripped in this interaction would be tidally thrown out to great distances from the Clouds and become too diffuse and distant to contribute to the Stream today (see material stripped from the first interaction in Figure 2 of P18).

Comparison with Previous Orbits

In the previous orbital model of B12 and P18 (B12's "Model 2"), the LMC and the SMC experience three interactions in isolation (without any MW influence) over ∼6 Gyr. They are then rotated into the correct orientation, placed at the virial radius of the MW, and allowed to continue evolving until they reach their present-day positions (∼1 Gyr). During this infall they experience an additional direct collision that forms the Magellanic Bridge.

In the model presented here, all the interactions between the Clouds and the MW occur in a single, self-consistent simulation lasting 3.5 Gyr. The LMC and the SMC have two interactions,

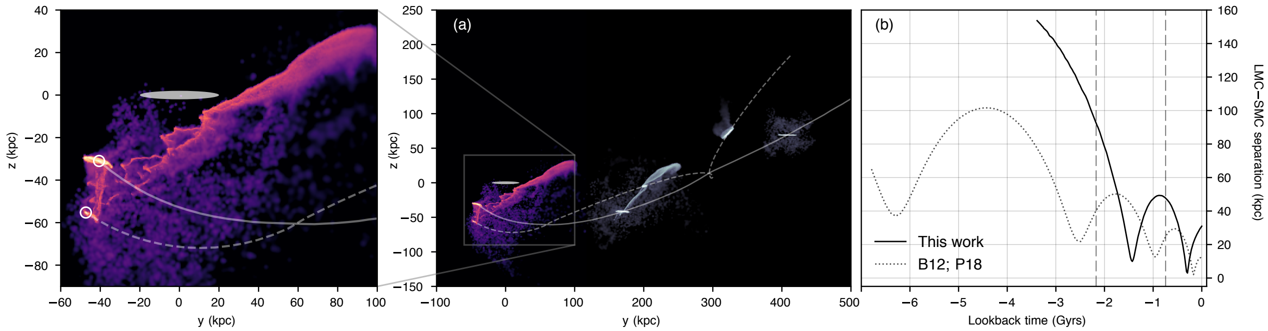

Figure 3.1: The orbital history of the Magellanic Clouds. Panel (a) shows the Magellanic Stream in Cartesian coordinates at three different times during the Clouds' infall. The present-day Stream is shown in color. The MW disk is at the origin and denoted by the gray shaded oval (the sun is located at $(x, y, z) = (-8.3, 0, 0.027)$ kpc). The solid and dashed lines represent the past orbital trajectories of the LMC and SMC, respectively. A zoomed inset of the present-day Stream can be seen in the panel on the left with the locations of the Clouds in the simulation marked with circles. The color of the gas represents plane-projected density on an arbitrary scale with higher densities represented as lighter colors. Panel (b) shows the distance between the center of masses of the LMC and SMC in kpc as they orbit around each other and fall in toward the MW. The model presented here is compared with previous works (shown as a dotted line; B12; P18). Present day is on the right side of the plot ($t = 0$), and the Clouds' initial state is on the left side ($t = -3.5$ Gyr for the present work). Vertical dashed lines denote the times of the two past images in panel (a) (shown in gray scale).

the second of which has a very low impact parameter and forms the Magellanic Bridge. The main differences between these two orbital models are (see Figure 3.1b):

- the number of interactions (4 versus 2),
- the length of the simulation (7 versus 3.5 Gyr),
- the maximum separation between the Clouds (100 versus 150 kpc), and
- the sense of the SMC's orbit around the LMC (see Section 3.4 and Figure 3.4).

While there have been many other proposed orbital models of the interactions between the Clouds (e.g. Růžička et al., 2010; Diaz and Bekki, 2011; Guglielmo et al., 2014), none have looked at this explicit combination, especially when considering a first-passage scenario with the inclusion of an MW CGM and the Magellanic Corona.

3.3 Results

The simulation ran for 3.46 Gyr, when the positions and velocities of the Clouds matched current observations just after their first pericentric passage. When the LMC and SMC are at their present-day sky positions in our model, they are at distances of 52.1 ± 1.7 kpc and 78.0 ± 7.8 kpc respectively (with errors calculated as err_{res} discussed in footnote c of Table 3.1; $\text{err}_{\odot}$ are negligible), with proper motions and radial velocities listed in Table 3.1. The kinematics of the Clouds are fully consistent with the observed values: within 1σ for the proper motions and radial velocity for both the LMC and the SMC (with the exception of μ_W for the LMC at 1.18σ). Additionally, the relative velocity between the Clouds (66 km s^{-1}) matches within 2σ.

The present-day disk gas masses[1] for the LMC and SMC are 4.4×10^8 and 3.3×10^7 $\text{M}_{\odot}$ respectively (with peak column densities of $10^{21.8}$ and $10^{21.4}$ cm^{-2}). A full exploration of the structure of the Clouds themselves will be performed in an upcoming paper with more complete star formation and feedback routines.

Throughout their 3.5 Gyr interaction history, a trailing Stream is formed through tidal interactions between the Clouds. The orbital paths of the LMC and SMC along with the resultant Stream at the present day are shown projected onto the y–z plane relative to the MW disk in Figure 3.1a. The LMC and SMC experience two close encounters shown as minima in Figure 3.1b. Their first interaction, 1.4 Gyr ago with an impact parameter of 9.9 kpc, provides the tidal forces necessary to strip material from the SMC to create the bulk of the H I Stream. Their second interaction, 295 Myr ago, has a significantly lower impact parameter of 3.0 kpc, and this direct collision forms the Magellanic Bridge. The present-day position of the Magellanic System can also be seen in 3D in Figure 3.2.

To test the dominant stripping mechanism in our model, we ran two additional simulations: one consisting of just the MW, its hot corona, and the SMC (without the LMC), and another with the MW, its hot corona, and the LMC with the Magellanic Corona (without the SMC). When the SMC alone passes through the MW's CGM, we find only 8% of the total gas mass stripped from the full model. When the LMC alone passes through, we find negligible stripping of gas from the LMC, but the Magellanic Corona still sees 95% of the stripping of the full model. Therefore, we conclude that the neutral Stream is stripped through tidal forces (consistent with previous findings; e.g. Salem et al. 2015), whereas the ionized component of the Stream (originating in the Magellanic Corona) is stripped mostly through ram pressure against the MW hot corona, even during the first

---

[1] These masses were calculated in physical 3D space by summing the particle masses within spheres centered on each galaxy with diameters 13.5 kpc for the LMC, and 5.5 kpc for the SMC.

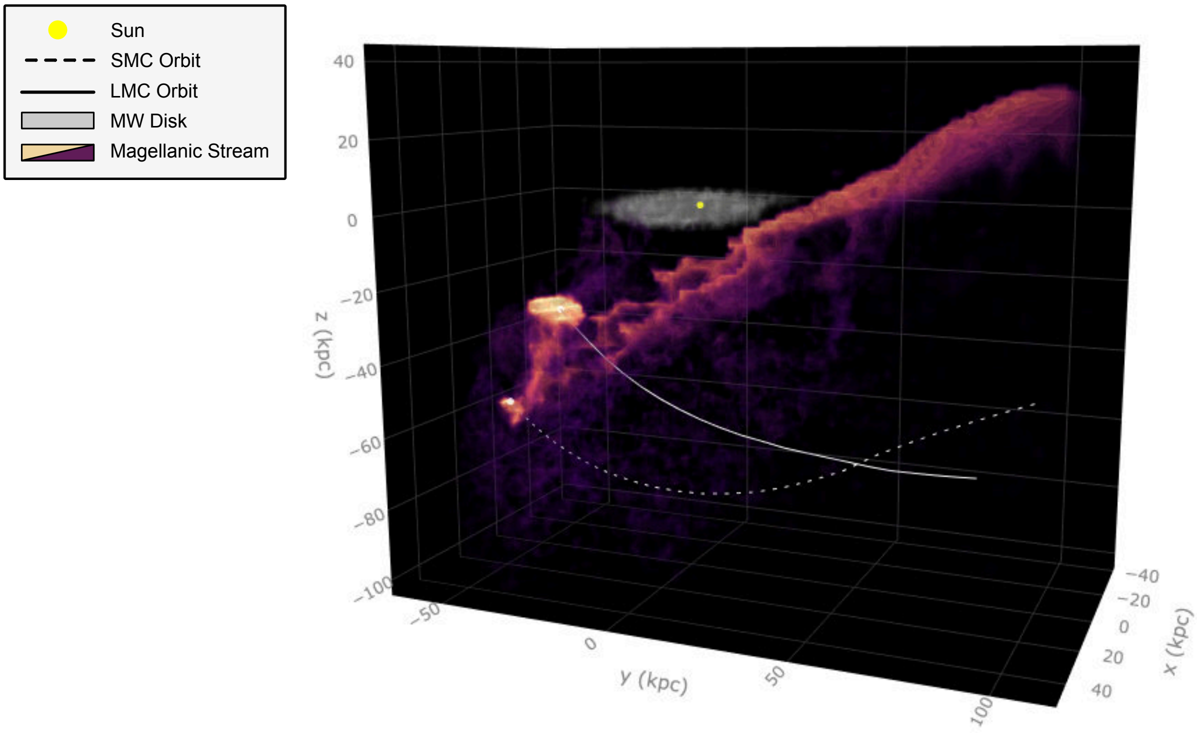

Figure 3.2: A 3D model of the Magellanic Stream. The orbits of the LMC and SMC are shown as solid and dashed lines, respectively. The MW disk is shown in gray with the location of the Sun marked with a yellow sphere.

passage.

As in L20, the bulk of the mass of the Magellanic Stream is composed of ionized gas originating in the Magellanic Corona. However, the distribution of the ionized Magellanic Corona gas on the sky is substantially different in our new model (compare Figure 3.3(c) with L20 Figure 2(a)), but the neutral Stream's appearance on the sky in our model is generally consistent with previous models and observations (Figure 3.3(a), (b), (d)). While the simulated Stream is longer than observed and slightly offset spatially, the morphology of the Stream in this model more accurately reproduces the turbulent, filamentary nature of the data. Due to its interactions with the Magellanic Corona and the MW's hot CGM, instabilities fragment and distort the Stream, leading to a significant improvement in its appearance and morphology when compared to models that do not include these gaseous components (e.g.P18).

The velocity profile of our simulated Stream also matches observations (see Figure 3.3e). Previous models found a velocity gradient (v_{LSR} vs Magellanic longitude) too shallow when compared

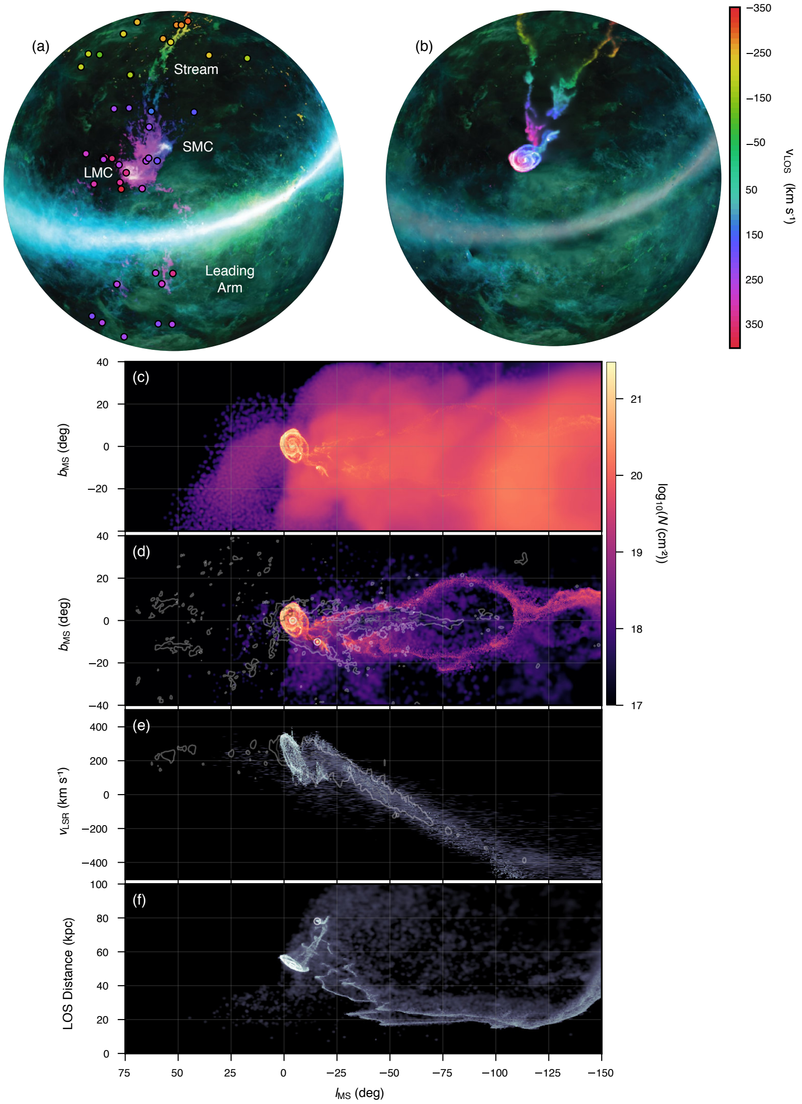

Figure 3.3: Properties of the Magellanic Stream produced in our simulations. Panels (a) and (b) show the observed and simulated Stream respectively in zenithal equal-area coordinates with line-of-sight velocity indicated by the color scale and the relative gas column density indicated by the brightness. The H I data in Panel (a) are from the GASS survey (McClure-Griffiths et al., 2009) with the points showing sight lines with UV-absorption-line observations from the Hubble Space Telescope (Fox et al., 2014) colored by their line-of-sight velocity. Panel (c) shows the column density of the total gas in the Stream (including the ionized Magellanic Corona and neutral Magellanic disk components) in Magellanic Coordinates ($l_{\rm MS}$ and $b_{\rm MS}$). Panel (d) only shows the neutral gas originating in the disks of the LMC and SMC compared to the observed data from Nidever et al. (2010) shown in contours (black, gray, and white correspond to 10^{21}, 10^{20}, and 10^{19} cm^{-2}). The centroids of the LMC and SMC stellar disks are marked by white circles. Panel (e) shows the local standard of rest (LSR) velocity gradient along the Stream with data shown as contours (Nidever et al., 2010). Panel (f) shows the line-of-sight distance to the gas in the Stream along its length with the centroids of the Clouds marked with circles. Note that the bulk of the simulated Stream is significantly closer to us than the Magellanic Clouds are (∼20 kpc vs. ∼60 kpc).

to the data (L20), but this is resolved in our new model. As stated in Section 3.2.1, the density profile and total mass of the MW hot corona were increased by a factor of 2 over the Salem et al. (2015) values to better match the velocity gradient along the Stream. If the MW's hot halo is not massive enough, the stripped gas from the Clouds is accelerated toward the MW and in some cases ends up with greater velocities than the LMC and SMC themselves. A higher gas density around the MW provides the ram pressure forces to slow down the trailing Stream to match the observed velocity gradient. This is in contrast to previous works that placed upper limits on the MW coronal mass such that a Leading Arm can form (Tepper-García et al. 2019; L20).

Additionally, as seen in Figure 3.3d, this model does not self-consistently reproduce the Leading Arm gas. This is because the Clouds only have two close encounters so there is not enough time for gas to be tidally thrown ahead of the Clouds in their orbits. This is in contrast to previous studies (Tepper-García et al. 2019; L20) where the lack of a Leading Arm was due to the MW hot coronal density being too high. In this new model, even without an MW hot corona, a Leading Arm is not formed. The true nature of the Leading Arm is one of the biggest outstanding questions in the Magellanic System (D'Onghia and Fox, 2016). While a Magellanic origin is supported by the kinematics (Putman et al., 1998) and the metallicities (although they vary with position; Fox et al., 2018), several works have proposed alternative, non-Magellanic sources. Hammer et al. (2015) and Tepper-García et al. (2015) suggested the Leading Arm structures could be remnants from dwarf spheroidal satellites of the MW whose gas has been stripped from the MW hot corona, and a non-Magellanic explanation for the Leading Arm remains a possibility.

The most notable implication of this new model is that the Stream is significantly closer to us than previously thought (Figure 3.3f). While some past models have predicted a close Stream (via multiple passages around the MW; e.g. Moore and Davis 1994; Diaz and Bekki 2012), all previous first-passage orbits have resulted in the Stream flowing behind the Clouds out to distances of $100 - 200$ kpc or greater (see Figure 3.4e; B12; P18; L20). The first-passage model presented here forms a tidal Stream that reaches as close as $\sim$20 kpc away from the Sun with a column density-weighted average distance of 24.7 kpc (between Magellanic longitudes of $-25°$ and $-150°$). See Section 3.4 for an in-depth discussion of this finding.

We emphasize that in all our simulations that formed a Stream (7 of the 10 selected from the backward integration, see Section 3.2.2), that Stream was <50 kpc away from us. While the distances and kinematics of the Clouds, and the Stream morphology, vary greatly between these individual simulation runs, the finding that the Stream remains nearby is a robust prediction of our first-infall models. Additionally, we have run several convergence tests at various numerical resolutions, and despite minor differences on small scales, all runs produced accurate positions and velocities for the Clouds, and all predicted a nearby Stream with total ionized and neutral masses consistent with observations.

3.4 Discussion and Conclusions

The new first-passage interaction history of the Magellanic Clouds presented here leads to a dramatically different 3D spatial positioning of the Stream than previous models. Previous first-passage, tidal simulations led to a Stream extending away from the Clouds out to distances upward of 200 kpc, whereas our new model results in the Stream angling up toward the MW reaching as close as 20 kpc to the Sun. While there are many differences between previous models and the model presented here (see Section 3.2.2), two differences in particular lead to this dramatic shift in positioning of the Stream:

1. a qualitative difference in the SMC's orbit around the LMC, and
2. the inclusion of the Galactic and Magellanic Coronae.

First, the orientation of the SMC's orbit around the LMC is qualitatively different than the most recent previous models (B12; P18; L20). To compare these different orbital histories, we need to analyze the orbits in a consistent coordinate system, so we will discuss the relative motion of the SMC around the LMC when viewed projected onto the y–z plane as defined in Figure 3.1 (relative to the MW disk, which is in the x–y plane with the Sun located at $(x, y, z) = (-8.3, 0, 0.027)$ kpc)[2]. When viewed from this perspective, our model has the SMC on a *counterclockwise* orbit around the LMC, whereas in the B12 model, the SMC rotates around the LMC *clockwise*. In the *clockwise* orbit, the Stream is tidally thrown out in the $+y$ direction with a velocity in the $-z$ direction, leading to it stretching away from the MW disk. Whereas in the *counterclockwise* orbit, the Stream is

---

[2] Note that this is the same perspective as Figure 3 in B12 but is not consistent with the coordinate systems in B12's Figure 2, L20's Extended Data Figure 2, or P18's Figure 2. Because of rotations performed before the Clouds fall into the MW potential in these models, the y–z perspective discussed above is approximately equivalent to mirroring these figures across the y-axis.

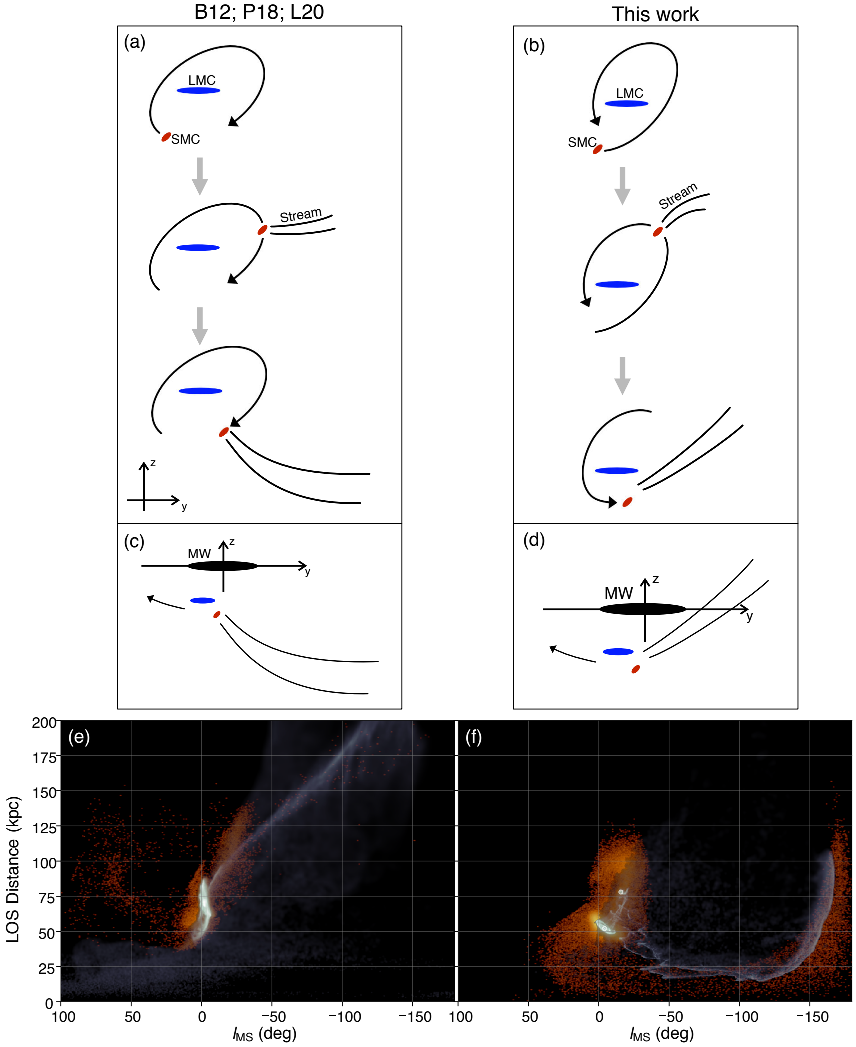

Figure 3.4: Orbital schematics and distance to the Magellanic Stream compared for two different models. The left column (panels (a), (c), and (e)) shows the clockwise orbit of previous works (B12; P18; L20), while the right column (panels (b), (d), and (f)) shows the counterclockwise orbit used in the model presented here. In panels (a) and (b), the orbital path of the SMC (red) around the LMC (blue) is shown at three different times in the y–z plane: before the interaction (top), at apoapsis when the Stream material is stripped out of the SMC (middle), and at their present-day orientation (bottom). Panels (c) and (d) show the present-day positions of the Clouds and the Stream in the two models with respect to the MW, again in the y–z plane. The arrow shows the direction of motion of the Clouds around the MW. Panels (e) and (f) both show line-of-sight distance to the gas in the simulated Stream (gray) and the stars in the Stream (orange). In previous orbital models (left column), the Stream stretches out and away from the MW leading to distances of 100–200 kpc. Whereas in the new orbital history presented here (right column), the Stream is stripped during the SMC's counterclockwise motion around the LMC and then pushed into place through the ram pressure and frictional forces of the MW's CGM leading to distances of as little as ∼20 kpc.

still tidally stripped in the $+y$ direction, but its velocity is in the $+z$ direction. This leads to a Stream angled up in the $+y$ and $+z$ directions, resulting in low line-of-sight distances to the Sun. A schematic of these two orbital orientations is shown in Figure 3.4(a)-(d).

Second, the inclusion of the Galactic and Magellanic Coronae is crucial. While previous parameter space searches of orbits for the Clouds would possibly have explored this orbital configuration in the past (e.g. Růžička et al., 2010; Guglielmo et al., 2014), none included the Galactic and Magellanic Coronae. These are key elements as the ram pressure and friction from the MW's CGM are able to "push" the Stream into its present-day position and velocity. Without the MW's gaseous halo, the Stream would collide with the MW disk before the Clouds reach their present-day positions. Moreover, the Magellanic Corona is required to shield the neutral Stream from the intense forces and pressures as it moves through high-density regions of the Galactic corona L20.

A Stream reaching $\sim$20 kpc has a number of implications. First, the total observed mass (neutral and ionized) of the Stream would be reduced. Total mass estimates of the Stream have previously assumed the Stream has a similar distance as the Clouds (55 kpc), but they include a scale factor of $(d/55 \text{ kpc})^2$ which equals 0.2 for $d = 24.7$ kpc (the column density-weighted average distance in the simulation). This leads to new values of 9.7×10^7 M$_\odot$ of neutral gas (Brüns et al., 2005) and 4×10^8 M$_\odot$ of ionized gas (Fox et al., 2014), although this ionized gas mass should be considered as a lower limit as the spatial extent of the Stream's ionized phase may be significantly greater than the area on the sky that has currently been explored, and the ionized gas may be multiphase (Fox et al., 2014). Summing the masses of all gravitationally unbound particles that fall in the region of the trailing Stream in our simulation gives values of 2.0×10^8 M$_\odot$ (neutral) and 3.2×10^9 M$_\odot$ (ionized) for our model of the Stream, in good agreement with the observations. Second, as shown in Figure 3.4f, the stellar component of the Stream is also nearby, with stars predicted at $d \lesssim 20$ kpc (with a mean surface brightness of 31 mag arcsec^{-2}). Previous works have predicted that any stars associated with the Magellanic System are at large distances (B12; P18), but our new predictions suggest that continued searches for the Stream's stellar component are worthwhile (Zaritsky et al., 2020). Third, the interaction between the Stream and the MW CGM will be enhanced due to its proximity, because of the higher MW corona density. At a closer distance, the Stream would be closer to pressure equilibrium with the MW CGM, which could help explain its multiphase nature (Wolfire et al., 1995) and the high number of "head-tail" clouds seen in high-resolution H I observations (For et al., 2014). It could also lead to dramatically shorter lifetimes for the Stream in the future (Murali, 2000; Bland-Hawthorn et al., 2007). Indeed, due to its angle of approach with respect to the MW, the Stream may even directly collide with the MW disk within the next $\sim$50 Myr. This moves the timescale of gas accretion onto the disk up by a factor of $\sim$10 from previous predictions. The new distance to the Stream therefore implies a factor of $\sim$8 less gas accreting onto the MW $\sim$10 times earlier than previously thought, resulting in approximately the same infall rate of $\sim$4–7 $\mathrm{M_\odot\ yr^{-1}}$ as derived before (Fox et al., 2014). Fourth, a closer Stream should be subject to a more intense UV radiation field from the MW and hence significantly brighter in H α. This could explain the high observed H α emission from the Stream (Bland-Hawthorn et al., 2013; Bland-Hawthorn et al., 2019; Barger et al., 2017); at a distance of 20 kpc, the Galactic UV background could lead to H α emission as high as $150 - 300$ mR (Tepper-García et al., 2015), in agreement with observed levels along most of the Stream. However, this increased radiation still cannot explain the extremely high H α emission seen in the region of the Stream under the South Galactic Pole, which may indicate a recent Seyfert flare from the Galactic Center (Bland-Hawthorn et al., 2019). The enhanced radiation field intensity at d=20 kpc would also affect the ionization level inferred from UV metal-line studies of the Stream (Fox et al., 2014; Fox et al., 2020); however, the ionized/neutral ratio of $\sim$3:1 is distance independent since both the neutral and ionized masses scale as d^2.

There are currently no observational distance constraints on the Stream, although parts of the Leading Arm have constraints of $< 20 - 30$ kpc (McClure-Griffiths et al., 2008; Price-Whelan et al., 2018; Antwi-Danso et al., 2020). To test our prediction of a 20 kpc Stream, UV or optical spectroscopic studies could be performed to look for absorption at Magellanic velocities toward distant MW halo stars, such as blue horizontal branch stars with distances from Gaia. Lehner and Howk (2011) found no UV absorption at Magellanic velocities when looking at 28 halo stars out to z-distances of 12.6 kpc, but searches to larger distances using new stellar catalogs are needed. This offers a pathway for confirming our prediction of a nearby Stream.

REFERENCES

Anderson, M. E. and Bregman, J. N. 2010, *ApJ*, 714, 320–331, `10.1088/0004-637X/714/1/320`.

Antwi-Danso, J., Barger, K. A., and Haffner, L. M. 2020, *ApJ*, 891, 176, `10.3847/1538-4357/ab6ef9`.

Barger, K. A., et al. 2017, *ApJ*, 851, 110, `10.3847/1538-4357/aa992a`.

Besla, G., et al. 2007, *ApJ*, 668, 949–967, `10.1086/521385`.

Besla, G., et al. 2012, *MNRAS*, 421, 2109–2138, `10.1111/j.1365-2966.2012.20466.x`.

Bland-Hawthorn, J., et al. 2013, *ApJ*, 778, 58, `10.1088/0004-637X/778/1/58`.

Bland-Hawthorn, J. and Gerhard, O. 2016, *ARA&A*, 54, 529–596, `10.1146/annurev-astro-081915-023441`.

Bland-Hawthorn, J., et al. 2007, *ApJ*, 670, L109–L112, `10.1086/524657`.

Bland-Hawthorn, J., et al. 2019, *ApJ*, 886, 45, `10.3847/1538-4357/ab44c8`.

Brüns, C., et al. 2005, *A&A*, 432, 45–67, `10.1051/0004-6361:20040321`.

Conroy, C., et al. 2021, *Nature*, 592, 534–536, `10.1038/s41586-021-03385-7`.

D'Onghia, E. and Fox, A. J. 2016, *ARA&A*, 54, 363–400, `10.1146/annurev-astro-081915-023251`.

D'Onghia, E. and L. Aguerri, J. A. 2020, *ApJ*, 890, 117, `10.3847/1538-4357/ab6bd6`.

D'Onghia, E. and Lake, G. 2008, *ApJ*, 686, L61, `10.1086/592995`.

Diaz, J. and Bekki, K. 2011, *MNRAS*, 413, 2015–2020, `10.1111/j.1365-2966.2011.18289.x`.

Diaz, J. D. and Bekki, K. 2012, *ApJ*, 750, 36, `10.1088/0004-637X/750/1/36`.

Erkal, D., et al. 2019, *MNRAS*, 487, 2685–2700, `10.1093/mnras/stz1371`.

For, B.-Q., et al. 2014, *ApJ*, 792, 43, `10.1088/0004-637X/792/1/43`.

Fox, A. J., et al. 2014, *ApJ*, 787, 147, `10.1088/0004-637X/787/2/147`.

Fox, A. J., et al. 2018, *ApJ*, 854, 142, `10.3847/1538-4357/aaa9bb`.

Fox, A. J., et al. 2020, *ApJ*, 897, 23, `10.3847/1538-4357/ab92a3`.

Fujimoto, M. and Sofue, Y. 1977, *A&A*, 61, 199–215.

Garavito-Camargo, N., et al. 2019, *ApJ*, 884, 51, `10.3847/1538-4357/ab32eb`.

Gardiner, L. T. and Noguchi, M. 1996, *MNRAS*, 278, 191–208, `10.1093/mnras/278.1.191`.

Grand, R. J. J., et al. 2017, *MNRAS*, 467, 179–207, `10.1093/mnras/stx071`.

Guglielmo, M., Lewis, G. F., and Bland-Hawthorn, J. 2014, *MNRAS*, 444, 1759–1774, `10.1093/mnras/stu1549`.

Hafen, Z., et al. 2019, *MNRAS*, 488, 1248–1272, `10.1093/mnras/stz1773`.

Hammer, F., et al. 2015, *ApJ*, 813, 110, `10.1088/0004-637X/813/2/110`.

Harris, J. and Zaritsky, D. 2006, *AJ*, 131, 2514–2524, `10.1086/500974`.

Hopkins, P. F. 2015, *MNRAS*, 450, 53–110, `10.1093/mnras/stv195`.

Hopkins, P. F., et al. 2018, *MNRAS*, 480, 800–863, `10.1093/mnras/sty1690`.

Jahn, E. D., et al. 2021, *arXiv e-prints*, arXiv:2106.03861.

Kallivayalil, N., et al. 2013, *ApJ*, 764, 161, `10.1088/0004-637X/764/2/161`.

Lehner, N. and Howk, J. C. 2011, *Science*, 334, 955, `10.1126/science.1209069`.

Li, Y. and Bregman, J. 2017, *ApJ*, 849, 105, `10.3847/1538-4357/aa92c6`.

Lucchini, S., et al. 2020, *Nature*, 585, 203–206, `10.1038/s41586-020-2663-4`.

McClure-Griffiths, N. M., et al. 2008, *ApJ*, 673, L143, `10.1086/528683`.

McClure-Griffiths, N. M., et al. 2009, *ApJ Supplement*, 181, 398–412, `10.1088/0067-0049/181/2/398`.

Moore, B. and Davis, M. 1994, *MNRAS*, 270, 209–221, `10.1093/mnras/270.2.209`.

Murali, C. 2000, *ApJ Letters*, 529, L81–L84, `10.1086/312462`.

Nichols, M., et al. 2011, *ApJ*, 742, 110, `10.1088/0004-637X/742/2/110`.

Nidever, D. L., et al. 2010, *ApJ*, 723, 1618–1631, `10.1088/0004-637X/723/2/1618`.

Pardy, S. A., D'Onghia, E., and Fox, A. J. 2018, *ApJ*, 857, 101, `10.3847/1538-4357/aab95b`.

Peñarrubia, J., et al. 2016, *MNRAS*, 456, L54–L58, `10.1093/mnrasl/slv160`.

Price-Whelan, A. M., et al. 2018, *arXiv e-prints*, arXiv:1811.05991.

Putman, M. E., et al. 1998, *Nature*, 394, 752–754, `10.1038/29466`.

Růžička, A., Theis, C., and Palouš, J. 2010, *ApJ*, 725, 369–387, `10.1088/0004-637X/725/1/369`.

Salem, M., et al. 2015, *ApJ*, 815, 77, `10.1088/0004-637X/815/1/77`.

Springel, V. 2005, *MNRAS*, 364, 1105–1134, `10.1111/j.1365-2966.2005.09655.x`.

Springel, V. and Hernquist, L. 2003, *MNRAS*, 339, 289–311, `10.1046/j.1365-8711.2003.06206.x`.

Tepper-García, T., Bland-Hawthorn, J., and Sutherland, R. S. 2015, *ApJ*, 813, 94, `10.1088/0004-637X/813/2/94`.

Tepper-García, T., et al. 2019, *MNRAS*, 488, 918–938, `10.1093/mnras/stz1659`.

van de Voort, F., et al. 2019, *MNRAS*, 482, L85–L89, `10.1093/mnrasl/sly190`.

van der Marel, R. P., et al. 2002, *AJ*, 124, 2639–2663, `10.1086/343775`.

Wang, J., et al. 2019, *MNRAS*, 486, 5907–5916, `10.1093/mnras/stz1274`.

Wolfire, M. G., et al. 1995, *ApJ*, 453, 673, `10.1086/176429`.

Zaritsky, D., et al. 2020, *ApJ Letters*, 905, L3, `10.3847/2041-8213/abcb83`.

Zivick, P., et al. 2018, *ApJ*, 864, 55, `10.3847/1538-4357/aad4b0`.

CHAPTER 4

THE MAGELLANIC CORONA: A SYSTEMATIC EXPLORATION OF TIDAL FORMATION OF THE MAGELLANIC STREAM

Abstract

We present a survey of the tidal Magellanic Corona model of the formation of the Magellanic Stream. Using cutting edge, high-resolution hydrodynamic simulations we constrain the properties of the Magellanic Clouds before their infall into the Milky Way, including the gaseous halo of the Large Magellanic Cloud (LMC), the Magellanic Corona. With an LMC mass of 1.75×10^{11} $M_{\odot}$, a Corona of $> 5 \times 10^{9}$ $M_{\odot}$ at 3×10^{5} K, a total Small Magellanic Cloud mass $< 10^{10}$ $M_{\odot}$, and a Milky Way circumgalactic medium of 2×10^{10} $M_{\odot}$, we reproduce the observed total mass of the neutral and ionized components of the Trailing Stream, ionization fractions along the Stream, morphology of the neutral gas, and on-sky extent of the ionized gas. The stripped material is also suggestive of a nearby Stream, as found in prior models including a Magellanic Corona. Alternative orbital models are also able to self-consistently produce a Leading Arm with morphology, column density distribution, and total gas mass in excellent agreement with the H I observations. While the Trailing Stream in these specific simulations do match the data as well as other models, this is the first time the morphology of the Leading Arm has been reproduced with Magellanic material.

4.1 Introduction

The Magellanic Stream is the largest coherent extragalactic gaseous structure in our sky. It has the potential to dramatically impact the future of the Milky Way by depositing billions of solar masses of gas into our circumgalactic medium (CGM) and possibly onto our disk (Fox et al., 2014; D'Onghia and Fox, 2016). The Magellanic Stream is also direct evidence of galaxy interactions and evolution through mergers. By studying this serendipitous nearby system, we will learn about the future of our own Galaxy, the history of the Local Group, galaxy evolution in general (for $L*$ and dwarf galaxies), and the gas and metal transport processes that can sustain the growth of galaxies like our Milky Way.

The Magellanic Stream is an extended network of interwoven clumpy filaments of gas that originate from within the Large and Small Magellanic Clouds (LMC, SMC), two dwarf galaxy satellites of the Milky Way (MW). Combined with the Leading Arm, high velocity clumps of gas ahead of the Magellanic Clouds in their orbits, the Magellanic System covers over 200° on the sky. From all-sky H I surveys, we have an excellent view of its small-scale, turbulent morphology as well as its velocity structure (e.g. Nidever et al., 2008; Nidever et al., 2010; Westmeier, 2018). Moreover, absorption line spectroscopy studies have characterized the chemical composition and ionization state of the Stream along dozens of sightlines (Lu et al., 1994; Gibson et al., 2000; Sembach et al., 2003; Fox et al., 2010; Fox et al., 2013; Richter et al., 2013; Fox et al., 2014). Fox et al. (2014) has shown that the Stream is mostly ionized. They find an average ionization fraction of 73% with a total ionized gas mass of $\sim 1.5 \times 10^9$ $M_\odot$ (compared with 4.9×10^8 $M_\odot$ of neutral gas; Brüns et al. 2005).

Models of the formation of the Stream originally explained the stripped material as gas that was tidally pulled from the LMC through repeated interactions with the MW (Fujimoto and Sofue, 1976; Davies and Wright, 1977; Lin and Lynden-Bell, 1977; Lin and Lynden-Bell, 1982; Gardiner and Noguchi, 1996; Connors et al., 2006; Diaz and Bekki, 2011). This would result not only in stripped gas, but also in a tidally truncated dark matter halo. Thus, masses determined by rotation curve fitting ($1.7 \pm 0.7 \times 10^{10}$ $M_\odot$ within 8.7 kpc, van der Marel and Kallivayalil, 2014) would be sufficient for modeling the evolution of the Clouds and the formation of the Stream. However, updated proper motion measurements of the LMC and SMC have shown that the Clouds are most likely on their first infall towards the Milky Way (Kallivayalil et al., 2006; Besla et al., 2007; Kallivayalil et al., 2013). This would require a higher LMC mass as it would not yet be tidally truncated. Many different indirect methods of estimating the LMC's total pre-infall mass have converged on a value of $1 - 2 \times 10^{11}$ $M_\odot$: 1.98×10^{11} $M_\odot$ from abundance matching (Read and Erkal, 2019), $>10^{11}$ $M_\odot$ from the MW's reflex motion (Petersen and Peñarrubia, 2021), $>1.24\times10^{11}$ $M_\odot$ from the LMC's satellite population (Erkal and Belokurov, 2020), $2.5^{+0.09}_{-0.08} \times 10^{11}$ $M_\odot$ from the Hubble flow timing argument (Peñarrubia et al., 2016), and $1-2\times10^{11}$ $M_\odot$ from the MW's stellar streams (Erkal et al., 2019; Shipp et al., 2021). See Figure 4.1 for a summary. Shown in this figure is also the error-weighted mean of the values calculated in Vasiliev et al. (2021), Shipp et al. (2021), Erkal et al. (2019), Read and Erkal (2019), and Peñarrubia et al. (2016): $1.60 \pm 0.21 \times 10^{11}$ $M_\odot$ ($\sim 10 - 20\%$ of the MW's total mass).

While modern tidal models of the formation of the Stream have used large masses for the LMC, they are unable to explain the immense ionized mass (Besla et al., 2010; Besla et al., 2012; Pardy et al., 2018). On the other hand, ram pressure models are able to explain the ionized material via dissolution of the neutral gas through instabilities, but they require low masses for the LMC ($< 2 \times 10^{10}$ $M_\odot$; Hammer et al., 2015; Wang et al., 2019).

To resolve both of these discrepancies simultaneously, we introduced the Magellanic Corona model (Lucchini et al., 2020; Lucchini et al., 2021). Based on theoretical calculations and cosmological simulations, galaxies with masses $\sim 10^{11}$ $M_\odot$ should host gaseous halos at their virial temperature of $\sim 3 \times 10^5$ K[1]. Upon inclusion of a warm CGM around the LMC, dubbed the Magellanic Corona, we are able to explain the ionized material in the Stream while accounting for a massive LMC. In Lucchini et al. (2021), we showed that this Magellanic Corona also exerts hydrodynamical drag on the SMC as it orbits around the LMC. With a new orbital history consistent with the present-day positions and velocities of the Clouds, the Trailing Stream ends up five times closer to us that previous models predicted.

In a subsequent study, the Magellanic Corona was directly observed using absorption line spectroscopy data from the Cosmic Origins Spectrograph on the *Hubble Space Telescope* (Krishnarao et al., 2022). From 28 sightlines extending to 35 kpc away from the LMC, they detected a radially

---

[1] While this value is near the peak of the cooling curve, the true gas temperature of the Corona varies with radius and through supernova heating, the Corona remains stable. See Figure 4.3

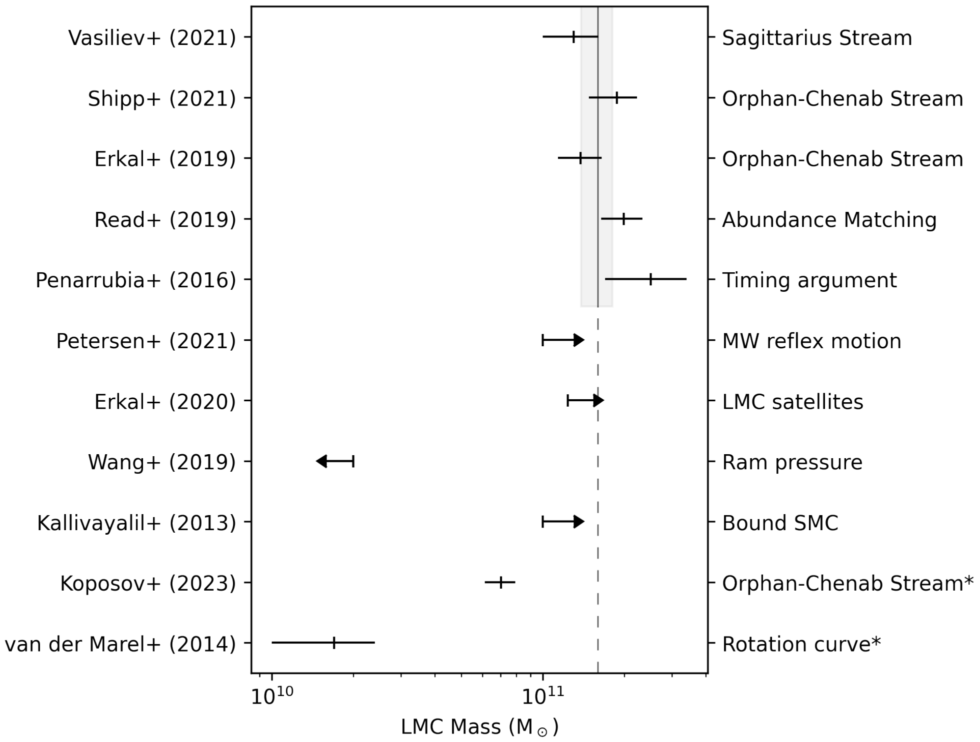

Figure 4.1: Observational LMC total mass estimates. Literature estimates for the total mass of the Large Magellanic Cloud. van der Marel and Kallivayalil (2014) and Koposov et al. (2023) (denoted with asterisks) provide constraints on the mass within 8.7 and 32.4 kpc, respectively, whereas all other estimates plotted are for the total virial LMC mass. Kallivayalil et al. (2013), Erkal and Belokurov (2020), and Petersen and Peñarrubia (2021) provide lower limits, and Wang et al. (2019) provides an upper limit. The remaining references (Peñarrubia et al., 2016; Read and Erkal, 2019; Erkal et al., 2019; Shipp et al., 2021; Vasiliev et al., 2021) give estimates of the total LMC mass with uncertainties. The error weighted average of these four values is $1.60 \pm 0.21 \times 10^{11}$ shown as the vertical line (extended to the bottom of the plot as a dashed line for comparison). The one-sigma errors are shown as a shaded region. The method for determining the LMC mass estimate from each paper is listed on the right edge of the plot.

declining profile in high ions (C IV, Si IV, O VI) with a total mass of $1.4 \pm 0.6 \times 10^9$ $M_\odot$ including a warm phase with temperature of 3×10^5 K. These results are consistent with the picture of a first-infall LMC with a Magellanic Corona. While these values give us an excellent picture of the LMC's CGM at the present-day, modeling the evolution of the Magellanic System will help us constrain the properties of the primordial LMC and its Magellanic Corona to understand dwarf galaxy evolution in general.

In this paper, we expand upon the Magellanic Corona model by presenting new, high-resolution simulations with detailed physical models including the self-consistent tracking of star formation, feedback, ionization, and metallicity to directly compare with absorption line spectroscopy observations. Furthermore, we explore the parameter space of temperatures and densities for the

Magellanic Corona and the MW's CGM that provide the best match to the observed properties of the Magellanic Clouds as well as the morphology of the neutral H I Stream. In Section 4.2, we outline the methodology of our simulations and analysis, including Sections 4.2.2 and 4.2.3 in which we explore the parameter space of temperatures and densities for the Magellanic Corona and MW CGM, respectively. In Section 4.3, we discuss the requirements to form a nearby Stream, as shown in Lucchini et al. (2021), that survives to the present day. In Section 4.4, we present an alternate simulation in which we form a Leading Arm self-consistently through tidal interactions between the Clouds. Sections 4.5 and 4.6 contain the discussion of our results and our conclusions.

4.2 Methods

We use GIZMO, a massively parallel, multiphysics code for our simulations (Hopkins, 2015; Springel, 2005). We utilize its Lagrangian "meshless finite-mass" hydrodynamics scheme which allows for the ability to track individual fluid elements while conserving angular momentum and capturing shocks (Hopkins, 2015). Star formation is included (Springel and Hernquist, 2003) with a physical density threshold of 100 cm^{-3}, a virial requirement that the gas is locally self-gravitating (Hopkins et al., 2013; Hopkins et al., 2018), and a requirement that the gas is converging ($\nabla \cdot v < 0$). Mechanical stellar feedback is also included in which we assume a constant supernova rate of 3×10^{-4} SNe Myr^{-1} $\mathrm{M}_\odot^{-1}$ for all stars less than 30 Myr old. Each supernova injects 14.8 $\mathrm{M}_\odot$ with 10^{51} ergs of energy and metals following the AGORA model (Kim et al., 2016). Cooling is included down to $\sim$ 10 K following Hopkins et al. (2018) with metal-dependent tables (Wiersma et al., 2009). We don't include radiative transfer or UV background radiation, however outside the MW at low redshift, we don't expect these mechanisms to play a significant role.

These simulations improve upon those of Lucchini et al. (2020) and Lucchini et al. (2021) by including accurate star formation and feedback with metallicity and advanced cooling routines. GIZMO calculates self-consistent ionization states for each particle based on collisional heating/ionization, recombination, free-free emission, high and low temperature metal-line cooling, and compton heating/cooling (see Appendix B in Hopkins et al., 2018) We therefore are able to track the neutral and ionized material separately throughout the simulation.

Table 4.1: Initial Properties of the Galaxies.

	LMC ($t = 0$ Gyr)	LMC ($t = 3.5$ Gyr)	SMC ($t = 0$ Gyr)
DM Mass ($M_\odot$)	1.75×10^{11}	1.75×10^{11}	7.7×10^{9}
Stellar Disk Mass ($M_\odot$)	2.5×10^{9}	2.7×10^{9}	2.5×10^{8}
Stellar Scale Length (kpc)	4.5	4.2	1.7
Gaseous Disk Mass ($M_\odot$)	0	9.1×10^{8}	1.5×10^{9}
Gaseous Scale Length (kpc)	–	5.2	6.9
CGM Mass ($M_\odot$)	5×10^{9}	3.7×10^{9}	–
CGM Temperature (K)	3×10^{5}	3.4×10^{5}	–
N Particles	5.5×10^{5}	5.5×10^{5}	8.5×10^{4}
Initial Position (kpc)	–	(33.03, 584.97, 300.80)	(−21.40, 610.74, 357.15)
Initial Velocity (km s^{-1})	–	(2.24, −63.93, −65.77)	(6.05, 10.48, −109.69)

4.2.1 Initial Conditions

Table 4.1 shows the properties of the Magellanic Clouds in our simulation and we used the DICE[2] code to generate our initial conditions (Perret et al., 2014). We used an LMC dark matter (DM) mass of 1.75×10^{11} $M_\odot$ consistent with previous studies (Besla et al., 2012; Pardy et al., 2018; Lucchini et al., 2020; Lucchini et al., 2021) and in agreement with indirect estimations (see Figure 4.1). We constrained the initial gaseous and stellar disk masses for the Magellanic Clouds by requiring their present-day values to be consistent with observations. This was straight forward for the stellar masses as the stars formed during the simulations comprise only a small fraction of the total. However the gas masses can vary greatly from their initial values due to the tidal interactions and accretion from the Magellanic Corona. We found that the LMC's disk gas mass agreed best with present-day values when allowing the gaseous disk to form naturally out of the Magellanic Corona. Therefore, we initialize our LMC ($t = 0$ Gyr in Table 4.1) with a 2.5×10^9 $M_\odot$ stellar disk and the Magellanic Corona (discussed in Section 4.2.2), and a gaseous disk forms self-consistently after 3.5 Gyr evolution in isolation. This is the LMC that we start with for the full simulations with the LMC, SMC, and MW (listed as "LMC ($t = 3.5$ Gyr)" in Table 4.1).

The only constraint on the SMC's total mass comes from its rotation curve which requires $1.25 \pm 0.25 \times 10^9$ $M_\odot$ within 4 kpc (Di Teodoro et al., 2019). While previous studies found that $\sim 10\%$ of the LMC's total mass ($\sim 2 \times 10^{10}$ $M_\odot$) produced the best results (Pardy et al., 2018), this was prior to the inclusion of the Magellanic Corona and MW CGM. Therefore, in this study we have explored the effect of the SMC total mass on the formation of the Stream and found that

---

[2] https://bitbucket.org/vperret/dice/src/master/

a lower SMC mass provides better results. This will be discussed further in Section 4.3. In our fiducial model, we used a DM mass of 7.7×10^9 $M_\odot$, a stellar mass of 2.5×10^8 $M_\odot$, and a gaseous disk mass of 1.5×10^9 $M_\odot$.

For the MW, we implemented a live DM halo with a total mass of 1.1×10^{12} $M_\odot$ combined with a hot gaseous CGM. The properties of the CGM are discussed below (Section 4.2.3).

We use a mass resolution of $\sim 3 \times 10^4$ $M_\odot$/particle for the gas elements, $\sim 2 \times 10^4$ $M_\odot$/particle for the stars, $\sim 10^6$ $M_\odot$/particle for the DM. This results in a total particle number of 1.5×10^6. Adaptive softening was used for the gas particles (such that the hydrodynamic smoothing lengths are the same as the gravitational softening length), and softening lengths of 150 pc and 550 pc were used for the stellar and dark matter particles, respectively.

4.2.2 The Magellanic Corona

To explore the parameter space of initial properties of the Magellanic Corona, we varied the initial temperature and total mass. The Corona was initialized with an isothermal distribution ($\rho \propto r^{-2}$) truncated at 200 kpc. Its total mass (within 200 kpc) ranged from 10^9 to 10^{10} $M_\odot$. This corresponds to masses of 0.6 and 6×10^9 $M_\odot$ within the LMC's virial radius of 120 kpc. The initial temperature of the Corona ranged from 10^5 to 9×10^5 K, and we used a metallicity of 0.1 solar. We explored the viability of these different Coronae by determining their stability and their impact on the present-day Stream.

As mentioned above, we intialize our LMC with a DM halo, stellar disk, and the Magellanic Corona. The gaseous disk forms during the first few billion years of evolution (in isolation). The Magellanic Corona is initialized with a streaming fraction of 0.2. Therefore, when the cooled material collapses onto the disk, it exhibits a bulk rotation as expected. Higher streaming fractions result in larger disks and lower streaming fractions result in smaller disks. This is because without any rotation, more material falls into the center of the gravitational potential and high gas densities induce very strong star formation which blows out the remaining gas. With too much rotation, the infalling cool material spreads out to larger radii (because it has higher velocity) and the densities are not high enough for star formation.

Stability

The main factor in determining the viable parameter space for the temperature and density of the Magellanic Corona is in its stability around the LMC. If the temperature is too high, the Coronal material blows off because its internal energy is too high and much of the material is unbound to begin with. If the temperature is too low, too much gas falls onto the LMC disk leading to disk gas fractions that are too high as well as very high star formation rates inconsistent with the LMC's history. Similarly, if the Corona starts with too much mass (i.e. too high density), the disk becomes too gas rich in contrast to the present day observed gas masses. Below a mass cutoff, the Corona remains stable however in order to reproduce the high ionization fractions along the length of the Stream, the Magellanic Corona must be more massive than 10^9 $M_\odot$ (within 120 kpc; see Section 4.2.2).

Figure 4.2 shows these results. The nine panels depict nine different simulations with varying initial conditions in which the LMC and Magellanic Corona were evolved in isolation. The initial temperature of the Corona increases from left to right (with values of 1, 3, and 9×10^5 K), while the initial mass of the Corona increases from top to bottom (1, 5, and 10×10^9 $M_\odot$ within 200 kpc). The black lines show the total masses of the gaseous components within 120 kpc (the virial radius of the LMC) – total gas mass (solid), ionized mass (circumgalactic Coronal gas; dashed), and neutral disk mass (dotted).

Figure 4.3 also shows the temperature distribution as a function of radius for the nine simulations at $t = 4$ Gyr. Again initial temperature increases to the right and the initial gas mass increases downwards. The mean temperature of the gas within $20 < r < 250$ kpc is shown as a horizontal dashed line. Interestingly, these white lines don't vary dramatically between the three columns. This means that the initial temperature has a minimal, if any effect on the stable temperature of the Corona.

We do, however, see that increasing the initial mass of the Corona affects the spread in temperatures. We believe this is due to the fact that the Coronae with higher initial masses contain higher density gas which can cool more effectively. Cooling is very efficient around 10^5 K, so subtle changes in density and temperature can have a strong impact on the strength of cooling. These higher density Coronae thus don't have sufficient supernova energy injection to keep the gas warm.

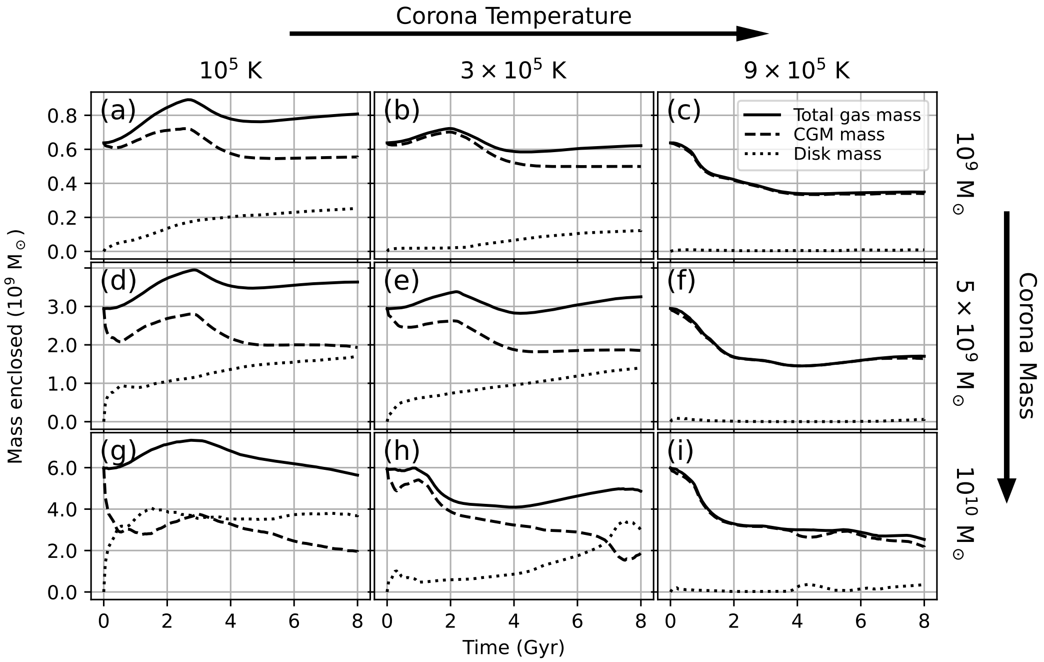

Figure 4.2: Magellanic Corona stability. Study of the stability of the Magellanic Corona for varying initial masses and temperatures. Each panel shows the total, CGM, and disk masses within 120 kpc as a function of time (solid, dashed, and dotted lines, respectively). The initial temperatures increase from left to right with values of 1, 3, and 9×10^5 K. The initial masses increase from top to bottom with values of 1, 5, and 10×10^9 M$_\odot$ (within 200 kpc). Our fiducial model (see Section 4.2.2) is the center frame (Panel e) corresponding to an initial mass of 3×10^9 M$_\odot$ and a temperature of 3×10^5 K.

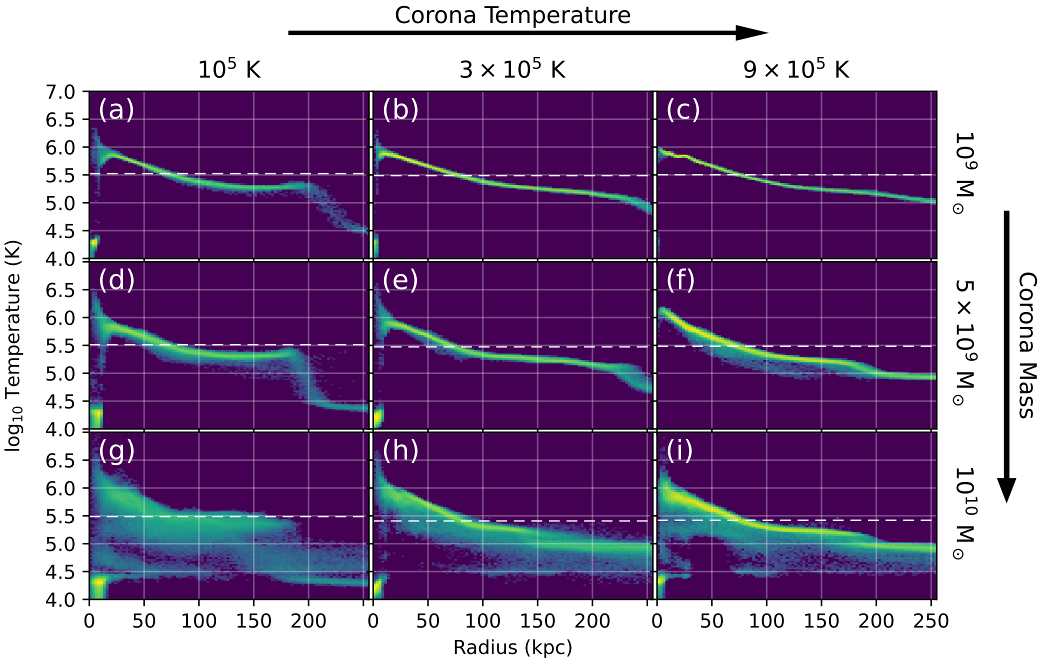

Figure 4.3: Magellanic Corona temperature. Temperature profile of the Magellanic Corona for nine initial masses and temperatures (as in Figure 4.2). These histograms show the relative density of the gas temperature as a function of radius for the nine simulations at $t = 4$ Gyr. The horizontal white dashed lines show the mean temperature of the gas within $20 < r < 250$ kpc.

Effect on the Magellanic Stream

We now want to explore the effect of varying the Magellanic Corona's initial mass and temperature on the properties of the present-day Magellanic System. The initial total mass of the Corona directly affects the amount of ionized gas that we observe around the Stream today. Via absorption-line spectroscopy, Fox et al. (2014) estimated that there is $\sim 1.5 \times 10^9$ $M_\odot$ of ionized gas associated with the Magellanic System, $\sim 10^9$ $M_\odot$ of which is in the Trailing Stream region. Figure 4.4 shows the total mass in the Trailing Stream for various different models. These values were calculated by mimicking the observational technique of integrating the column density at an assumed distance of 55 kpc. These are not the physical masses in the system (see Section 4.3.2), but allow us to compare directly with the observational estimates shown in the left-most bar (Brüns et al., 2005; Fox et al., 2014). Continuing from left to right we have the results from the simulations published in Besla et al. (2012) and Pardy et al. (2018) in which no ionized material was produced. The three right-most bars show the results of our simulations for three different initial Corona masses, 1, 5, and 10×10^9 $M_\odot$ (corresponding to Panels b, e, and h in Figures 4.2 and 4.3). Clearly, as we increase the progenitor mass, we are able to produce more ionized material in the Stream. For masses below 5×10^9 $M_\odot$ we are unable to reproduce the observations. In the models that we tested, either 5×10^9 or 10^{10} $M_\odot$ result in viable models. For masses larger than 10^{10} $M_\odot$, the mass of the LMC's CGM begins to approach estimates of the MW CGM's mass. Given the significant difference in virial masses of the two galaxies, having similar CGM masses is unlikely. Therefore Magellanic Corona masses below 10^{10} $M_\odot$ are preferred.

We also explored the impact of the initial Magellanic Corona temperature on the present-day Magellanic System. As shown in Figure 4.3, the initial temperature doesn't have a large effect on the temperature distribution or on the mean Corona temperature after 4 Gyr of evolution. The main difference that we see between temperature models is in the properties of the LMC disk. Since we form our LMC disk self-consistently by letting it condense out of the Corona, the temperature plays a large role in its size and stability. Figure 4.5 shows the LMC's disk at the present day for three different simulations compared with observational data from the HI4PI survey (HI4PI Collaboration et al., 2016; Westmeier, 2018). Panels a, b, and c show the results from simulations with initial Magellanic Corona Masses of 1, 3, and 9×10^5 K, respectively. Lower initial Corona

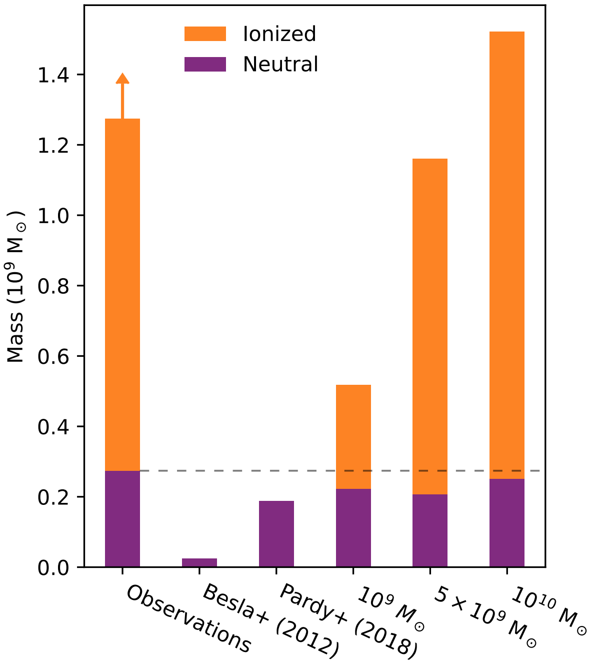

Figure 4.4: The source of mass in the Trailing Stream. Each bar shows the results for a different model compared against the observed mass in neutral and ionized gas shown in the left-most column (2.7×10^8 M$_\odot$ in neutral gas, Brüns et al. 2005; 1.0×10^9 M$_\odot$ in ionized gas, though this may be an underestimate Fox et al. 2014). Each value is computed by integrating the column densities for all gas behind the SMC ($l_{\rm MS} < l_{\rm MS,SMC}$) assuming a distance to the gas of 55 kpc (as done in observational works, Brüns et al. 2005, Fox et al. 2014). The total neutral masses in Besla et al. (2012), and Pardy et al. (2018) are 2.5×10^7 M$_\odot$ and 1.9×10^8 M$_\odot$, respectively. The three right-most columns show the results from our new simulations with initial Magellanic Corona masses of 1, 5, and 10×10^9 M$_\odot$ (at a temperature of 3×10^5 K; Panels b, e, and h in Figures 4.2 and 4.3). The neutral material is relatively consistent between these models at 2.2, 2.1, and 2.5×10^8 M$_\odot$, while the ionized gas masses are 3.0×10^8, 9.5×10^8, and 1.3×10^9 M$_\odot$ for the low, medium, and high mass models, respectively. By dividing the ionized mass by the total mass, we can get an approximate value for the average ionization fraction in the Magellanic Trailing Stream, and we find values of 57%, 82%, and 84% for the three models (compared with $\sim 75\%$ in the observed case).

temperatures leads to larger LMC disks due to more material cooling and losing angular momentum. For the highest temperatures (Panel c), no LMC disk forms since the Corona material can't cool and fall to the center of the gravitational potential. This is also visible in Figure 4.2f in which the dotted line (showing the total disk mass) remains at zero throughout the simulation.

Fiducial Model

Based on these tests, our chosen fiducial Magellanic Corona was initialized with a total mass (within 200 kpc) of 5×10^9 M$_\odot$ following an isothermal profile at a temperature of 3×10^5 K and a metallicity of 0.1 solar. After 3.5 Gyr in isolation, there remains 3.7×10^9 M$_\odot$ of ionized material bound to

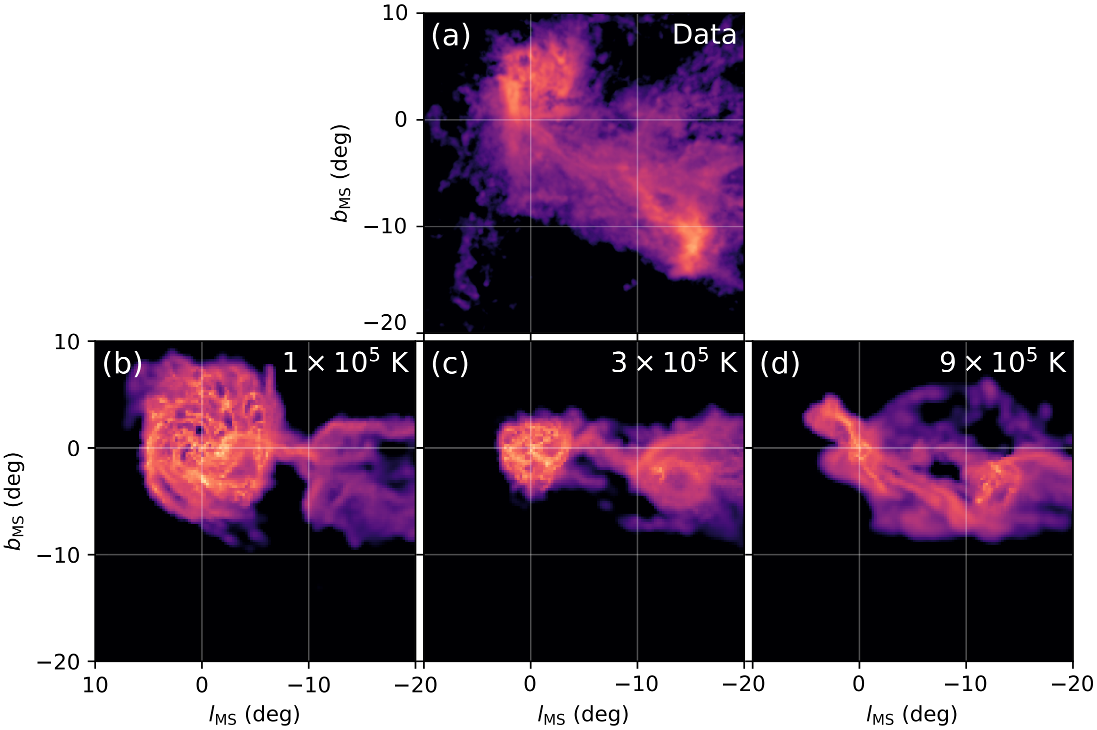

Figure 4.5: Present-day LMC disk for different Corona temperatures. A zoomed in region around the Magellanic Clouds is shown in Magellanic Coordinates for the observational data (Panel a; HI4PI, Westmeier 2018) compared with three different simulations (bottom panels). Panels b, c, and d show the results from initial Magellanic Corona temperatures of 1, 3, and 9 × 10^5 K, respectively (with a total mass of 5×10^9 $M_\odot$; Panels d, e, and f in Figures 4.2 and 4.3). As the temperature decreases the size of the LMC disk increases due to Corona material collapsing onto the disk. At higher temperatures (Panel d), barely any LMC disk forms.

the LMC (with 2×10^9 $M_\odot$ within 120 kpc) and its temperature profile is shown in Figure 4.6b with a median value of 3.4×10^5 K. 9.1×10^8 $M_\odot$ has cooled to form the LMC's gaseous disk.

4.2.3 The Milky Way's CGM

We initialized the MW CGM with a β-profile following Salem et al. (2015):

$$\rho \propto \left[1 + \left(\frac{r}{r_c}\right)^2\right]^{-3\beta/2} \tag{4.1}$$

with $r_c = 0.35$ and $\beta = 0.559$. We varied the total mass from 10^{10} to 8×10^{10} $M_\odot$, varied the temperature from 4×10^5 to 3×10^6 K, and tested with and without uniform rotation of the CGM. As we found above with the Magellanic Corona, changing the initial temperature of the gas did not affect the equilibrium temperature distribution significantly. Similarly, rotation, while it did

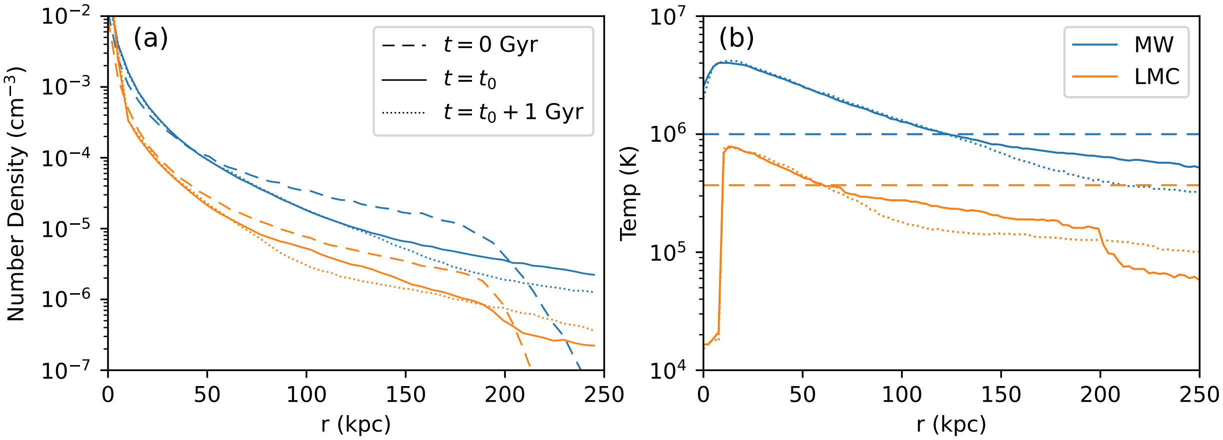

Figure 4.6: Initial properties of the Magellanic Corona and MW CGM. The Magellanic Corona is shown in orange and the MW CGM is shown in blue. The dashed lines shows the profiles at $t = 0$ Gyr, and the solid lines show the profiles at the end of isolated evolution ($t_0 = 2$ Gyr for the MW, and $t_0 = 3.5$ Gyr for the LMC). The dotted lines show the profiles after an additional 1 Gyr of evolution. Panel (a) shows the number density and panel (b) shows the median temperature as functions of radius.

decrease the equilibrium temperature of the CGM slightly, did not have a substantial effect on the Magellanic System. Therefore, the main variable we explored was the total mass.

Lucchini et al. (2021) found that a MW CGM mass of 4×10^{10} $M_\odot$ was required to get the best match to the velocity gradient along the Stream (two times larger than Salem et al. 2015). In the suite of orbits tested in this paper, we found that the largest effect that the MW CGM had on the present-day Stream is on the morphology of the neutral and ionized components. Figure 4.7 shows the ionized (orange) and neutral (grayscale contours) components of the simulated Streams in Magellanic Coordinates for three different models. The total mass of the MW CGM increases from top to bottom with values of 1, 2, and 8×10^{10} $M_\odot$. The higher gas density induces stronger ram pressure on the Magellanic gas, decreasing the on-sky extent of the ionized gas, and making the neutral Stream longer and narrower. We find that a value of 2×10^{10} $M_\odot$ (Panel b; in agreement with estimates from Salem et al. (2015)) provides the best agreement with the observations.

Our fiducial MW CGM model therefore has a total mass of 2×10^{10} $M_\odot$ at 10^6 K and is nonrotating. After evolution in isolation for 2 Gyr, 1.9×10^{10} $M_\odot$ remains bound with a mean temperature of 1.4×10^6 K. Figure 4.6 shows the initial and final (after 2 Gyr in isolation) density and temperature profiles in orange.

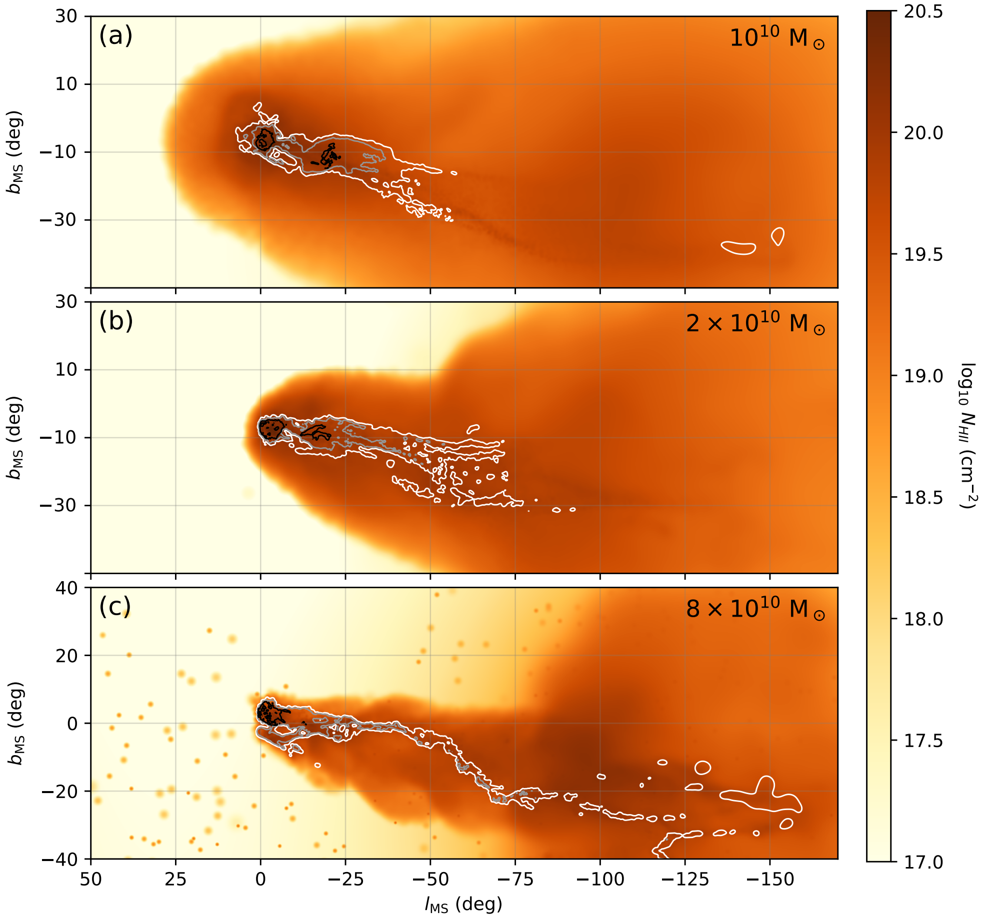

Figure 4.7: The Effect of the MW CGM on the Present-Day Stream. The ionized (orange) and neutral (grayscale contours) Magellanic gas for three simulations shown as they would appear on the sky in Magellanic Coordinates. Panels a, b, and c, show the results of simulations with a MW CGM total mass of 1, 2, and 8×10^{10} M$_\odot$, respectively (listed in the top right of each panel). All panels use our fiducial LMC with a Magellanic Corona of 5×10^9 M$_\odot$ at 3×10^5 K. The neutral gas contours (white, grey, and black) are at values of $\log_{10}(N_{\rm HI}) = 19$, 20, and 21, respectively.

4.2.4 Orbits of the Clouds

Following Lucchini et al. (2021), we have determined viable orbital histories for the Clouds with analytic integration. Using the galactic dynamics code gala[3] (Price-Whelan, 2017; Price-Whelan et al., 2022), we varied the present-day positions and velocities of the Clouds within their errors (Di Teodoro et al., 2019; Graczyk et al., 2020; De Leo et al., 2020; Wan et al., 2020) and integrated them backwards in time considering the effects of the MW, dynamical friction, and an empirical hydrodynamical friction term. With slight alterations to the initial positions and velocities, we

---

[3] `https://gala.adrian.pw/`

obtained the initial conditions for our full hydrodynamic simulations using GIZMO. Our fiducial orbit used in the simulations presented here consists of two interactions over 4.2 Gyr, very similar to the orbits presented in Lucchini et al. (2021). The initial properties of the Clouds as well as their positions and velocities (relative to the MW located at the origin) are listed in Table 4.1.

4.3 A Nearby Stream

As shown in Lucchini et al. (2021), the inclusion of the Magellanic Corona leads to a family of orbital histories in which the Stream ends up within 50 kpc from the Sun. The previous first-infall history predicted the Trailing Stream at $>$ 100 kpc (Besla et al., 2012), however the hydrodynamical friction on the SMC as it orbits the LMC requires fewer interactions and a shorter interaction history. As the stripped material moves through the Magellanic Corona and approaches the MW's CGM, it is encountering hot gas. In order for the neutral Stream to survive to the present day, the gas stripped out of the SMC must be dense enough to remain neutral.

As we have seen above (Sections 4.2.2 and 4.2.3) the properties of the MW CGM and the Magellanic Corona are largely determined by their stability. We therefore varied the properties of the Clouds themselves to ensure that the neutral Stream survives to the present day. By reducing the DM mass of the SMC, this reduces the potential well of the galaxy allowing for more material to be tidally stripped during its interactions with the LMC. For SMC DM masses below 10^{10} $M_{\odot}$, we find that there is enough gas stripped such that the neutral Stream survives its passage through the Magellanic Corona and MW CGM.

Figure 4.8 shows the results of our fiducial simulation in Magellanic Coordinates (defined in Nidever et al. 2008). The observational data is shown in Panel (a) with the H I 21cm emission from Nidever et al. (2010) in blue with C IV absorption detections shown as points colored by column density (the squares denote upper limits). Panels (b) and (c) show, respectively, the C IV and H I emission in our simulation. Panel (e) also shows the ionized material through H II emission. While the C IV doesn't trace the H II very well, we believe this is due to temperature variations throughout the Stream. Looking at the H II, we can see that the ionized material forms a cocoon around the neutral material covering a significant fraction of the sky. The neutral material consists of two filaments with turbulent, non-uniform structure, agreeing well with the morphology of the

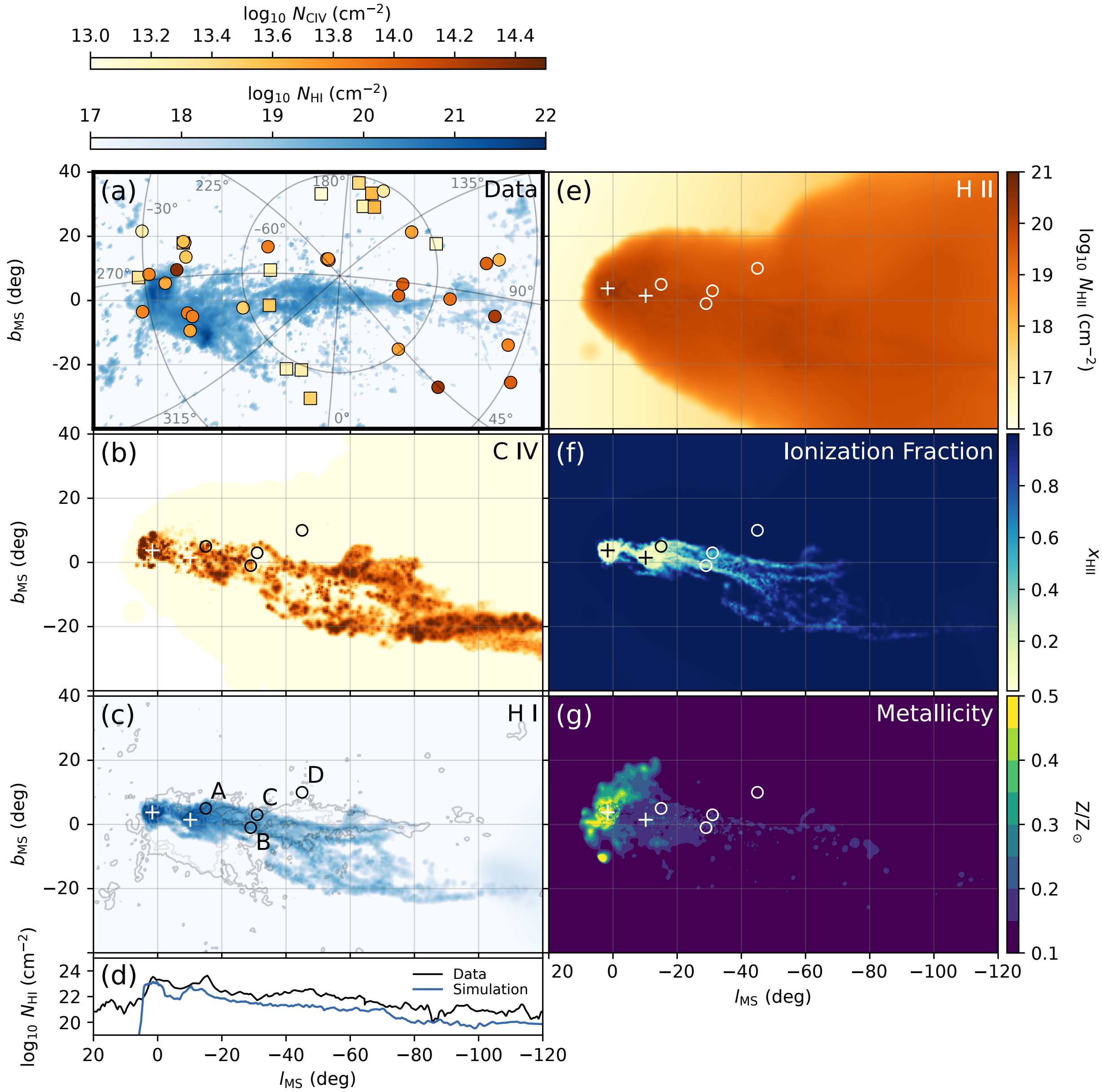

Figure 4.8: Properties of the nearby Stream. The properties of our simulated Stream compared with observations. Panel a shows the observed neutral 21 cm H I column density in blue from Nidever et al. (2010) and the C IV column densities detected via absorption-line spectroscopy as points colored in orange (the squares denote upper limits; Fox et al. 2014). Panels b, c, e, f, and g show the C IV column density, H I column density, H II column density, ionization fraction ($x_{\rm HII} = {\rm N(H\,II)}/({\rm N(H\,I)} + {\rm N(H\,II)})$), and metallicity, respectively. The plus marks in these panels denote the locations of the LMC and SMC at the present day, and the circles show the locations of four sightlines used to quantitatively compare our simulations with HST/COS data via simulated absorption-line spectroscopy (see Table 4.2). Panel d shows the integrated column density as a function of Magellanic Longitude with the observations in black and the simulation shown in blue.

Table 4.2: Mock Absorption-Line Spectroscopy Results.

	A	B	C	D
log N(H I)	19.91	19.88	19.11	15.27
log N(H II)	19.68	19.70	19.62	19.56
log N(Si II)	16.31	16.25	15.41	2.43
log N(Si III)	15.41	15.32	14.81	7.71
log N(C II)	16.78	16.72	15.88	5.84
log N(C IV)	13.66	13.99	12.83	12.08
log N(O I)	16.65	16.65	15.47	–
log N(O VI)	15.07	14.86	14.54	14.02
$x_{\rm HII}$ [a]	0.37	0.40	0.76	1.0
Z	0.172	0.160	0.133	0.100

Notes. [a] $x_{\rm HII}$ = N(H II)/(N(H I) + N(H II))

observations. No Leading Arm is formed, however this is due to the specific orbital history chosen here, see Section 4.4 for further discussion. Panel (d) shows the column density integrated along Magellanic Latitude as a function of Magellanic Longitude. The observations are shown in black and the simulation in blue. While we slightly underpredict the total column, the decreasing density as a function of longitude agrees well.

Panels (f) and (g) show the ionization fraction and the metallicity along the Stream, respectively. The ionization fraction varies from values of 0.05 in the Clouds and ∼0.3 in the Stream to ∼1.0 off of the neutral material (e.g. position D). By dividing the ionized gas mass by the total mass in the Stream, we can obtain an approximate average ionization fraction of 82% (compared with ∼ 75% in the observations). The metallicity varies slightly between the Clouds, the neutral Stream, and the ionized Corona. With values ranging from $Z_\odot$ to ∼ 0.1 $Z_\odot$. These properties are discussed further below.

4.3.1 Mock Spectroscopy

We have denoted four sightlines in our simulation data to analyze in absorption. For this, we used the Trident[4] python package built upon yt[5] (Hummels et al., 2017; Turk et al., 2011). Position A lies very near the Clouds, positions B and C lie on two different filaments in the neutral Stream,

---

[4] `https://trident.readthedocs.io/en/stable/`

[5] `https://yt-project.org`

and position D lies off the neutral Stream within the ionized Corona. These four locations will give us a representative look at the spectral differences across our simulated Stream. For each sightline, we have "observed" H I, H II, Si II, Si III, C II, C IV, O I, and O VI. The integrated column densities and some derived values are shown in Table 4.2.

Across these four sightlines, we see column densities in broad agreement with the observations. The H II integrated densities in particular agree very well with the values calculated from Cloudy modeling (19.42 - 20.04; Fox et al. 2014). We also find excellent agreement with the range of ionization fractions detected. At position A, we see a relatively low ionization fraction of $x_{\mathrm{HII}} = 0.37$ due to the high H I column density near the SMC. In the Trailing Stream region (positions B, C, and D), we find increasing x_{HII} with decreasing H I column density up to $x_{\mathrm{HII}} = 1.0$ in agreement with the range of values seen in the data (Fox et al., 2014).

The metallicity distribution throughout the Magellanic System is also very interesting (Figure 4.8f). We see high values in the LMC, with lower values in the SMC, as expected based on their star formation histories. The gas metallicity also decreases along the Stream as we move further from the Clouds. While we don't see values as high as those observed towards Fairall 9 (Richter et al., 2013), we do see most of the Stream around 0.1 solar with a few locations up to ~0.2 solar.

4.3.2 Trailing Stream Mass

As discussed in Lucchini et al. (2021), a nearby Stream would impact the total mass of both its neutral and ionized components. Observations calculate the total mass by integrating the column densities assuming a distance to the gas. Brüns et al. (2005) found that there was $4.7 \times 10^8 \times [d/(55\ \mathrm{kpc})]^2\ \mathrm{M}_\odot$ of neutral material in the Magellanic System outside the LMC and SMC, and Fox et al. (2014) estimated $\sim 1.5 \times 10^9 \times [d/(55\ \mathrm{kpc})]^2\ \mathrm{M}_\odot$ in ionized material. These calculations assume all the material is at a single distance. While this is not physically accurate, it is the best we can do since we do not know the distance to the gas in the Stream. In order to accurately compare with these observations, we performed the same analysis on our simulated data. By integrating the column density assuming a distance of 55 kpc, we find that there is $5.4 \times 10^8\ \mathrm{M}_\odot$ of neutral gas and $1.2 \times 10^9\ \mathrm{M}_\odot$ of ionized gas in the Bridge and Trailing Stream.

We can also calculate the physical gas mass in the simulation. First we locate the Clouds in the simulation and exclude the gas within spheres of radii 1.65 kpc and 6.07 kpc around the SMC and LMC, respectively. These sizes are calculated from the angular size of the disks (excluded in the mock observation calculation described above) and the distances to the Clouds in the simulation. Then we simply sum up the mass of all the particles remaining weighted by their ionization fraction. This leaves 6.5×10^8 $M_\odot$ of neutral material and 4.3×10^9 $M_\odot$ of ionized material. So, despite having a mean distance of 47 kpc to the neutral Stream, the total mass is actually larger than the value assuming all the gas is located at 55 kpc. The mean distance to the ionized material is 142 kpc which means that the physical mass of the hot gas is much larger than the observations indicate.

4.4 The Leading Arm

The Leading Arm is comprised of four main complexes each containing multiple small, turbulent clouds. These complexes are labelled LA I-IV and have velocities ranging from ∼100 to ∼300 km s^{-1} with a total mass of $3.0 \times 10^7 [d/(55\ \text{kpc})]^2$ $M_\odot$ (Brüns et al., 2005; Nidever et al., 2010). The true nature of the Leading Arm is still very much unknown. It was originally proposed as Magellanic material due to the velocity of the H I (Putman et al., 1998), and subsequent metallicity measurements were not inconsistent with an SMC origin (Richter et al., 2018; Fox et al., 2018). But the properties of the Leading Arm are very different than those of the Trailing Stream (Fox et al., 2020) and models have found mixed results in explaining it self-consistently. Tidal models have generally been able to produce gas leading the Clouds (Besla et al., 2012; Pardy et al., 2018), however the effect of the MW CGM on the ability for the leading gas to survive has been debated (Tepper-García et al., 2019; Bustard and Gronke, 2022). Additionally, the shorter interaction history shown in Lucchini et al. (2021) didn't allow enough time for material to be thrown ahead of the Clouds in to the Leading Arm region. Here we show new orbital orientations in which this is no longer a problem.

Classically, there are two tails formed during tidal interactions – a bridge between the galaxies, and a tail of escaping debris (Toomre and Toomre, 1972). In our previous models of Stream formation, we do see both of these features formed, however the material stripped out of the SMC into the original tidal bridge[6] becomes absorbed by the LMC, while the escaping debris forms the Trailing Stream (Lucchini et al., 2021). In the simulations presented here, we have explored alternative orbits in which the tidal bridge material orbits the LMC at larger radii. Therefore, at the present-day, the original tidal bridge forms the Trailing Stream (since it has become unbound from the LMC), while the escaping material is thrown ahead of the Clouds in their orbits to form the Leading Arm.

In this family of orbital histories, the SMC remains at a relatively large distance from the LMC ($\sim$50 kpc) until about 1 Gyr ago when the separation between the Clouds decreases until their direct collision which forms the Magellanic Bridge. This larger pericentric distance allows for the stripped material to also remain well outside the LMC's disk. This is in contrast to closer approaches (as seen in our previous models, Lucchini et al. 2021) for which the tidal bridge material gets absorbed into the LMC disk.

Figure 4.9 shows the present-day appearance of this simulated Leading Arm (Panel b) compared with observations (Panel a; Nidever et al. 2010), as well snapshots from the orbital history of the Clouds for this particular simulation (Panel d). The Leading Arm clouds have very similar elongated, turbulent morphologies to the observed structures. And the integrated column density (Panel c) also reproduces the data very well. While the Trailing Stream for this particular simulation is slightly offset and too short with respect to the observations, its filamentary morphology also mimics the data well. It is plausible that a Magellanic orbital history exists such that the Leading Arm can be formed in this way while also reproducing the large-scale structure of the Trailing Stream.

4.4.1 The MW CGM's Effect on the Leading Arm

Previous works have shown that the density of the MW's CGM has a strong effect on the survivability of the Leading Arm (LA; Tepper-García et al. 2019; Lucchini et al. 2020). We have also explored this in the context of these new orbits. Figure 4.10 shows the observational data (Panel a) compared with three simulations (bottom panels). Panels b, c, and d included MW CGM total masses of 1, 2, and 8×10^{10} $M_\odot$. The model in Figure 4.9 corresponds to Panel c.

---

[6] Note that this bridge material is distinct from the present-day Magellanic Bridge which was formed through the direct collision of the Clouds a few hundred million years ago.

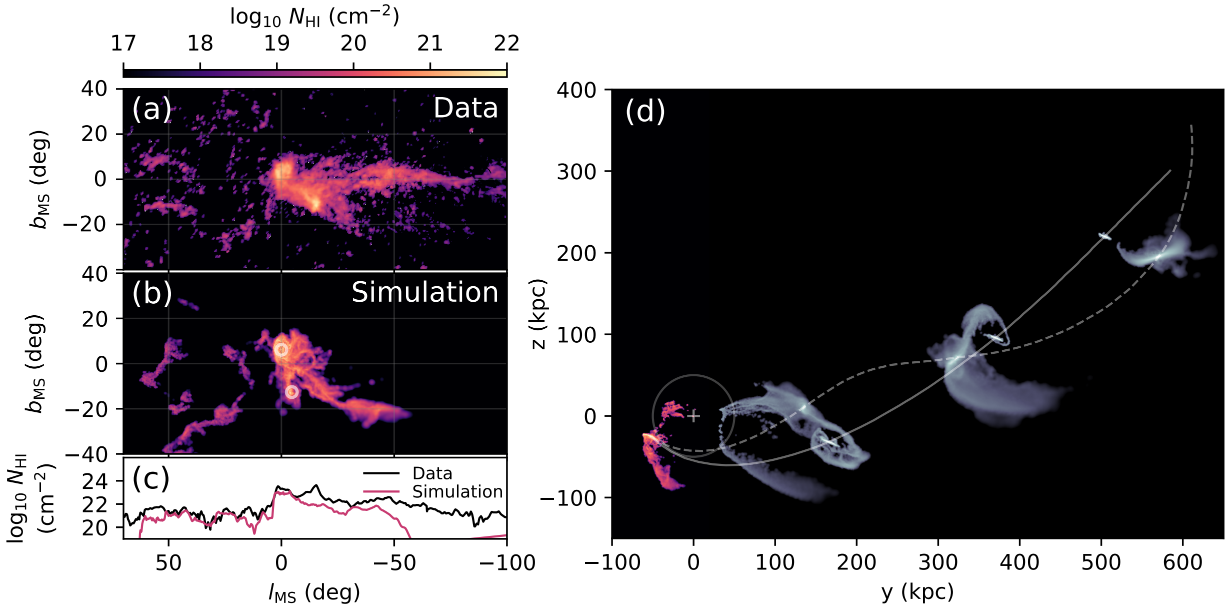

Figure 4.9: Formation of the Leading Arm. Panels a and b show the column densities of the observed (Panel a; Nidever et al. 2010) and simulated (Panel b) Stream in Magellanic Coordinates. Panel c shows the integrated column density as a function of Magellanic Longitude with the observed data shown in black and the simulation results shown in purple. While the Trailing Stream is slightly offset and too short, the Leading Arm provides excellent agreement with the data in terms of its column density and overall morphology. Panel d shows an orbital history for the Clouds that produces a Leading Arm. This panel is in Cartesian coordinates with the MW located at the origin (denoted by a plus symbol) and a Galactocentric radius of 50 kpc is shown by a grey circle. The orbits of the LMC and SMC shown as solid and dashed lines, respectively. The projected neutral gas density of the Magellanic material is shown at four times: the present day (in color), 800 Myr ago, 2.25 Gyr ago, and 3.85 Gyr ago. You can see that the Trailing Stream originates from the tidal bridge material while the Leading Arm comes from the tidal tail.

In previous works it has been found that increasing the MW CGM mass and density prevents the LA from forming due to increased ram pressure forces. However in the simulation presented here, there is enough high-density material thrown out in to the leading region that much higher MW CGM masses are allowed. For example, in Lucchini et al. (2020), we found that a total MW CGM mass of 5×10^9 M$_\odot$ was sufficient to prevent the formation of the LA. Whereas in Figure 4.10, we are testing values of 1, 2, and 8×10^{10} M$_\odot$, much more consistent with observational estimates.

Furthermore, the high densities of the stripped gas result in a clumpy, discrete morphology upon interaction with the gaseous external medium. If the leading material is too diffuse, increasing the MW CGM mass and density simply prevents it from reaching the LA region. With this high-density stripped material, an increase in the MW CGM mass causes the gas to fragment (comparing Figure 4.10b and c). This discrete nature agrees with the morphology of the observed LA very well.

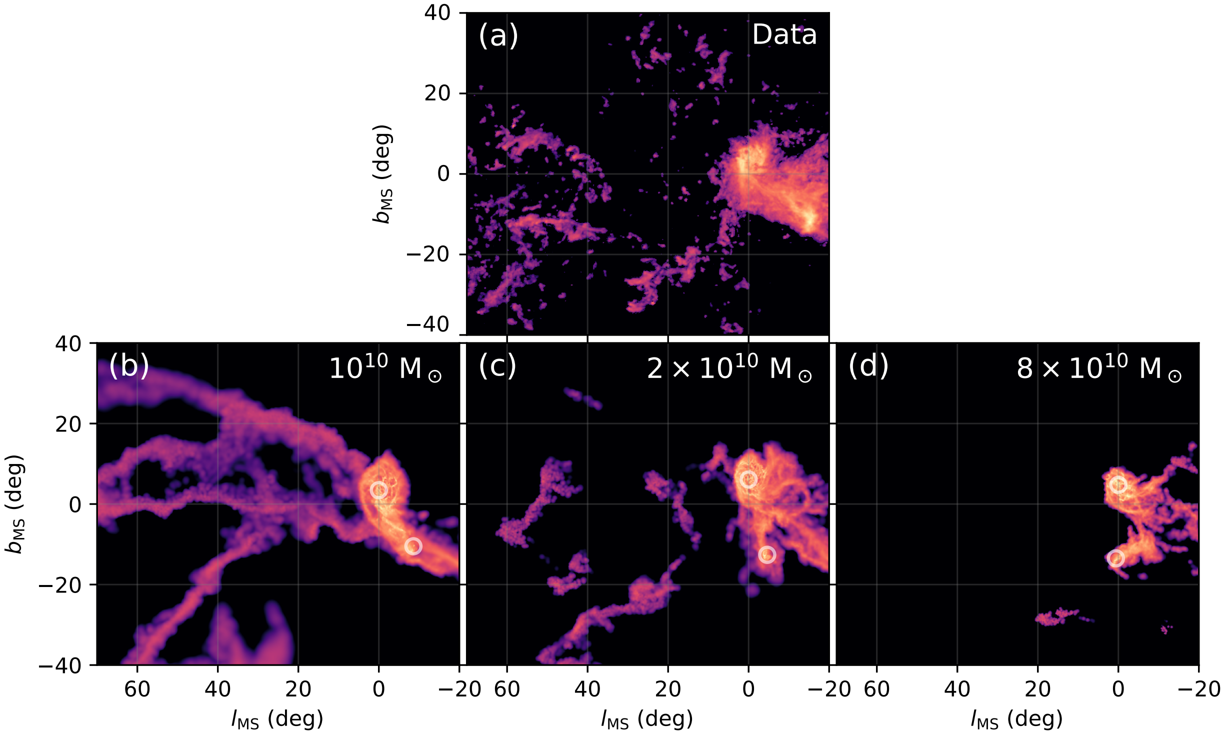

Figure 4.10: The effect of the MW CGM mass on the Leading Arm. The morphology of the Leading Arm for three different MW CGM masses compared with the data. Panel a shows the Leading region of the HI4PI neutral H I observations in Magellanic Coordinates (Westmeier, 2018). Panels b, c, and d show the results of simulations with MW CGM masses of 1, 2, and 8 × 10^{10} M$_\odot$, respectively (listed in the top right of each panel). All panels use our fiducial LMC with a Magellanic Corona of 5×10^9 M$_\odot$ at 3×10^5 K.

We do find that increasing the MW CGM mass even further (Panel d) results in the prevention of LA formation due to increased ram pressure forces.

The best agreement with the observations is found with a MW CGM mass of 2×10^{10} M$_\odot$. It is worthwhile to note that this MW CGM mass constraint agrees perfectly with the constraint found when looking at the neutral Stream length and ionized gas extent (Figure 4.7). This is also in line with the total CGM mass predicted in Salem et al. (2015).

4.5 Discussion

The model presented here is a continuation of the tidal, first-infall model originally presented in Besla et al. (2010) and Besla et al. (2012). These models formed the Trailing Stream and Leading Arm through 4 interactions over 7 Gyr, however they didn't include any MW CGM. In response to the observations of the large ionized mass in the Stream (Fox et al., 2014), Pardy et al. (2018) attemped to increase the stripped material in the Magellanic System by increasing in the pre-infall LMC and SMC gaseous disk masses. While this brought the present-day neutral Stream mass closer to the observed values (see Figure 4.4), it wasn't enough to account for the total mass of $> 10^9$ $M_\odot$. Our model now includes the Magellanic Corona which provides the remaining mass (in the form of warm ionized gas) bringing the results of our simulations in agreement with the observations (Lucchini et al., 2020).

While these models represent a significant step forward in terms of gas physics, there are a few caveats as well. As mentioned above, in order to reproduce the observed ionization fractions, we reduced the SMC's total mass to 7.7×10^9 $M_\odot$. A full exploration of the possible orbital histories of the Clouds with this new SMC mass should be performed to ensure that models can reproduce the present-day positions and velocities of the Clouds accurately. Additionally, an in-depth discussion of the properties of the LMC and SMC disks and the Magellanic Bridge is beyond the scope of this paper, however these features provide concrete observational signatures that can discriminate between models.

Additionally, no radiative transfer or UV background radiation is included in these simulations. While they are not expected to play a large role in the low-redshift universe, their inclusion could affect the observed ionization fractions. A full exploration of their impacts will be explored in future work.

The other proposed formation pathway for the Magellanic Stream involves ram-pressure stripping gas out of the LMC and SMC disks (Hammer et al., 2015; Wang et al., 2019). While this model is able to account for many of the features of the Magellanic System, including its turbulent morphology and ionized gas component, it requires a very low mass for the LMC ($< 2 \times 10^{10}$ $M_\odot$) with little to no dark matter. This is in contrast with the many indirect indications of the LMC's mass shown in Figure 4.1. Moreover, they use relatively low mass models of the MW while including a very extended, high-mass CGM (total masses of $\sim$7 and 8×10^{11} $M_\odot$ with CGM masses of 2 and 1.5×10^{11} $M_\odot$, i.e. 28% and 18%, respectively). These gaseous halos extend out beyond 500 kpc and we have not been able to reproduce the stability reported in Figure 1 of Wang et al. (2019). Finally, they do not discuss the metallicity along the length of the Stream which may not agree with observations given that there is significant LMC material stripped.

By obtaining constraints on the distance to the gas in the Stream through absorption-line spectroscopy towards MW halo stars, we will be able to better discriminate between existing models. Moreover, a reevaluation of the properties of the Leading Arm could lead to answers on whether it is of Magellanic origin or not. These observations and more will constrain key properties of the Magellanic System, giving us the information we need to converge on the true history of the Magellanic Clouds.

4.6 Conclusions

We have fully characterized the influence of the Magellanic Corona on the formation and evolution of the Magellanic Stream. With this suite of simulations, we have shown that the first-infall tidal model of Stream formation can produce a present-day Magellanic System with properties in agreement with the observations (Figure 4.8). The ionized component is formed out of the Magellanic Corona, which becomes warped and shaped around the Clouds and the neutral Stream through its interactions with the MW's CGM. The trailing Stream's turbulent morphology seen in H I is reproduced through interactions between the neutral gas and the warm/hot gas in the Magellanic Corona and MW CGM. We find a range of ionization fractions and metallicities in agreement with absorption-line spectroscopy observations. Moreover, we find an orbital model in which the Leading Arm is formed through tidal interactions while including the Magellanic Corona and MW CGM (Figure 4.9). This Leading gas matches the distribution and morphology of the 21-cm observations very well, however this specific model does not reproduce the trailing Stream as well as some of our other models.

We have also explored the parameter space of temperatures and densities for the Magellanic Corona to constrain its properties. We find that a mass $> 5 \times 10^9$ $M_\odot$ (within 200 kpc) can provide sufficient ionized material at the present day (Figure 4.4). By forming the LMC's gaseous disk self-consistently out of the Corona, we are able to reproduce the gas mass within the galaxy's disk at the present day. The initial temperature of the Coronal gas determines the size and mass of the LMC's disk at later times, so we found that a value of 3×10^5 K (in agreement with the virial temperature) provides the best results (Figure 4.5).

These models show that we are able to reproduce the properties of observed Magellanic System while accounting for a large LMC mass. The Magellanic Corona provides the key element that necessitates a review of the precise orbital histories of the Clouds. This brings the Trailing Stream gas much closer to us than previously thought, explaining the turbulent morphology and H α brightness, and implying an infall onto the MW disk within ∼100 Myr. These models also show the possibility of self-consistently forming the Leading Arm through tidal interactions between the Clouds.

References

Besla, G., et al. 2010, *ApJ*, 721, L97–L101, `10.1088/2041-8205/721/2/L97`.

Besla, G., et al. 2007, *ApJ*, 668, 949–967, `10.1086/521385`.

Besla, G., et al. 2012, *MNRAS*, 421, 2109–2138, `10.1111/j.1365-2966.2012.20466.x`.

Brüns, C., et al. 2005, *A&A*, 432, 45–67, `10.1051/0004-6361:20040321`.

Bustard, C. and Gronke, M. 2022, *ApJ*, 933, 120, `10.3847/1538-4357/ac752b`.

Connors, T. W., Kawata, D., and Gibson, B. K. 2006, *MNRAS*, 371, 108–120, `10.1111/j.1365-2966.2006.10659.x`.

D'Onghia, E. and Fox, A. J. 2016, *ARA&A*, 54, 363–400, `10.1146/annurev-astro-081915-023251`.

Davies, R. D. and Wright, A. E. 1977, *MNRAS*, 180, 71–88, `10.1093/mnras/180.2.71`.

De Leo, M., et al. 2020, *MNRAS*, 495, 98–113, `10.1093/mnras/staa1122`.

Di Teodoro, E. M., et al. 2019, *MNRAS*, 483, 392–406, `10.1093/mnras/sty3095`.

Diaz, J. and Bekki, K. 2011, *MNRAS*, 413, 2015–2020, `10.1111/j.1365-2966.2011.18289.x`.

Erkal, D., et al. 2019, *MNRAS*, 487, 2685–2700, `10.1093/mnras/stz1371`.

Erkal, D. and Belokurov, V. A. 2020, *MNRAS*, 495, 2554–2563, `10.1093/mnras/staa1238`.

Fox, A. J., et al. 2010, *ApJ*, 718, 1046–1061, `10.1088/0004-637X/718/2/1046`.

Fox, A. J., et al. 2013, *ApJ*, 772, 110, `10.1088/0004-637X/772/2/110`.

Fox, A. J., et al. 2014, *ApJ*, 787, 147, `10.1088/0004-637X/787/2/147`.

Fox, A. J., et al. 2018, *ApJ*, 854, 142, `10.3847/1538-4357/aaa9bb`.

Fox, A. J., et al. 2020, *ApJ*, 897, 23, `10.3847/1538-4357/ab92a3`.

Fujimoto, M. and Sofue, Y. 1976, *A&A*, 47, 263–291.

Gardiner, L. T. and Noguchi, M. 1996, *MNRAS*, 278, 191–208, `10.1093/mnras/278.1.191`.

Gibson, B. K., et al. 2000, *AJ*, 120, 1830–1840, `10.1086/301545`.

Graczyk, D., et al. 2020, *ApJ*, 904, 13, `10.3847/1538-4357/abbb2b`.

Hammer, F., et al. 2015, *ApJ*, 813, 110, `10.1088/0004-637X/813/2/110`.

HI4PI Collaboration, et al. 2016, *A&A*, 594, A116, `10.1051/0004-6361/201629178`.

Hopkins, P. F. 2015, *MNRAS*, 450, 53–110, `10.1093/mnras/stv195`.

Hopkins, P. F., Narayanan, D., and Murray, N. 2013, *MNRAS*, 432, 2647–2653, `10.1093/mnras/stt723`.

Hopkins, P. F., et al. 2018, *MNRAS*, 480, 800–863, `10.1093/mnras/sty1690`.

Hummels, C. B., Smith, B. D., and Silvia, D. W. 2017, *ApJ*, 847, 59, `10.3847/1538-4357/aa7e2d`.

Kallivayalil, N., et al. 2006, *ApJ*, 638, 772–785, `10.1086/498972`.

Kallivayalil, N., et al. 2013, *ApJ*, 764, 161, `10.1088/0004-637X/764/2/161`.

Kim, J.-h., et al. 2016, *ApJ*, 833, 202, `10.3847/1538-4357/833/2/202`.

Koposov, S. E., et al. 2023, *MNRAS*, `10.1093/mnras/stad551`.

Krishnarao, D., et al. 2022, *Nature*, 609, 915–918, `10.1038/s41586-022-05090-5`.

Lin, D. N. C. and Lynden-Bell, D. 1977, *MNRAS*, 181, 59–81, `10.1093/mnras/181.2.59`.

———. 1982, *MNRAS*, 198, 707–721, `10.1093/mnras/198.3.707`.

Lu, L., Savage, B. D., and Sembach, K. R. 1994, *ApJ Letters*, 437, L119, `10.1086/187697`.

Lucchini, S., D'Onghia, E., and Fox, A. J. 2021, *ApJ Letters*, 921, L36, `10.3847/2041-8213/ac3338`.

Lucchini, S., et al. 2020, *Nature*, 585, 203–206, `10.1038/s41586-020-2663-4`.

Nidever, D. L., Majewski, S. R., and Butler Burton, W. 2008, *ApJ*, 679, 432–459, `10.1086/587042`.

Nidever, D. L., et al. 2010, *ApJ*, 723, 1618–1631, `10.1088/0004-637X/723/2/1618`.

Pardy, S. A., D'Onghia, E., and Fox, A. J. 2018, *ApJ*, 857, 101, `10.3847/1538-4357/aab95b`.

Peñarrubia, J., et al. 2016, *MNRAS*, 456, L54–L58, `10.1093/mnrasl/slv160`.

Perret, V., et al. 2014, *A&A*, 562, A1, `10.1051/0004-6361/201322395`.

Petersen, M. S. and Peñarrubia, J. 2021, *Nature Astronomy*, 5, 251–255, `10.1038/s41550-020-01254-3`.

Price-Whelan, A., et al. Version v1.6.1, Zenodo, 2022, `10.5281/zenodo.7299506`.

Price-Whelan, A. M. 2017, *The Journal of Open Source Software*, 2, `10.21105/joss.00388`.

Putman, M. E., et al. 1998, *Nature*, 394, 752–754, `10.1038/29466`.

Read, J. I. and Erkal, D. 2019, *MNRAS*, 487, 5799–5812, `10.1093/mnras/stz1320`.

Richter, P., et al. 2013, *ApJ*, 772, 111, `10.1088/0004-637X/772/2/111`.

Richter, P., et al. 2018, *ApJ*, 865, 145, `10.3847/1538-4357/aadd0f`.

Salem, M., et al. 2015, *ApJ*, 815, 77, `10.1088/0004-637X/815/1/77`.

Sembach, K. R., et al. 2003, *ApJ Supplement*, 146, 165–208, `10.1086/346231`.

Shipp, N., et al. 2021, *ApJ*, 923, 149, `10.3847/1538-4357/ac2e93`.

Springel, V. 2005, *MNRAS*, 364, 1105–1134, `10.1111/j.1365-2966.2005.09655.x`.

Springel, V. and Hernquist, L. 2003, *MNRAS*, 339, 289–311, `10.1046/j.1365-8711.2003.06206.x`.

Tepper-García, T., et al. 2019, *MNRAS*, 488, 918–938, `10.1093/mnras/stz1659`.

Toomre, A. and Toomre, J. 1972, *ApJ*, 178, 623–666, `10.1086/151823`.

Turk, M. J., et al. 2011, *ApJ Supplement*, 192, 9, `10.1088/0067-0049/192/1/9`.

van der Marel, R. P. and Kallivayalil, N. 2014, *ApJ*, 781, 121, `10.1088/0004-637X/781/2/121`.

Vasiliev, E., Belokurov, V., and Erkal, D. 2021, *MNRAS*, 501, 2279–2304, `10.1093/mnras/staa3673`.

Wan, Z., et al. 2020, *MNRAS*, 492, 782–795, `10.1093/mnras/stz3493`.

Wang, J., et al. 2019, *MNRAS*, 486, 5907–5916, `10.1093/mnras/stz1274`.

Westmeier, T. 2018, *MNRAS*, 474, 289–299, `10.1093/mnras/stx2757`.

Wiersma, R. P. C., Schaye, J., and Smith, B. D. 2009, *MNRAS*, 393, 99–107, `10.1111/j.1365-2966.2008.14191.x`.

CHAPTER 5

SIMULATIONS OF THE MAGELLANIC CLOUDS: A DISCUSSION FOR THE NON-SCIENTIST

My favorite aspect of doing science is talking about it – discussing the nuances of a new publication with my colleagues, giving seminars explaining my research to other physicists and astronomers, or simply talking about black holes with strangers in an elevator. I wrote this chapter in hopes of starting many more of these conversations. It has not only strengthened my love for public science, but allowed me to see my work in a new light with a much broader impact. If we as scientists continue to nestle ourselves in ever more esoteric niches without bringing the public with us or relating our work to other fields, science literacy is bound to wane. I am extremely grateful to Professor Bassam Shakhashiri and the Wisconsin Initiative for Science Literacy for starting this project and to Cayce Osborne and Elizabeth Reynolds for supporting my participation.

Humans have always been gazing at the heavens, trying to understand what's out there. We started closest to home with our own Solar System. Understanding that the Earth and all the other planets orbit the Sun was crucial to finding our place in the universe. With this information, and continually improving telescope technology, we discovered that all the other dots we could see in the night sky were other suns located at incredible distances from Earth. All of these stars comprised our Milky Way galaxy, which, as recently as the 1920s, was thought to contain all the stars in the universe. But in addition to stars, astronomers saw fuzzy patches in the night sky, dubbed "nebulae." By determining the distances to these nebulae, we discovered that the Milky Way was just one of many, many galaxies in the universe (Hubble, 1925).

Even today, there remain many unanswered mysteries of galaxies. Astronomers in the 1990s used the *Hubble Space Telescope* to estimate that there are two trillion galaxies in the observable universe (Siegel, 2022). And each of these galaxies looks different. The huge variety in appearance and morphology of the universe's galaxies showed astronomers that galaxies are not static objects; they grow and evolve. For this to happen, galaxies need to acquire gas, which then compresses and condenses to form stars. However, as stars form, this gas gets used up, so galaxies continually need new gas. The *Hubble Space Telescope* has shown us galaxies across the entire spectrum – from galaxies that ran out of gas and are only made up of old stars, to bright exciting galaxies with stars forming right now. My work aims to understand how these galaxies acquire new gas and evolve into what we see in the night sky today.

In order to learn about how galaxies get their gas, we need to be able to see that gas. When looking up into the night sky with your naked eyes, or perhaps a backyard telescope, we see starlight (emitted from stars, or reflected off of planets and moons). However, advances in telescope technology have given us the ability to look beyond the light that our eyes can see. Various chemical elements can emit light in the ultraviolet, infrared, microwave, or radio wavelengths, imperceptible to the human eye. By building telescopes that can detect these different frequencies of light, we can see more than just the stars; we can see the gas. And while space may look pretty sparse to our naked eyes, it is very much not empty.

If we observe the sky in radio waves, we see something drastically different than the tiny pinpricks of stars that we are used to. Radio waves trace the existence of cold ("neutral") hydrogen gas, and hydrogen is everywhere. Figure 5.1 shows comparisons between an optical photograph as

Figure 5.1: The night sky in optical and radio waves. Three versions of a photograph taken by Colin Legg of the Milky Way disk and Magellanic Clouds. The original (optical) photo is in the top left showing what you would see with your naked eye. The top right photo is what would appear if we could photograph radio waves showing the neutral hydrogen in the sky. The Milky Way disk and Magellanic Clouds are still clearly visible. The bottom photo shows the neutral hydrogen only associated with the Magellanic Clouds. The two galaxies are the bright spots at the top center of the image (LMC on top, SMC below) and the Magellanic Stream extends out towards the right edge of the image. The Leading Arm clumps are to the left of the Magellanic galaxies.

we would see with our naked eyes ("optical," top left) and the neutral hydrogen in the sky traced by radio wave emission (top right). The bright band of stars on the left side of the optical image (top left) is the disk of our Milky Way galaxy. Our disk is also very bright in radio waves (top right) since it is where most of the hydrogen gas resides. We can also see two bright spots at the top center in both images. These are the Large and Small Magellanic Clouds (LMC, above; SMC, below). They are two other galaxies outside the Milky Way. And as we can see from the top right image, they aren't just made up of stars, they have a lot of hydrogen gas as well. If we isolate just the gas associated with the Magellanic Clouds, we are left with the image on the bottom of Figure 5.1. A huge amount of hydrogen is not only overlapping with the stars of these galaxies, but extending out all around them. This extensive network of gas covering the sky is the mystery that I have been trying to explain through this work – the Magellanic Stream.

5.1 The Magellanic System

Although faint, the stars in the Magellanic Clouds are visible with the naked eye from the southern hemisphere. There are innumerable references to the Clouds as "fountains" or "pools of water" in the sky from cultures in the southern hemisphere such as the Mapuche in Chile and the Tupi-Guaranis in Brazil (Dennefeld, 2020). From the 16th Century, they were dubbed "Nubecula Minor" and "Nubecula Major" in scientific publications. It wasn't until the end of the 19th Century when the galaxies began to be associated with Ferdinand Magellan's name. This was presumably because they feature prominently in the astronomers' and navigators' writings from his circumnavigation of the globe in 1519 (Dennefeld, 2020).

Today, we know the LMC and the SMC as dwarf galaxies that are currently orbiting the Milky Way. Our Galaxy has many "satellite" galaxies, but the Magellanic Clouds are the two biggest. They are also the only two that still have any gas. Additionally, we know that the Clouds have been experiencing strong gravitational forces. Both of their disks are warped and misshapen (they are both technically classified as "irregular galaxies"). We can also see a bridge of gas and stars extending between the galaxies (D'Onghia and Fox, 2016). All of these observations point to the Clouds most likely having had a collision a few hundred million years ago (very recently on the scale of galaxies!), and possibly more interactions in the past.

In addition to the LMC, SMC, and "Magellanic Bridge" mentioned above, the Magellanic System includes the Magellanic Stream, originally observed in the 1970s. Don Mathewson and collaborators used newly acquired radio telescope data from the Parkes Observatory in Australia to identify a continuous stream of gas trailing behind the Magellanic Clouds (Mathewson et al., 1974). They gave it the name the Magellanic Stream, and in the decades since its discovery we have learned a tremendous amount about it. Improved telescopes have given us incredible, high-resolution images of the hydrogen gas in the Stream (like we can see in Figure 5.1). These observations allow us to map the distribution of cold gas.

We call this cold gas "neutral" because it is comprised of hydrogen atoms that still have their electrons. In its natural state, hydrogen has a proton and an electron, making it electrically neutral. However, if the gas gets hot, these hydrogen atoms are moving much more quickly and colliding into each other with much more energy. These collisions dislodge the electrons, "ionizing" the hydrogen. We can see the (neutral) hydrogen in radio waves because of its electron changing energy levels. Since ionized hydrogen has lost its electrons, we have to detect this hot gas another way.

The technique scientists have used to observe this hot, ionized gas is called "absorption-line spectroscopy" and it has been put to good use in the Magellanic System. While we aren't able to take a picture of the hot gas like what we see in Figure 5.1 for the cold gas, we can still estimate how much of it there is. And it turns out that this ionized material constitutes the majority of the total mass of the Stream! Andy Fox and collaborators in 2014 found that what we can see in the bottom image in Figure 5.1 is actually just a quarter of the total gas that the Magellanic Clouds are bringing with them (Fox et al., 2014). The hot gas makes up the remaining 75%! As we will see below, this observation was one of the key inspirations for my work.

5.2 Previous Theories

We know a lot about the Magellanic Stream, but one piece of the puzzle that we still haven't worked out is where it came from. People have been trying to understand the origin of the Magellanic Stream ever since it was first discovered (Fujimoto and Sofue, 1976; Davies and Wright, 1977; Murai and Fujimoto, 1980; Gardiner and Noguchi, 1996; Mastropietro et al., 2005). Some of the best tools we have for this exploration are computer simulations. However, back in the 70s and 80s, computers weren't nearly powerful enough to simulate the full evolution of the Magellanic Clouds. As computers have improved, our simulations have improved as well. But there have also been a few key observations that have paved the way for us to learn about the history of the Magellanic Clouds.

Originally, it was thought that in order to form the Magellanic Stream, the LMC and the SMC must have been orbiting around the Milky Way for most of the age of the universe. However, once we were able to actually measure their velocities, astronomers determined that the Clouds are moving very fast (Kallivayalil et al., 2006). So fast in fact, that they couldn't have already gone around the Milky Way (Besla et al., 2007). By starting with the Clouds in their present-day positions, with their present-day velocities, we can calculate the gravitational forces on them to trace their positions backwards in time. While this depends on the mass of our Galaxy, and can't account for many of the phenomena that affect the gas, it is a good approximation. This backwards tracing shows us that the most likely scenario is that the LMC and SMC are currently moving away from us after just having approached our Galaxy for the first time (Besla et al., 2007).

The first models of the formation of the Stream in this "first-infall" paradigm were published by Gurtina Besla in 2010 (Besla et al., 2010; Besla et al., 2012). She found that we can still form the Trailing Stream through interactions between the LMC and SMC (instead of through interactions between the LMC and the Milky Way). This model was able to reproduce many of the observed features in the Stream, and was consistent with the very high velocities of the Clouds that we observe today. Figure 5.2 shows a schematic contrasting the original models in which the Clouds orbit the Milky Way multiple times (black dashed line), with the first-infall model where the LMC and SMC have just had their first approach to our Galaxy (black solid line).

However, upon realizing that the Stream is mostly ionized (Fox et al., 2014), this model hit a bit of a rough patch. Not only was there no ionized gas predicted in Gurtina's models (there was no mechanism included to heat up the gas), but there was only a small amount of gas stripped out into the Trailing Stream. Andy Fox's work showed that the total mass in the Magellanic System was four times larger than previously thought. A previous graduate student here at UW–Madison, Stephen Pardy, wrote several papers on the evolution of the Magellanic Clouds exploring this issue. In one published in 2018, he increased the amount of gas the LMC and SMC started with in the simulations in an attempt to explain the massive amount of ionized material (Pardy et al., 2018). However, he was still unable to reconcile these models with the ionized gas observations.

5.3 The Magellanic Corona

Building on the work by Gurtina and Stephen, I began my PhD looking to explain the ionized gas in the Stream. It didn't seem like the ionized gas could come from the disks of the Magellanic Clouds (Stephen's work), so we needed a new source for this material. But are there any other parts of a galaxy that we could consider? That depends on the galaxy's mass.

Determining the total mass of a galaxy is very difficult because galaxies are mostly comprised

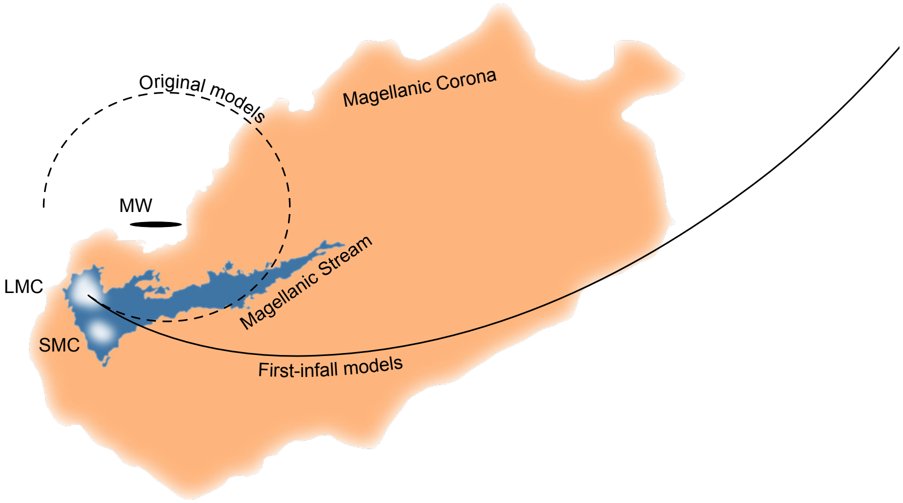

Figure 5.2: First-infall of the Magellanic Clouds. A schematic showing a zoomed-out view of the LMC and SMC relative to the Milky Way (the Milky Way disk is shown edge-on as the black oval labelled MW). The lines show the orbital histories of the Magellanic Clouds contrasting the original, multiple-passage model (dotted line) with the first-passage model (solid line) in which the LMC and SMC have just recently approached the Milky Way. Also shown is a sketch of the cold, neutral Magellanic Stream (blue) trailing behind the Clouds embedded within the massive, ionized Magellanic Corona (orange).

of invisible “dark matter.” We need to look for how galaxies are affecting their environments indirectly. There are many different techniques used to “weigh” the Magellanic Clouds (focusing mostly on the LMC since it is larger). One such method uses the fact that the Clouds just passed their first closest approach to our Galaxy. By Newton’s Third Law (for every action, there is an equal and opposite reaction), if the Milky Way is pulling on the LMC, then the LMC is also pulling on the Milky Way. So by looking for signs that the Milky Way has moved, we can measure just how much the LMC was pulling on our Galaxy – giving us an estimate for its mass. This has been done and we do in fact see a shift in the center of the Milky Way’s disk when compared to the stars in its outer halo (Petersen and Peñarrubia, 2021). Using this technique and others, scientists have estimated that the LMC’s mass is roughly 10% of the mass of the Milky Way.

These estimates now put the mass of the LMC above a special threshold. Small galaxies consist of stars and sometimes gas in their disk, embedded within dark matter. But more massive galaxies can gravitationally hold onto more material. This additional gas gets heated up through repeated collisions and can provide a supporting pressure force due to its increased temperature. Therefore, in addition to the stars and gas in their disk, larger galaxies often are surrounded by a spherical “corona” containing more gas that can slowly feed the disk and fuel continued growth of the galaxy.

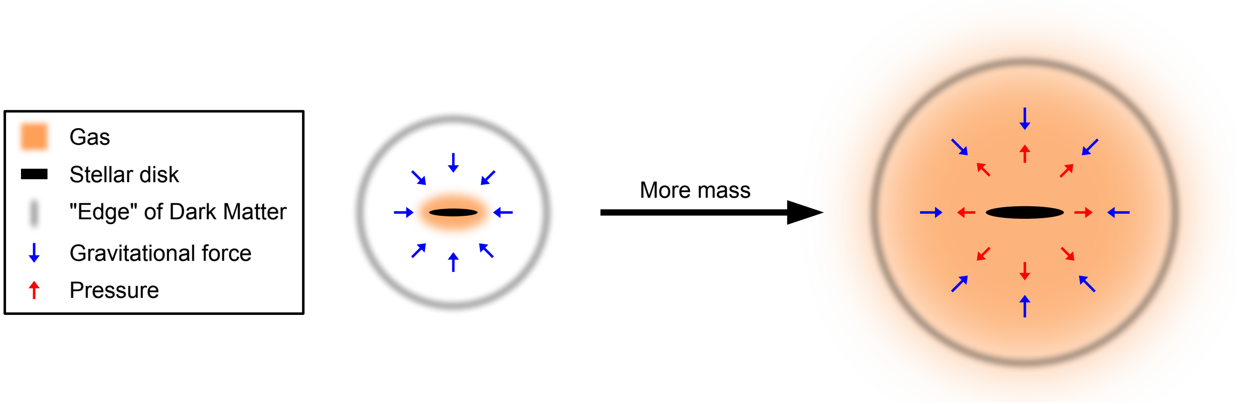

Figure 5.3: Galaxies with coronae. This schematic shows that for low mass galaxies, the gas resides in their disks because it isn't heated sufficiently to provide a supporting pressure force. Whereas in higher mass galaxies, the gas is heated through repeated collisions and fills the volume of space between the disk and the "edge" of the dark matter halo. Gas is shown in orange, the stellar disks are the black ovals, and the extent of the dark matter is shown as a blurred grey line. The blue arrows represent contraction due to gravity, and the red arrow show forces provided by gas pressure.

Figure 5.3 shows the locations of stars and gas relative to the extent of dark matter for low and high mass galaxies. At 10% of the size of the Milky Way, the LMC would be in the category of galaxies with coronae (Jahn et al., 2021). We now have a new possible source of ionized material for the Magellanic Stream – this spherical reservoir of gas around the LMC. We called this reservoir the "Magellanic Corona" and my work was to run simulations of the evolution of the Clouds to determine if this Magellanic Corona could supply enough gas to match the observations.

5.3.1 Ionized Gas Results

Based on my simulations, the Magellanic Corona can provide the ionized gas that we see around the Magellanic System today. As the LMC and SMC dance around each other, they strip cold gas out of their disks into the Magellanic Stream just as figure skaters spin around each other and fling their partners out into tremendous jumps. That is the same as Gurtina Besla's model, however now all of this is happening while they are embedded within the Magellanic Corona. So once the Magellanic System approaches the Milky Way, the Magellanic Corona forms a cocoon around the Clouds and the Stream, enveloping the stripped gas with ionized material (see Figure 5.2). The distribution and the total mass of the ionized gas in my simulations agree with the observational predictions from Andy Fox (Fox et al., 2014), and we still see the cold Stream consistent with the radio maps in Figure 5.1. Figure 5.2 shows the cold Stream in blue, embedded within the

Magellanic Corona shown in orange. The Corona has been warped and shaped as it approached the Milky Way and matches what we see in the sky today. Figure 5.4 shows the observed gas mass in the Trailing Stream (left bar) compared with three different models: the original first-infall model from Gurtina Besla, the modified model from Stephen Pardy trying to strip more gas out of the Clouds, and my new model in which the Magellanic Corona provides the ionized gas in agreement with the observations.

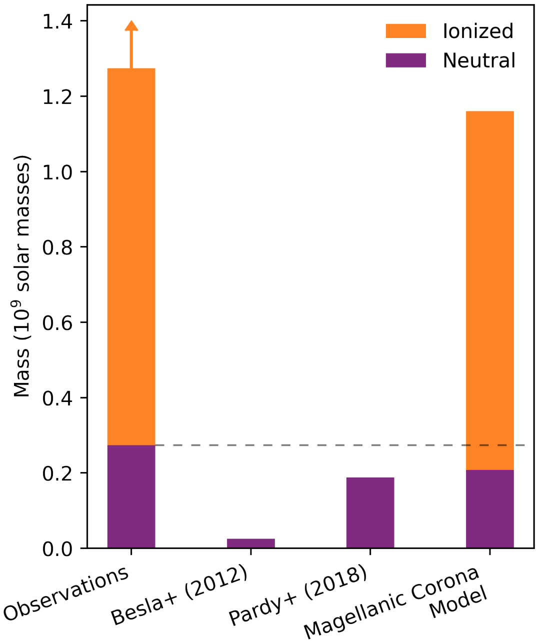

Figure 5.4: Stream mass for different models. Each column represents a different model and the height of the bars show the total mass in each of the components. Purple shows contributions from the cold, neutral gas, and orange is hot, ionized gas from the Magellanic Corona. The left-most bar are the observed values for the gas in the Stream from Brüns et al. (2005), the next two bars are the results of simulations performed by Gurtina Besla and Stephen Pardy (Besla et al., 2012; Pardy et al., 2018), and the right-most bar summarizes the results from my work showing that the Magellanic Corona can provide the ionized mass in the Stream in agreement with the observations.

So what's still missing from this new model? Well, the inclusion of the Magellanic Corona means that the positions of the Magellanic Clouds in the past aren't quite the same anymore. We're not only trying to find out where the Stream came from, we also want to know how exactly the Magellanic Clouds approached the Milky Way, i.e. what were their orbits in the past? Gurtina found an orbit for the Clouds that matched up the positions and velocities of the LMC and SMC in the simulation with their observations. But once we change what the galaxies look like (add in the Magellanic Corona), we change the gravitational and gas pressure forces that the galaxies feel, so that orbit doesn't work anymore. The main problem with my first model was that my simulated Magellanic Clouds didn't match up with their observed counterparts today.

5.4 Magellanic Orbits

The SMC is orbiting around the LMC while both galaxies are embedded within the Magellanic Corona. So now the SMC has to push through this additional gas as it moves around the LMC. Instead of biking on a nice clear day, imagine you are the SMC and now you have to bike through a strong headwind. You won't get nearly as far as you would have on the clear day because the wind is working against you. This is what's happening to the SMC as it tries to push through the Magellanic Corona. This additional drag force (called "ram pressure") causes the SMC to lose energy and eventually fall onto the LMC and merge with it. While this will happen in the future, as we observe them today, the Magellanic Clouds are still separated. So in order for the LMC and SMC to match their present-day positions in the sky, we need the Clouds to be interacting for a shorter amount of time.

The trouble is, we can't simply calculate where the Magellanic Clouds were 5 billion years ago. Based on their positions and velocities today, their masses, and the mass of the Milky Way, we can estimate where they might have been by working our way backwards. But the effects of ram pressure, and the actual stripping of the material out into the Stream are incredibly difficult to calculate in reverse. So using a combination of this "backwards integration" and trial and error, I explored possible alternate orbits for the Magellanic Clouds.

After 134 attempts, we were successful in finding an orbital history for the Clouds consistent with their present-day positions and velocities while including the Magellanic Corona. This history involves two interactions over 3.5 billion years (compared with four interactions over 7 billion years in the previous model; Besla et al. 2012), and we still reproduce the cold and hot gas. The results from this simulation are shown in Figure 5.5. Panel a shows positions of the Clouds (white circles) and the Magellanic Stream gas (purple shading) with respect to the Milky Way (grey oval). This is a similar perspective as in Figure 5.2 (Cartesian coordinates). The past orbits of the LMC and SMC are shown by solid and dashed lines in Panel a and the inset. Panel a also shows the gas density at two times in the past in greyscale. Panel b shows the separation between the Magellanic Clouds over time for our new orbits (solid line) and the previous history (dashed line, Besla et al. 2012). This plot shows that our model has two interactions between the Clouds (the two low points), while the previous model had four.

The most interesting result from this work was the position of the Magellanic Stream gas with respect to the Milky Way. Figure 5.5a (and the zoomed in panel) show the gas getting very close to our Galaxy's disk, closer even than the LMC and SMC themselves. Gurtina's previous model predicted that the gas in the Stream should be much farther away than the Clouds, so our results prompt quite a shift in our understanding of the Magellanic Stream. Interestingly, there

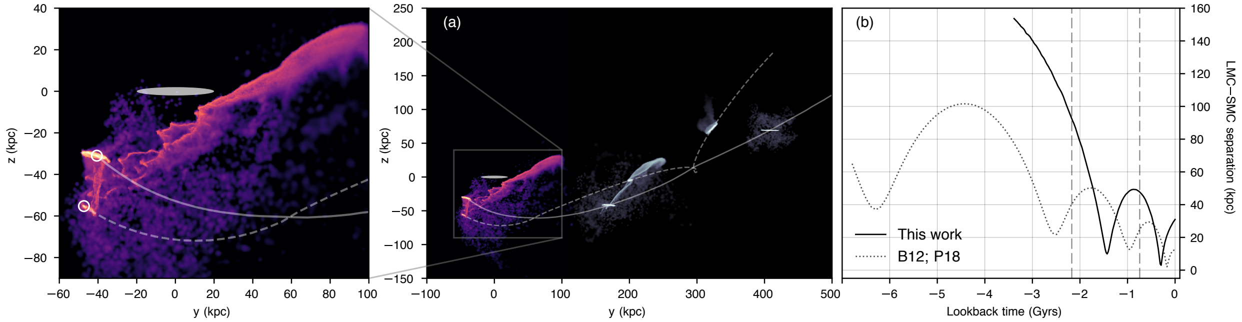

Figure 5.5: The new orbital history for the Magellanic Clouds. This figure shows our simulated Stream relative to the position of the Milky Way (shown as a grey oval). The left panel is a zoomed-in region of Panel (a) which shows the formation of the Stream at the present day (in color) and at two times in the past (750 million years ago, and 2.2 billion years ago). These times are also shown as vertical dashed lines in Panel (b) which shows the separation between the Clouds throughout their interaction history. The solid line is the current model, and the dotted line shows Gurtina Besla's original first-infall model (Besla et al., 2012).

are no observational estimates of the distance to the gas in the Stream. Astronomers have devised ingenious methods for determining the distance to astronomical objects. However, all of these techniques rely on stars. Since there are no stars in the Magellanic Stream (it's all gas), we have no way of knowing its distance.

This means that we have relied on simulations and models to predict how far away the gas in the Stream should be. However, because we predict the gas in the Stream to be so much closer, we may be able to use indirect methods to estimate its distance observationally. In ongoing work, we are looking for stars with known distances that overlap with the Stream on the sky. By using absorption-line spectroscopy (as we did to find the hot gas in the Stream), we can see if the Magellanic Stream is in front of or behind those stars. This would only be possible if the Stream is nearby, so it hasn't been tested before. Hopefully we will be able to learn about the distance to the gas in the Stream which would help us confirm or reject different models in the future.

5.5 Future Directions

Over the course of my PhD, we have developed a new picture for where the Magellanic Stream came from. My research began with unexpected observations of hot gas leading to the discovery of the Magellanic Corona, and moved to exploring the implications of this Corona on the history of the Magellanic Clouds. However, we still have much to do. Looking to the future, I am working on making my simulations more robust. By making them more realistic, I will be able to better compare with the available data to see where my models succeed and where they require improvement. One key area which I will be focusing on is in the calculations for the hot vs cold gas. Previously, we used rough assumptions to separate the neutral and ionized components of the Stream. In my new models, I hope to be able to use the simulation code to directly estimate the temperatures and ionization states of each particle.

This work has not only given us a more complete picture of the Magellanic System today, but it has given us crucial insight into what the Magellanic Clouds looked like in the past. In other simulations, we have seen LMC-like galaxies and we can consider their properties throughout the evolution of the universe, but my work has given us strong constraints on the properties of the real LMC. My simulations have shown that the LMC should have had a Magellanic Corona of gas before it approached the Milky Way. This gives us important information about the evolution and growth of dwarf galaxies of that size.

Furthermore, by understanding the distance to the Magellanic gas, we will have a better idea of how it will affect the Milky Way in the future. One way in which galaxies grow and acquire new gas to form stars is through merger events in which multiple galaxies come together and coalesce. Right here in our very own Milky Way, we have an exciting merger event ongoing with the Magellanic Clouds. By understanding what will happen to this gas, we can learn about how galaxies could refuel their gas supply and continue growing and forming stars.

REFERENCES

Besla, G., et al. 2010, *ApJ*, 721, L97–L101, `10.1088/2041-8205/721/2/L97`.

Besla, G., et al. 2007, *ApJ*, 668, 949–967, `10.1086/521385`.

Besla, G., et al. 2012, *MNRAS*, 421, 2109–2138, `10.1111/j.1365-2966.2012.20466.x`.

Brüns, C., et al. 2005, *A&A*, 432, 45–67, `10.1051/0004-6361:20040321`.

D'Onghia, E. and Fox, A. J. 2016, *ARA&A*, 54, 363–400, `10.1146/annurev-astro-081915-023251`.

Davies, R. D. and Wright, A. E. 1977, *MNRAS*, 180, 71–88, `10.1093/mnras/180.2.71`.

Dennefeld, M. 2020, *The Messenger*, 181, 37–42, `10.18727/0722-6691/5210`.

Fox, A. J., et al. 2014, *ApJ*, 787, 147, `10.1088/0004-637X/787/2/147`.

Fujimoto, M. and Sofue, Y. 1976, *A&A*, 47, 263–291.

Gardiner, L. T. and Noguchi, M. 1996, *MNRAS*, 278, 191–208, `10.1093/mnras/278.1.191`.

Hubble, E. P. 1925, *The Observatory*, 48, 139–142.

Jahn, E. D., et al. 2021, *arXiv e-prints*, arXiv:2106.03861.

Kallivayalil, N., et al. 2006, *ApJ*, 638, 772–785, `10.1086/498972`.

Mastropietro, C., et al. 2005, *MNRAS*, 363, 509–520, `10.1111/j.1365-2966.2005.09435.x`.

Mathewson, D. S., Cleary, M. N., and Murray, J. D. 1974, *ApJ*, 190, 291–296, `10.1086/152875`.

Murai, T. and Fujimoto, M. 1980, *PASJ*, 32, 581–603.

Pardy, S. A., D'Onghia, E., and Fox, A. J. 2018, *ApJ*, 857, 101, `10.3847/1538-4357/aab95b`.

Petersen, M. S. and Peñarrubia, J. 2021, *Nature Astronomy*, 5, 251–255, `10.1038/s41550-020-01254-3`.

Siegel, E. 2022 , `bigthink.com/starts-with-a-bang/how-many-galaxies/`. Accessed 14/4/2023.

CHAPTER 6

CONCLUSION

6.1 Summary

Throughout this work, we have determined a self-consistent explanation for the formation of the Magellanic Stream. Our new model consists of a first-infall trajectory for the Large and Small Magellanic Clouds (LMC, SMC) in which their tidal interactions strip cold, neutral material from the SMC's disk while embedded within the Magellanic Corona, the LMC's warm ionized circumgalactic medium (CGM). This new model is the first to be consistent with both the high mass of the LMC, and with the high ionization fractions observed throughout the Magellanic System (Lucchini et al., 2020).

The ionized Magellanic Corona forms a cocoon around the Clouds and the neutral Stream as the Magellanic System approaches the Milky Way (MW). The MW's own hot CGM provides the hydrodynamical forces that dramatically reshape the Corona from its initially spherical distribution. Prior to its infall into the MW, the Magellanic Corona surrounds the LMC extending out to ~ 100 kpc (Figure 2.2). Even at the present day, the Coronal material covers a large fraction of the sky, in agreement with the large coverage seen in C IV and other high ions that trace the ionized Magellanic material (Figures 2.5, 3.3, and 4.8). Depending on the initial mass of the Corona, we find varying ionized gas masses at the present day, however reasonable values of $> 5 \times 10^9$ ($\sim$3% of the total LMC mass) produce values in agreement with observational estimates (Figures 2.6 and 4.4).

The inclusion of the Magellanic Corona also has strong implications for the orbital history of the Magellanic Clouds themselves. Due to increased ram pressure forces as the SMC orbits the LMC, the Clouds merge much earlier than previous models predicted. The SMC's orbit decays quickly and necessitates a shorter history of interactions between the Clouds. We found a family of orbits in which the Trailing Stream and Magellanic Bridge are formed through two close encounters between the Clouds over ~ 4 Gyr (Lucchini et al., 2021) (Figure 3.1). Due to the orientation of these shorter orbits, the tidally stripped SMC material forming the Stream ends up much closer than predicted by previous models (e.g. Besla et al. 2012; see Figure 3.4). The gas in the Stream reaches as close as 20 kpc from the Sun in our new model (Figures 3.2 and 3.3). This nearby Stream has several important implications:

1. The total mass of the neutral and ionized components in the Magellanic System may need to change depending on the distance to the gas. However, the total physical gas masses may still be quite different from the observational estimates due to the material being at a range of distances.

2. In addition to the gaseous Stream being nearby, we predict that the tidally stripped stellar stream should be nearby as well. While it is still very faint, at 21 mag arcsec^{-2}, this changes its expected location in phase space and requires a new search for this previously undetected component.

3. The morphology of the observed H I filaments is much better explained with a nearby Stream. Due to the interactions with the Magellanic Corona and the MW CGM, we are able to reproduce the filamentary, turbulent structure. Moreover, this also brings the Stream material closer into pressure equilibrium, and can explain the high number of head-tail clouds seen in the data.

4. A nearby Stream can explain the high H α emission along the length of the Stream. Previous models underpredict the H α emission by a factor of $\sim$10 (Barger et al., 2017). By reducing the distance to the Stream to $\sim$20 kpc, this discrepancy is potentially resolved and model predictions seem to align with the observed values.

Finally, we have performed an exploration of the parameter space of initial properties for the Clouds, Magellanic Corona, and MW CGM. This has given us a picture of how the LMC could have evolved and what it would have looked like before its interactions with the SMC and the MW. Additionally, with more advanced simulations, we can now directly compare with absorption-line spectroscopy data making mock observations of specific lines, metallicities, ionization fractions, etc.

This work showed that a Magellanic Corona with an initial mass $> 5\times10^9$ $M_\odot$ and a temperature of 3×10^5 K will self-consistently produce a gaseous disk in agreement with the properties of the LMC disk that we observe today (Figure 4.5). Varying the initial temperature of the Magellanic Corona or the MW CGM did not affect the equilibrium temperature of the circumgalactic gas since that is set through collisional equilibrium and the gravitational potential (Figures 4.2, 4.3). A total SMC mass $< 10^{10}$ $M_\odot$ is required in order for enough gaseous material to be stripped to survive passage through the warm Corona and hot MW CGM. The total mass of the MW's CGM plays a role in the appearance of the neutral and ionized Trailing Stream, and we determined that a value of 2×10^{10} $M_\odot$ best matches the length of the H I Stream and the on-sky extent of the ionized material (Figure 4.7).

With these criteria, we form a Trailing Stream with properties in agreement with the observations – total neutral mass, total ionized mass, ionization fraction, neutral Stream morphology, and ionized gas on-sky distribution (Figure 4.4 and 4.8). We also find additional orbital configurations in which tidally stripped SMC material is thrown out ahead of the Clouds to form the Leading Arm (Figure 4.9). While these models are not able to reproduce the properties of the Trailing Stream as well, it is encouraging that we are able to match the structure and morphology of the Leading region while including the Magellanic Corona and MW CGM.

6.2 Future Work

There are several ways in which we plan to move this work forward. First of all, we wish to test our prediction of a nearby Stream. Due to previous models predicting distances of > 100 kpc, there had not been observational methods available to constrain the distance to the gas in the Stream. But at distances < 50 kpc, we can use absorption-line spectroscopy to get distance limits to the gas observationally. We have an ongoing project in which we are looking for absorption at Magellanic velocities in the spectra of MW halo stars with known distances. If Magellanic absorption is detected, we know the Stream gas at that location is closer to us than the star. If absorption is not detected, the Stream gas is farther than the halo star. This technique has been used before however due to technological limitations, stars only out to 12.6 kpc were studied (Lehner and Howk, 2011). We currently have an accepted proposal led by Dr. Andrew J. Fox at the Very Large Telescope (VLT)[1] to observe six targets near the tail of the Stream with distances of $15 - 60$ kpc. These results will be a critical factor in discriminating between models in the future.

On the theoretical side, further work needs to be done in exploring the small-scale structure of the Clouds and the Stream. With a new orbital history for the Clouds and the additional gaseous component from the Magellanic Corona, a comprehensive analysis of the disks of the LMC and SMC

---

[1] `https://www.eso.org/public/teles-instr/paranal-observatory/vlt/`

is required. Our new models are able to reproduce the broad features of the Magellanic System including its total mass, proper motions, and morphology. However, the incredible wealth of data on the stellar structures in the Clouds (e.g. Schmidt et al., 2022; Cullinane et al., 2022) as well as the high-resolution 21 cm observations (e.g. Dickey et al., 2013; Pingel et al., 2022) necessitates an in-depth exploration of the LMC and SMC disk features within the simulations.

One concrete method to do this is to explore the relationship between the tidal interactions between the Clouds and the properties of the turbulence in the neutral gas within their disks. By analyzing the extremely high-resolution data upcoming from the GASKAP project (Dickey et al., 2013; Pingel et al., 2022), we may be able to constrain the impact parameter of the SMC's most recent collision with the LMC by comparing with simulations. With small enough impact parameter (as is indicated by orbital integrations; Zivick et al. 2018), we may even be able to indicate where on the LMC's disk the SMC punched through.

Additionally, high-resolution simulations must explore the role of the interaction history of the Magellanic Clouds on the unique, asymmetric structures observed in their disks today. Within the LMC, there are multiple offset features including a gaseous overdensity in the eastern disk, a stellar "bar" in the southern disk, a single spiral arm, and the explosive 30 Doradus region. The SMC also hosts several mysteries including multiple velocity components, multiple stellar populations, and a line of sight depth of up to 20 kpc. Reproducing these features through tidal interactions could give us useful clues about the history of the Clouds further constrain models of the formation of the Stream.

Finally, inspired by these indications of a Magellanic Corona around the LMC, I plan to explore a more general view of the CGM around galaxies. Specifically looking at the role of galactic merger events in the larger picture of galaxy evolution and gas acquisition. Recent explorations into the properties of the gas around galaxies has uncovered a complex multiphase medium consisting of higher metallicity gas than was expected. The interplay between this complex CGM and galaxy growth is yet not well understood. Are satellites depositing cold material out at large distances around galaxies (as we see with the Magellanic System)? Or are satellite passages driving instabilities that seed the condensation of cold clouds out of the hot gaseous material? Or is this multiphase medium maintained through gas flows within the galaxy itself – is star formation fueled by these cold, high density clouds which then induce supernova outflows which blow out high metallicity gas to seed cold cloud growth?

This work has not only allowed us to get several steps closer to an understanding of the formation of the Magellanic Stream, but it has given us intriguing insight into the properties of dwarf galaxies and their circumgalactic gas, gas acquisition and metal transport around star forming galaxies, and how interactions can shape galaxy morphologies. Moving forward, improved simulations and computational advancements will make the field of galaxy evolution simulations even more fruitful and I am excited to play a part in understanding future mysteries.

REFERENCES

Barger, K. A., et al. 2017, *ApJ*, 851, 110, `10.3847/1538-4357/aa992a`.

Besla, G., et al. 2012, *MNRAS*, 421, 2109–2138, `10.1111/j.1365-2966.2012.20466.x`.

Cullinane, L. R., et al. 2022, *MNRAS*, 510, 445–468, `10.1093/mnras/stab3350`.

Dickey, J. M., et al. 2013, *PASA*, 30, e003, `10.1017/pasa.2012.003`.

Lehner, N. and Howk, J. C. 2011, *Science*, 334, 955, `10.1126/science.1209069`.

Lucchini, S., D'Onghia, E., and Fox, A. J. 2021, *ApJ Letters*, 921, L36, `10.3847/2041-8213/ac3338`.

Lucchini, S., et al. 2020, *Nature*, 585, 203–206, `10.1038/s41586-020-2663-4`.

Pingel, N. M., et al. 2022, *PASA*, 39, e005, `10.1017/pasa.2021.59`.

Schmidt, T., et al. 2022, *A&A*, 663, A107, `10.1051/0004-6361/202142148`.

Zivick, P., et al. 2018, *ApJ*, 864, 55, `10.3847/1538-4357/aad4b0`.

APPENDIX A

ADDITIONAL PUBLISHED WORKS

Introduction

During my graduate career, I have also published two first-authored papers studying stellar dynamics within the Milky Way. These projects were completed through collaboration with a UW undergraduate, Emil Pellett, class of 2023.

The goal of these works were to investigate stellar velocities around the Sun and throughout our Galaxy's disk in an attempt to constrain properties of the Milky Way's bar. We have known that our Galaxy hosts a bar since the 1990s, however its length, rotation speed, and angle with respect to the Sun are not strongly constrained. Nonaxisymmetric features, such as a bar, induce resonances that can trap stars and form comoving groups of stars. The distribution and properties of these stellar "moving groups" can give us valuable information on the Galactic bar through these resonances.

This work was made possible due to the immense amount of stellar data obtained using the *Gaia* satellite launched in 2013. June 2022 marked its third data release including full 6D position and velocity information for more than 33 million stars. This immense data set allowed us to investigate the dynamics of the Milky Way like never before.

We were particularly interested in investigating kinematic "moving groups." These are groups of stars with similar velocities (they are clustered in the Galactocentric azimuthal vs radial velocity plane). It is particularly important to note that these stars were not necessarily born together; they won't have the same ages or metallicities, and they won't be clustered in physical space. These stars have grown to move with the same velocities through gravitational forces within the Milky Way. Therefore, studying them can give us incredible insights into the structure of our Galaxy.

In order to investigate these moving groups, we developed an open-source Python implementation of an image analysis technique called a "wavelet transformation." This technique allows us to identify structures with a specified size in images, in our case 2D histograms (the azimuthal vs radial velocity plane). In Section A.1, we use this wavelet transformation to detect overdensities (corresponding to these kinematic moving groups) in this velocity plane of stars near the Sun. We also track these groups throughout the Galactic disk. In Section A.2, we explore one classical moving group in particular, Hercules. Based on how its properties vary across Galactocentric azimuth, we are able to add to the evidence for a long, slow bar in our Galaxy.

Monthly Notices
of the
ROYAL ASTRONOMICAL SOCIETY

MNRAS **519,** 432–444 (2023)
Advance Access publication 2022 December 2

https://doi.org/10.1093/mnras/stac3519

Moving groups across Galactocentric radius with *Gaia* DR3

Scott Lucchini [1★] Emil Pellett,[1] Elena D'Onghia[1,2] and J. Alfonso L. Aguerri[3,4]

[1]*Department of Physics, University of Wisconsin - Madison, Madison, WI, USA*
[2]*Department of Astronomy, University of Wisconsin - Madison, Madison, WI, USA*
[3]*Instituto de Astrofísica de Canarias; C/ Vía Láctea s/n, 38200, La Laguna, Spain*
[4]*Departamento de Astrofísica, Universidad de La Laguna, E-38206 La Laguna, Spain*

Accepted 2022 November 24. Received 2022 November 18; in original form 2022 June 21

ABSTRACT

The kinematic plane of stars near the Sun has proven an indispensable tool for untangling the complexities of the structure of our Milky Way (MW). With ever improving data, numerous kinematic 'moving groups' of stars have been better characterized, and new ones continue to be discovered. Here we present an improved method for detecting these groups using *MGwave*, a new open-source 2D wavelet transformation code that we have developed. Our code implements similar techniques to previous wavelet software; however, we include a more robust significance methodology and also allow for the investigation of underdensities, which can eventually provide further information about the MW's non-axisymmetric features. Applying *MGwave* to the latest data release from *Gaia* (DR3), we detect 47 groups of stars with coherent velocities. We reproduce the majority of the previously detected moving groups in addition to identifying three additional significant candidates: one within Arcturus, and two in regions without much substructure at low $V_{\rm R}$. Finally, we have followed these associations of stars beyond the Solar neighbourhood from Galactocentric radius of 6.5–10 kpc. Most detected groups are extended throughout radius indicating that they are streams of stars possibly due to non-axisymmetric features of the MW.

Key words: Galaxies – Stars – Galaxy: kinematics and dynamics $<$ The Galaxy – stars: kinematics and dynamics $<$ Stars – methods: data analysis $<$ Astronomical instrumentation, methods, and techniques – solar neighbourhood $<$ The Galaxy.

1 INTRODUCTION

Even a relatively small region of the Milky Way (MW) around, our Sun contains a wealth of information about the larger properties and non-axisymmetric features of our Galaxy. By studying the motion of nearby stars, we can begin to untangle the many complex components of the gravitational potential of the MW, including the bar and spiral arms. We have also seen evidence that the stellar disc is out of equilibrium with the discovery of local vertical features like the Radcliffe Wave (Alves et al. 2020) and a more extended vertical kinematic wave (Thulasidharan et al. 2021). Since the Hipparcos mission, scientists have slowly been uncovering more and more detail in the kinematic grouping of stars in the Solar neighbourhood ('moving groups'; Eggen 1996; Dehnen 1998; Ramos, Antoja & Figueras 2018). The intricacies of the azimuthal velocity (V; V_ϕ) versus radial velocity (U; $V_{\rm R}$) distribution of nearby stars show that the MW is anything but a smooth galactic disc in dynamical equilibrium (Dehnen 1998; Antoja et al. 2018). By studying the origin of these substructures with the advent of *Gaia* (Gaia Collaboration et al. 2016) and, at the same time, utilizing various theoretical approaches (Quillen et al. 2011; Fujii et al. 2019; Monari et al. 2019; D'Onghia & L. Aguerri 2020; Craig et al. 2021; Trick et al. 2021), we can gain insights on the various components of the MW, and understand better galactic structure and evolution.

One of the least well-constrained features of the MW is its bar. This non-axisymmetric feature can have a significant gravitational potential, and can affect the distribution of stars through resonances. Depending on the length and pattern speed of the bar, it could provide different explanations for many of the moving groups that we see in the Solar neighbourhood (SN). For example, previous models of the MW included a short bar with a pattern speed of $\sim$55 km s^{-1} kpc^{-1}, where the outer Lindblad resonance (OLR) coincided with the SN (Dehnen 2000; Debattista, Gerhard & Sevenster 2002; Monari et al. 2017). The OLR creates a bimodality in the kinematic plane of stars around the Sun providing one possible explanation for the Hercules group. However, recent observations before *Gaia* DR3 already suggest that the bar is actually long and rotating more slowly ($\sim$40 km s^{-1} kpc^{-1}; Clarke et al. 2019; Sanders, Smith & Evans 2019). Theoretical models and simulations have shown that Hercules could be formed by stars at the corotation resonance of a long bar (Pérez-Villegas et al. 2017; Asano et al. 2020; D'Onghia & L. Aguerri 2020). Furthermore, several of the significant moving groups in the SN are explained by being in resonance with the long bar (the Outer Lindblad resonance (2:1), the 4:1 or the outer ultra-harmonic resonance, and the 6:1 correspond to the Hat, Sirius, and the Horn, respectively; Monari et al. 2019). The MW's spiral arms have also been shown to have a significant effect on the kinematics of the SN (e.g. Antoja et al. 2009; Hunt et al. 2018; Michtchenko et al. 2018; Barros et al. 2020). While looking at the resonances in the SN alone are not sufficient to break the degeneracy to discriminate between the long and short bar scenarios (Trick et al. 2021; Trick 2022), *Gaia* DR3 provided the data to observe the bar in the azimuthal velocity field of the galaxy, and indicate that the pattern

---

★ E-mail: lucchini@wisc.edu

Published by Oxford University Press on behalf of Royal Astronomical Society

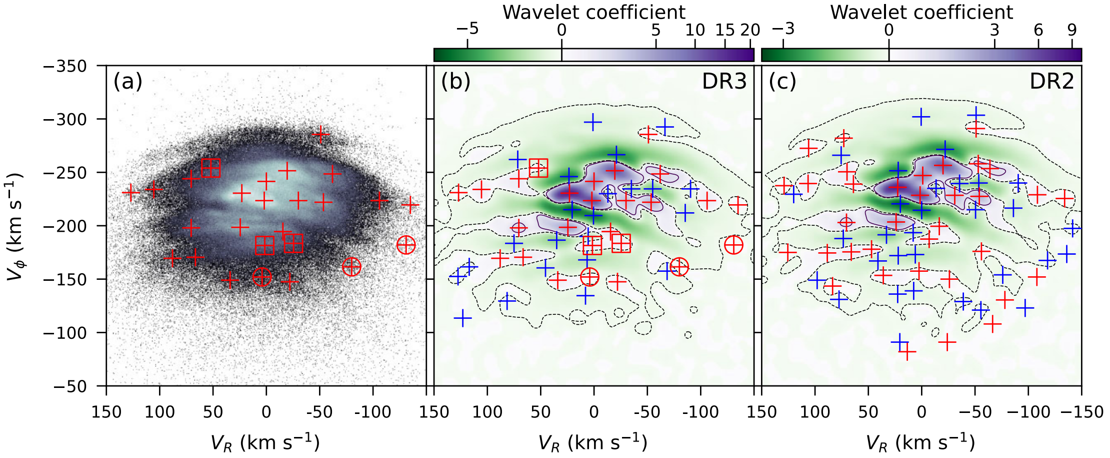

Figure 1. Panel (a) shows the 2D histogram of all the SN stars in the V_{R}–V_ϕ kinematic plane using *Gaia* DR3 with a bin size of 0.5 km s^{-1}. Overplotted are the locations of the wavelet maxima using DR3 data (as in Panel (b), see below). Panels (b) and (c) show the results of the wavelet transformation for DR3 and DR2, respectively, shown at a scale of 8–16 km s^{-1}. The purple and green regions depict the relative strength of the positive and negative wavelet coefficients, respectively, normalized by square-root. Contours are shown at the −0.1 (dashed) and 5 per cent levels. Red markers represent significant overdensities and blue markers represent significant underdensities. Note that only extrema with confidence level ≥2 and $P_{\mathrm{MC}} > 0.8$ are shown. The DR3 overdensities are also shown overlaid onto panel (a). In panels (a) and (b), the three new group candidates (DR3G-25, 26, and 31) are circled and those groups previously detected but missing from prior studies using *Gaia* are enclosed within squares (Kushniruk17-J4-19, HR1614, and Zhao09-9; marked with asterisks in Table 1).

speed is between 38-42 km s^{-1} kpc^{-1} (Gaia Collaboration et al. 2022b).

Gaia constitutes the largest and most precise data base of positions and velocities of stars in the MW to date, which makes it perfect for this exploration (Gaia Collaboration et al. 2016). Its latest release (Data Release 3 (DR3); Gaia Collaboration et al. 2022a) provides improved astrometry and errors for 1.4 billion stars based on 34 months of data. For this study, we include approximately 34 million stars centred on the Sun for which *Gaia* provides positions, proper motions, parallaxes, and radial velocities.

While much of the structure in the V_{R}–V_ϕ kinematic diagram is clearly visible as overdensities (e.g. Fig. 1a), more sophisticated methods are required to quantify the wealth of information. One such technique is the wavelet transformation. Much like a Fourier transformation, the wavelet transform (WT) decomposes data into different components based on a given scale (see Starck, Murtagh & Bijaoui 1998, and references therein). When applied to 2D images, the WT can isolate visual structures of different sizes. This technique has been used on a variety of astrophysical data, where it allows for the detection of subtle variations from uniformity, e.g. cosmological large-scale structure (Slezak, de Lapparent & Bijaoui 1993; Einasto et al. 2011), galaxy cluster distributions (Girardi et al. 1997; Da Rocha & Mendes de Oliveira 2005; Da Rocha, Ziegler & Mendes de Oliveira 2008), and the cosmic microwave background (Sanz et al. 1999; Rogers et al. 2016; Hergt et al. 2017).

Recent work has also utilized the WT to explore the kinematic space of the MW (Antoja et al. 2008; Zhao, Zhao & Chen 2009; Zhao et al. 2014, 2015; Kushniruk, Schirmer & Bensby 2017; Ramos et al. 2018; Yang et al. 2021; Bernet et al. 2022). Ramos et al. (2018) (hereafter R18) used *Gaia* DR2 and the WT to detect moving groups in the V_{R}–V_ϕ plane, and found many arch features covering the majority of previously known moving groups. In addition to detecting 28 new overdensities, they traced V_ϕ of the groups over radius and azimuth to compare with the detected ridges in V_ϕ–R space (Antoja et al. 2018). The outcome showed that there are kinematic features indicative of both phase mixing processes as well as resonant trapping due to the MW's non-axisymmetric structures.

Similarly, Bernet et al. (2022) explored a larger region of the MW disc using *Gaia* eDR3, and the WT combined with a breadth-first search to group detected overdensities together in (R, ϕ, Z, V_{R}, V_ϕ) space. The WT they use is one-dimensional and was specifically designed to detect and group overdensities into the arches found in R18. They again explore the variation in V_ϕ versus R for each detected group in addition to looking at the distribution of V_ϕ along ϕ and z. By comparing both slow- and fast-bar models, they find several resonances that overlap with the detected groups/arches, however *Gaia* eDR3 was not extended enough to determine the bar's length and pattern speed in order to remove the degeneracy.

For this work, we have developed an open-source WT code for use in PYTHON, *MGwave*[1]. The code is based on the *á trous* algorithm (Starck & Murtagh 1994; Starck et al. 1998), and is able to perform the wavelet transformation on any 2D image and output the resultant wavelet coefficients, locations of the extrema, as well as a significance, or confidence level for each extremum (when compared to values resulting from Poisson noise). We build on previous works by using our *MGwave* code to analyse the SN as seen by *Gaia* DR3. By performing the full 2D WT, we not only detect new kinematic moving groups, but we are also able to track their extension in the kinematic plane and their location through Galactocentric radius. By identifying moving groups of stars that are extended across the Galactic disc, we can distinguish the large-scale substructures with a dynamical origin (e.g. those stars that might be in resonance with the bar or spiral arms) from local transient features.

This paper is structured as follows: Section 2 outlines our data sample and WT methods, Section 3 shows the main results, Section 4

---

[1] This code is publicly available at https://github.com/DOnghiaGroup/MGwave.

discusses the implications of our results within the context of previous works, and conclusions are summarized in Section 5.

2 METHODS

2.1 *Gaia* data sample

We selected from the approximately 34 million stars that have positions, proper motions, parallaxes, and radial velocities in *Gaia* DR3. In order to avoid the known biases caused by inverting the parallax to find distances, we use the geometric distances, along with their errors, computed by Bailer-Jones et al. (2021) (Bailer-Jones et al. 2020). We transformed the six-dimensional *Gaia* observables to Galactocentric cylindrical coordinates with the Sun located at $\phi_\odot = 0^\circ$, $Z_\odot = 5.5$ pc, and $R_\odot = 8.15$ kpc. We take the peculiar motion of the Sun with respect to the local standard of rest (LSR) in cartesian coordinates as $(U, V, W) = (10.6, 10.7, 7.6)\,\mathrm{km\,s^{-1}}$, and the circular velocity of the Sun as $V_\mathrm{c} = 236\,\mathrm{km\,s^{-1}}$ (Reid et al. 2019). V_R is directed out away from the Galactic Centre, and V_ϕ is directed against the direction of rotation of the disc (i.e. ϕ decreases in the direction of rotation, towards the major axis of the MW bar, and increases counter to the rotation, towards the minor axis of the MW bar).

We used Monte Carlo simulations to transform the *Gaia* errors from right ascention, declination, proper motions, and radial velocities (source properties) into the Galactocentric cylindrical coordinates defined above (final properties). Using the PYIA code (Price-Whelan 2018), we sampled the source *Gaia* data 256 times for each star, assuming a Gaussian distribution for each property. By then transforming the sampled properties into Galactocentric coordinates, we could measure the spread in their values (the standard deviation) to determine the errors in the final properties (R, ϕ, Z, V_R, V_ϕ, V_Z). This method does account for correlations between right ascention, declination, and proper motion, but does not include correlations for radial velocity or the Bailer-Jones distances.

There are 33 653 049 stars with radial velocities and Bailer-Jones distances in *Gaia* DR3. This is increased by more than a factor of four over eDR3. We define the ‘SN’ region as $|z| < 0.5$ kpc, $-1.5^\circ < \phi < 1.5^\circ$, and $8.05 < R < 8.25$ kpc, which contains 997 918 stars. We have also explored additional volumes throughout the Galactic disc by looking at 70 overlapping radial bins of width 0.2 kpc in the range $R = (6.4, 10.1)$ kpc while maintaining the constraints on z and ϕ, specifically (6.4, 6.6), (6.45, 6.65), (6.5, 6.7) kpc, etc. However, we do see a decrease in the number of stars per bin as we reach the limits of this range.

In order to compare with previous works, we have also performed the same analysis with *Gaia*’s Data Release 2 (DR2). We have followed the same procedure as above, however, we have used the definition of Galactocentric cylindrical coordinates as defined in R18 ($Z_\odot = 14$ pc, $R_\odot = 8.34$ kpc, $(U, V, W) = (11.1, 12.24, 7.25)\,\mathrm{km\,s^{-1}}$, and $Vc = 240\,\mathrm{km\,s^{-1}}$ from Schönrich, Binney & Dehnen 2010 and Reid et al. 2014). We have also required ‘good’ parallax values, i.e. $\varpi/\sigma_\varpi > 5$, and distances were calculated by inverting the parallax. This provided us with an identical data set to that of R18. A comparison of our results between DR2 and DR3 is shown in Fig. 1.

2.2 Wavelet transform method

Our open-source WT code, *MGwave*, is based on the *á trous* algorithm (Starck & Murtagh 1994; Starck et al. 1998). We have also implemented quantitative analysis to determine the significance of detected structures with respect to Poisson noise (Slezak et al. 1993). Finally, Monte Carlo simulations are used to propagate data errors through to the wavelet results.

Our implementation of the *á trous* algorithm utilizes the Starlet transformation with a B3-spline scaling function (Starck & Murtagh 2006),

$$\begin{aligned}\phi(x) &= B_3(x)\\ &= \frac{1}{12}\left(|x-2|^3 - 4|x-1|^3 + 6|x|^3 - 4|x+1|^3 + |x+2|^3\right).\end{aligned} \tag{1}$$

Figs 2 a and b shows the continuous scaling function and corresponding wavelet function. Since we are working with pixellated images, we need to discretize these functions. Defined in terms of the h and g filter set (Starck et al. 1998), the scaling function corresponds to $h = \left[\frac{1}{16}, \frac{1}{4}, \frac{3}{8}, \frac{1}{4}, \frac{1}{16}\right]$ and the wavelet function is derived from $g = \delta - h = \left[-\frac{1}{16}, -\frac{1}{4}, \frac{5}{8}, -\frac{1}{4}, -\frac{1}{16}\right]$ (where δ is the discretized delta function, i.e. $\delta = [0, 0, 1, 0, 0]$). These discrete wavelet functions are shown in Figs 2 c–e for three different scales ($j = 0$, 1, and 2). By applying this separable convolution mask to our image in each dimension sequentially, we obtain the wavelet transformed image (consisting of the values of the wavelet coefficients for each pixel). An example image and its wavelet transforms at three different scales ($j = 2, 4$, and 5) are shown in Figs 2 f–i. When performing the wavelet transformation at small scales (panel f), the smallest structures in the original image are selected. As we increase the scale of the transformation, larger and larger features are shown. For a more detailed discussion see Starck et al. (1998).

We then use a peak detection algorithm to find local minima and maxima in the wavelet transformed image. We require that detected extrema are separated by at least the wavelet scale size (2^j). This is accomplished using the `peak_local_max` function in the `scikit-image` package (van der Walt et al. 2014). We then ensure that if there are two peaks or two troughs within 2^j pixels, we only keep the extremum with the larger wavelet coefficient. Once we have located the extrema, we then calculate the significance of each peak and trough to determine whether or not it could be an artefact of Poisson noise.

2.3 Significance of detected extrema

Given a wavelet coefficient, its significance must be computed to assess the probability that the detected extremum is ‘real’. This will give us a confidence level that the value of a wavelet coefficient (pixel in the transformed image) is not due to random Poisson noise. In order to calculate this, we can integrate the WT probability density function, $p_n(w)$, to determine the likelihood that a random wavelet coefficient due to Poisson noise has a lower value than a wavelet coefficient of value w (Slezak et al. 1993; i.e. larger values of $F(w)$ mean w is more significant):

$$F(w) = \int_{-\infty}^{w} p_n(x)\,\mathrm{d}x. \tag{2}$$

The probability density function depends on both the specific wavelet function chosen (in its continuous form, e.g. Fig. 2b), and also on the number of events used to determine the wavelet coefficient. As stated above, we use a B3-spline as the scaling function, ϕ (equation 1). At each wavelet scale, j, we dilate the scaling function by a factor of 2^j, and then renormalize it such that

$$\int_{-\infty}^{\infty} \phi\left(\frac{x}{2^j}\right)\mathrm{d}x = 1. \tag{3}$$

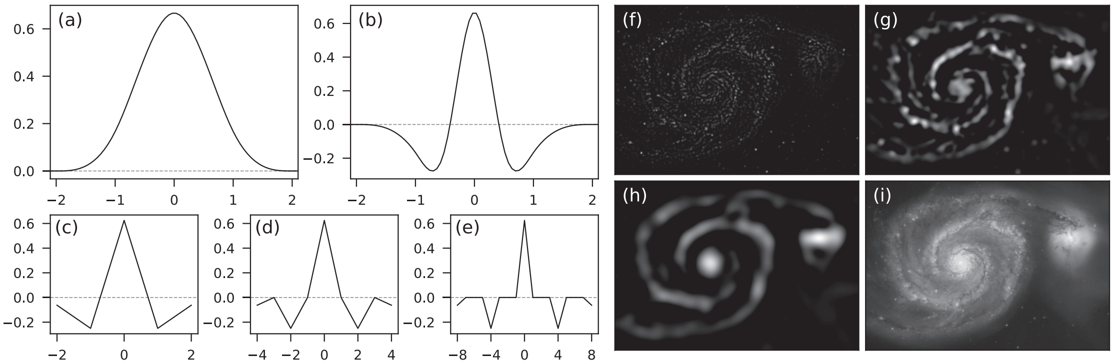

Figure 2. Panels **a** and **b** show the continuous B3-spline scaling function, $\phi(x)$, and the corresponding wavelet function, $\psi(x)$, respectively. Panels **c**−**e** show the discrete wavelet function (generated from the filters h and g) for scales $j = 0$, 1, and 2. Panels **f**−**h** show the resulting wavelet transform of the image of M51 shown in panel **i**.[2] The original image is 720 pixels wide by 1037 pixels high and the scales shown in panels **f**, **g**, and **h** are $j = 2$,4, and 5 resulting in the detection of features with sizes of 4–8, 16–32, and 32–64 pixels, respectively.

We then compute the continuous wavelet function (in 2D), $\psi(x, y)$, by looking at the difference between the scaling functions at two successive scales (Starck et al. 1998).

$$\frac{1}{4}\psi\left(\frac{x}{2}, \frac{y}{2}\right) = \phi(x, y) - \frac{1}{4}\phi\left(\frac{x}{2}, \frac{y}{2}\right), \tag{4}$$

where $\phi(x, y) = \phi(x)\phi(y)$.

The number of events also affects the probability density function. In the case of a 2D histogram (for example, the V_R–V_ϕ kinematic plane used later in this paper), the number of events represents the total number of stars within the bins used in calculating the wavelet coefficient. If there is only one event, the probability to get any given wavelet coefficient is represented by the histogram of the wavelet function, H_1. For two events, each has the probability represented by the histogram of the wavelet function and since they are independent to each other, we can take the autoconvolution of the histogram to represent the PDF for two events (Slezak et al. 1993). Therefore for n events, the PDF is $n - 1$ autoconvolutions of the PDF for a single event.

$$p_n(x) = H_1 * H_1 * \cdots * H_1. \tag{5}$$

We compute the histogram of the wavelet function using the kernel density estimator (`kdeplot`) from the `seaborn` PYTHON package (Waskom 2021). As described in Slezak et al. (1993), a maximum must have $n \geq 3$ and a minimum to be $n \geq 4$ in order for the significance calculation above to be valid.

Therefore, $F(w)$ (equation 2) can be used to determine the confidence level of each extremum via thresholding. We followed the method in R18 setting confidence levels based on these significance values:

$$\begin{aligned} &0 : F(w) < \epsilon_{1\sigma} \\ &1 : \epsilon_{1\sigma} \leq F(w) < \epsilon_{2\sigma} \\ &2 : \epsilon_{2\sigma} \leq F(w) < \epsilon_{3\sigma} \\ &3 : F(w) \geq \epsilon_{3\sigma}, \end{aligned} \tag{6}$$

where $\epsilon_{n\sigma}$ corresponds to the integral of the normal distribution, $N(0, 1)$, from $-\infty$ to n. This gives $\epsilon_{1\sigma} \approx 0.841$, $\epsilon_{2\sigma} \approx 0.977$, and $\epsilon_{3\sigma} \approx 0.999$.

Following previous works (R18), we consider any extremum to be significant if it has a confidence level $\geq$2.

2.4 Monte Carlo simulations

To account for underlying uncertainty in the data, we use Monte Carlo simulations to propagate errors through the WT. Uncertainty values can be supplied for the x and y coordinates for each object (i.e. the data used to create the histogram on which the WT is performed), and *MGwave* will simulate new data by pulling random values from Gaussian distributions. After running this simulation process, many times and performing the WT on each new data set, the code then calculates the number of simulations in which a peak is detected within a circle of diameter 2^j (the scale of the WT) around the actual peak. The workflow is as follows:

(i) Obtain new x and y values for each object by sampling a Gaussian distribution with the associated errors.
(ii) Run the wavelet routine on the new, simulated data obtaining a list of maxima and minima.
(iii) For each extremum in the original data, check if there exists an extremum in the simulated data within a circle of diameter of 2^j.
(iv) Repeat N times.

For the work presented in this Article, we supplied uncertainties in V_R and V_ϕ propagated from the *Gaia* data individually for each star (see Section 2.1) and performed $N = 2000$ iterations. Following previous works (R18), we consider any extremum to be independent of *Gaia* errors if it is reproduced in >80 per cent of the Monte Carlo simulations, i.e. $P_\mathrm{MC} > 0.8$. These values are listed in Table 1.

3 RESULTS

Using *Gaia* DR3, we performed the wavelet transformation on the V_R–V_ϕ kinematic plane. We first binned the *Gaia* data into 600 bins of size 0.5 km s^{-1} (in both dimensions; shown in Fig. 1a). Then we used scales of $j = 2$, 3, 4, and 5 (shown in Fig. 3) for our WT. These scales allow us to detect structures in the histogram with sizes between $\Delta \times 2^j$ and $\Delta \times 2^{j+1}$, where Δ is the bin size (0.5 km s^{-1}). Since most of the stellar moving group structures have sizes of $\sim$10 km s^{-1}, we used the $j = 4$ scale for this analysis which corresponds to structures with sizes between 8 and 16 km s^{-1}. At smaller scales (Fig. 3b), some of the classical moving groups (e.g. Hyades, Coma Berenices, Sirius) break into

Table 1. Moving groups detected using our new wavelet transform on *Gaia* DR3 data. The same naming convention as R18 is followed (see their Appendix C for more information). Groups marked with an asterisk (∗) are those that have been previously discovered but were not present in the wavelet analysis of R18. Bold lines are groups newly discovered in this work. Columns 5–8 list the output of our analysis: CL denotes the confidence level that a given group is not due to Poisson noise (see Section 2.3); P_{MC} gives the percentage of Monte Carlo simulations in which the peak appeared when varying the stellar velocities within *Gaia* errors (see Section 2.4); Wavelet gives the magnitude of the wavelet coefficient at the peak; Stars lists the number of stars in a region of kinematic space around the peak corresponding to the scale of the wavelet transformation performed (in this case within a circle of radius 16 km s^{-1}). References: (1) Dehnen (1998); (2) Zhao et al. (2009); (3) Antoja et al. (2012); (4) Xia et al. (2015); (5) Bobylev & Bajkova (2016); (6) Kushniruk et al. (2017); (7) Liang et al. (2017); (8) R18.

	V_{R} (km s^{-1})	V_{ϕ} (km s^{-1})	Name	CL	P_{MC}	Wavelet	Stars	Refs
1	23.0	−230.5	Hyades	3	1.00	15.9831	139 712	1,2,3,5,7
2	2.0	−223.5	Pleiades	3	1.00	11.9514	145 719	1,2,3,5,7
3	−19.5	−251.5	Sirius	3	1.00	10.6615	111 631	1,2,3,4,5,
4	0.0	−241.5	Coma Berenices	3	1.00	5.7824	147 895	1,2,3,4,5
5	24.5	−198.5	Hercules II	3	1.00	4.3941	54 221	2,3,5,7
6	−53.5	−222.0	Dehnen98-14 (Horn)	3	1.00	3.1135	44 473	1,2,3,5
7	−30.0	−223.5	Dehnen98-6	3	1.00	2.5743	86 079	1,2,5
8	−62.0	−248.5	γLeo	3	1.00	1.3055	27 352	2,3,5,7
9	70.5	−198.0	ϵInd	3	1.00	1.2055	16 928	3,5,7
10	−15.5	−194.5	Liang17-9	3	1.00	0.6758	33 501	7
11	1.5	−181.5	Kushniruk17-J4-19∗	3	0.99	0.4585	26 148	6
12	70.5	−244.0	Antoja12-GCSIII-13	3	1.00	0.3995	12,169	3
13	66.5	−170.5	GMG 1	3	1.00	0.3706	7728	8
14	−106.0	−223.5	Antoja12-12	3	1.00	0.3537	4289	3
15	**88.5**	**−202.0**	**DR3G-15**	**3**	**0.55**	**0.2564**	**7782**	**This work**
16	−25.5	−183.5	HR1614∗	3	1.00	0.2453	18 636	1,5,7
17	105.5	−234.0	Antoja12-16	3	1.00	0.2380	2750	3
18	34.0	−149.0	ηCep	3	1.00	0.1813	4299	3,5
19	88.0	−169.5	GMG 3	3	0.98	0.1229	3701	8
20	52.0	−254.0	Zhao09-9∗	3	1.00	0.1210	16 252	2
21	−51.0	−285.5	GMG 4	3	1.00	0.0884	1913	8
22	−22.0	−147.5	Antoja12-17	3	1.00	0.0835	3123	3
23	**−56.0**	**−166.0**	**DR3G-23**	**3**	**0.53**	**0.0549**	**3649**	**This work**
24	−135.0	−219.5	GMG 7	3	1.00	0.0412	563	8
25	**4.0**	**−152.0**	**DR3G-25**	**2**	**0.97**	**0.0359**	**5007**	**This work**
26	**−80.0**	**−161.5**	**DR3G-26**	**2**	**1.00**	**0.0204**	**1355**	**This work**
27	127.0	−231.0	GMG 8	3	1.00	0.0204	662	8
28	−37.0	−135.5	Antoja12-19∗	2	0.68	0.0203	1445	3
29	−93.0	−184.5	Bobylev16-23∗	1	0.99	0.0178	2395	5
30	**104.0**	**−199.5**	**DR3G-30**	**1**	**0.72**	**0.0150**	**2897**	**This work**
31	**−131.0**	**−182.0**	**DR3G-31**	**3**	**0.93**	**0.0150**	**404**	**This work**
32	−75.5	−124.5	GMG 13	2	0.76	0.0140	463	8
33	**−65.5**	**−131.5**	**DR3G-33**	**2**	**0.64**	**0.0102**	**696**	**This work**
34	**79.0**	**−141.5**	**DR3G-34**	**1**	**0.69**	**0.0081**	**1,258**	**This work**
35	119.0	−197.0	GMG 20	1	0.91	0.0069	983	8
36	**−83.5**	**−111.5**	**DR3G-36**	**1**	**0.49**	**0.0067**	**266**	**This work**
37	**−97.0**	**−136.0**	**DR3G-37**	**1**	**0.95**	**0.0056**	**327**	**This work**
38	**139.5**	**−190.5**	**DR3G-38**	**1**	**0.98**	**0.0049**	**321**	**This work**
39	−71.5	−281.0	GMG 10	1	0.90	0.0048	934	8
40	73.0	−276.5	GMG 11	0	1.00	0.0044	1113	8
41	**−25.5**	**−99.5**	**DR3G-41**	**0**	**0.68**	**0.0028**	**271**	**This work**
42	−20.5	−90.5	GMG 16	0	0.64	0.0011	202	8
43	**−86.0**	**−279.5**	**DR3G-43**	**0**	**0.71**	**0.0001**	**375**	**This work**
44	**15.0**	**−117.5**	**DR3G-44**	**0**	**0.99**	**−0.0004**	**595**	**This work**
45	**−87.0**	**−227.0**	**DR3G-45**	**0**	**1.00**	**−0.0011**	**10,406**	**This work**
46	−4.0	−113.5	GMG 17	0	0.75	−0.0011	520	8
47	−40.5	−115.5	GMG 22	0	0.83	−0.0019	495	8

multiple components, and at larger scales (Fig. 3) the groups merge together. While some of the small-scale features are interesting to explore in future works, the goal of this work is to compare with the existing studies of moving groups, so we will focus on the $j = 4$ scale below.

3.1 Detected moving groups in the Solar neighbourhood

From the $j = 4$ WT image, we are able to detect 47 moving groups listed in Table 1. Fig. 1 shows the 2D histogram (Panel a) as well as the resultant wavelet coefficients and extrema (Panel b). Both panels show the locations of significant maxima as red crosses, while Panel b

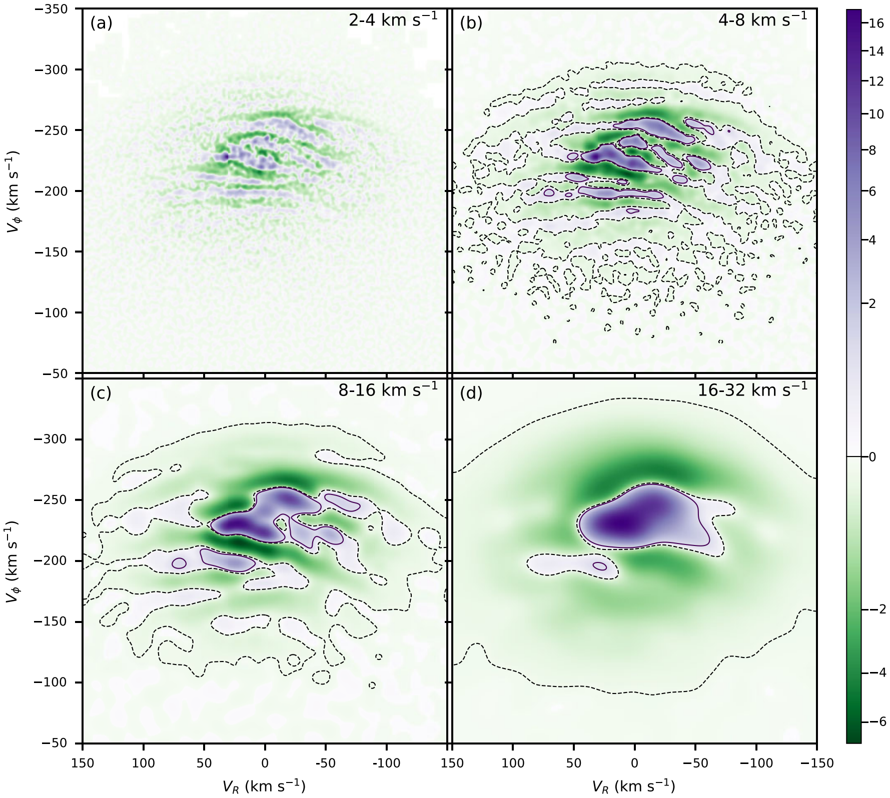

Figure 3. Wavelet coefficient values across the kinematic plane for the SN at various wavelet scales using *Gaia* DR3. Panel (a) corresponds to a scale of $j = 2$ increasing to a scale of $j = 5$ in Panel (d). Given our bin size of 0.5 km s^{-1}, these correspond to physical sizes of 2 km s^{-1} up to 32 km s^{-1} (see labels in figure). Contours are shown at the 5 and −0.1 per cent (dashed) level (except for Panel (a)).

also shows significant minima as blue crosses. The identified moving groups are also shown in Fig. 4, which shows only the overdensities with their corresponding ID number (column 1 in Table 1). The purple and green shaded regions in Fig. 1 b show the positive and negative wavelet coefficients, respectively. While our results for DR3 are in general very consistent with DR2 (shown in Fig. 1c), the most significant differences arise from the restriction on the minimum number of stars for a detected maximum. As discussed above, at least three stars are required for relative maxima, and four stars are required for relative minima in order for consistent significance determination. This cut-off was not implemented in previous works, and for easier comparison with R18, it is disabled in our analysis of the DR2 data below.

We are able to detect 15 candidate overdensities in addition to finding five previously detected groups that were not detected in R18: Kushniruk17-J4-19 (Kushniruk et al. 2017), HR1614, Zhao09-9 (Zhao et al. 2009), Bobylev16-23 (Bobylev & Bajkova 2016), and Antoja12-19 (Antoja et al. 2012). Our 15 candidate groups are numbered with a ‘DR3G’ (Data Release 3 Group) prefix in Table 1. Of our 15 candidate groups discovered, six meet the confidence level criteria (CL ≥ 2), seven meet the Monte Carlo criteria ($P_{\rm MC} > 0.8$), and three groups meet both criteria (Groups 25, 26, and 31 in Table 1). Group 25 lies within Arcturus, and Groups 26 and 31 are in regions without much substructure at low $V_{\rm R}$. These groups are circled in Fig. 1 a and b.

To compare our wavelet method with previous works, we have reproduced the steps of R18. Following their selection of *Gaia* DR2 data, our code is able to detect all the top 24 groups listed in their Table 3. We also find 11 of the remaining 20 groups (all of which were new detections not matching any previously known moving group). In addition to the groups found in R18, our wavelet code detects six previously identified groups: Kushniruk17-J5-2, Kushniruk17-J4-19 (Kushniruk et al. 2017), Dehnen98-11 (Dehnen 1998), HR1614, Zhao09-9 (Zhao et al. 2009), Antoja12-19, and Antoja12-15 (Antoja et al. 2012).

There are also 33 detected overdensities that don’t overlap with any of the groups listed in Table 3 or C.1 in R18, however only 3 of these meet the confidence level and Monte Carlo criteria (Groups 30, 39, and 49 in Table A1). Groups 39 and 49 use fewer than three stars to calculate the wavelet coefficient, which is below our cut-off in the DR3 data. Group 30 is detected in the DR3 data as well (Group 25 in Table 1) slightly shifted but it remains significant and robust against the Monte Carlo simulations.

3.2 Moving groups across the disc

One of the most valuable aspects of automated WTs is the ability to quickly and easily detect overdensities and underdensities for an arbitrary data set. We have used this to analyse different bins of *Gaia* DR3 data to track moving groups throughout Galactocentric radius.

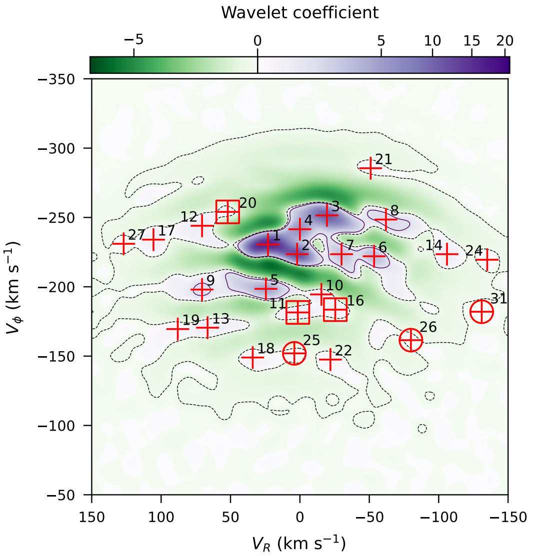

Figure 4. As Fig. 1 b with only maxima shown and numbered by ID as listed in Table 1. Again, only maxima with confidence level ≥2 and $P_{\rm MC} > 0.8$ are plotted, with circles enclosing the three new group candidates and squares around the three groups not previously seen within *Gaia* data.

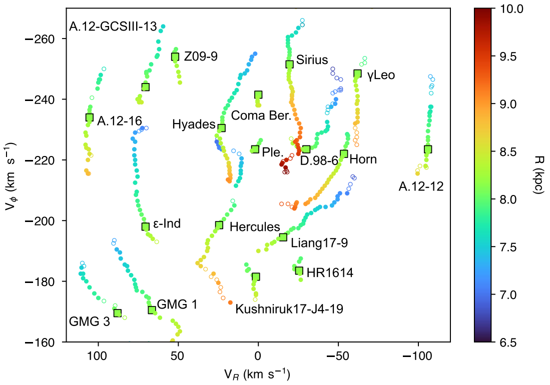

Figure 5. The $V_{\rm R}$–V_ϕ kinematic plane with the locations of detected moving groups shown as a function of radii. The locations of the peaks of the moving groups are shown between radii of 6.5 and 10.0 kpc with radius represented by colour. The filled and empty circles represent those peaks with $P_{\rm MC} \geq 0.8$ and <0.8, respectively. The green square points are the locations of the moving groups in the SN region ($8.05 < R < 8.25$ kpc).

Table 2. Radial extent of the moving groups shown in Fig. 5. The first column lists the ID corresponding to the groups in Table 1. Note that we found that Sirius extends to the maximum radius of 10 kpc, so it could extend further outwards.

	Name	$r_{\rm min}$ (kpc)	$r_{\rm max}$ (kpc)	Extent (kpc)
3	Sirius	7.45	10.00∗	2.55
5	Hercules	6.95	9.25	2.30
1	Hyades	7.20	9.05	1.85
7	Dehnen98-6	6.75	8.35	1.60
10	Liang17-9	6.85	8.40	1.55
6	Dehnen98-14 (Horn)	7.85	9.30	1.45
9	ϵInd	7.00	8.40	1.40
14	Antoja12-12	7.30	8.65	1.35
13	GMG 1	7.25	8.55	1.30
17	Antoja12-16	7.65	8.85	1.20
8	γLeo	7.85	9.05	1.20
12	Antoja12-GCSIII-13	7.55	8.50	0.95
19	GMG 3	7.40	8.25	0.85
11	Kushniruk17-J4-19	7.95	8.50	0.55
20	Zhao09-9	8.00	8.40	0.40
4	Coma Berenices	8.15	8.50	0.35
16	HR1614	7.95	8.25	0.30
2	Pleades	8.00	8.20	0.20

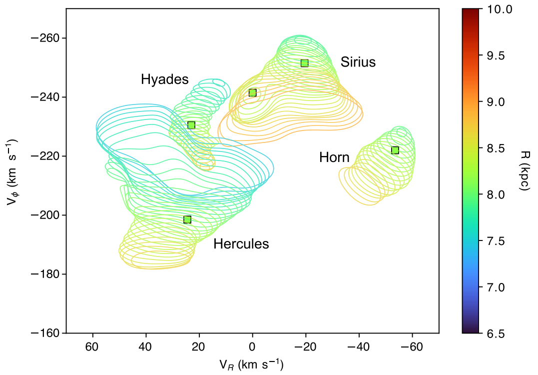

Figure 6. As in Fig. 5, except each moving group is designated by contours of constant wavelet coefficient. Note that the axis limits are different from Fig. 5. This allows us to see how the shapes of the groups vary as a function of radius. Note only four groups are displayed here to maintain clarity.

We selected 70 radial bins centred on R ranging from 6.5 to 10 kpc with a bin size of 0.2 kpc.

For each bin, we run the WT and determine the locations and significance of each overdensity. By plotting each detected peak on the kinematic plane, we can track the evolution of the moving groups throughout the Galactic disc. This is shown in Fig. 5 (some extraneous detections not associated with a continuous stream have been removed). Each dot is a detected peak coloured by its Galactocentric radius. The moving groups in the SN are shown as square markers and are labelled. Here we can clearly see that many of the detected moving groups extend $\gtrsim$1 kpc radially throughout the Galactic disc. The tracked groups with their radial extents are listed in Table 2. We also note that there are four groups with very limited radial extent (<0.5 kpc): Coma Berenices, HR1614, Pleiades, and Zhao09-9. A discussion of the differences between these and the radially extended groups is included in Section 4.

3.2.1 *Shapes of moving groups in the kinematic plane*

In addition to simply detecting the peaks of overdensities, the WT evaluates the wavelet coefficients across the entire image (shown as green and purple shaded regions in Fig. 1 b and c). We can then look at the shape of the moving groups in kinematic space by plotting contours of constant wavelet coefficient. We have also performed this analysis as a function of radius and the results are shown in Fig. 6. Note that while the contour levels are consistent across radius within a single group (e.g. all contours for the Hercules group are

10 per cent of the maximum wavelet coefficient at each radius), the contour levels vary from group to group (e.g. the contours for Sirius are at the 40 per cent level whereas the contours for Hyades are at the 90 per cent level). This allows for optimum visualization of groups with different wavelet coefficient values, however this means that the relative size between groups in this figure does not have meaning. The main purpose of this figure is to show how the kinematics of individual groups changes with radius.

For example, as we progress towards the Galactic Centre, we can see that Hercules covers a larger portion of the kinematic plane. Therefore, at smaller radii, the percentage of stars in the Hercules stream increases. Converesely, as we progress towards the outer disc, Hercules tends to disappear. We see a similar but inverse trend with Sirius. At smaller Galactocentric radii, the contours around Sirius shrink and eventually vanish, but as we progress past the SN and beyond into the outer disc, Sirius grows to cover a significant portion of the kinematic plane.

4 DISCUSSION

Our WT code, *MGwave*, performs 2D wavelet transformations with the goal of detecting statistically significant circular overdensities and underdensities at varying scales. This is distinct from many recent WT analyses of the SN kinematic plane. R18 don't include a minimum star count cut-off, and thus detect many more fringe overdensities that we consider not significant against Poisson noise. Yang et al. (2021) use a bivariate WT to detect features in the V versus $\sqrt{U^2 + 2V^2}$ space, and they utilize a Gaussian mixture model with Monte Carlo sampling to generate a smooth background distribution to compare against. Bernet et al. (2022) explore the $V_{\rm R}$–V_ϕ plane by performing a one-dimensional WT on slices in $V_{\rm R}$. By linking peaks in the 1D WT with neighbouring $V_{\rm R}$ bins, they detect arches in the kinematic plane analogous to those found in R18.

While previous works have analysed moving groups through radius (e.g. R18; Antoja et al. 2018; Fragkoudi et al. 2019; Bernet et al. 2022), they have focused on the variation in the locations of the peak overdensities (e.g. Figs 5, 7). Our Fig. 6 shows that the WT can provide much richer information than simply the location of the extrema. The contours of these groups and how they evolve with radius and azimuth can be informative on the properties of the non-axisymmetric features of the Galactic disc. Because many of these groups are so extended in radius, we know that they are not local, transient structures, but large-scale features of the MW disc. Their extent indicates that these moving groups are likely formed through the gravitational effects of the MW's non-axisymmetric features.

The MW's bar and spiral arms and their associated resonances have long been used to explain the origin of moving groups. The specific resonances that are able to form the groups depend on the bar model (e.g. Hercules can be formed by the outer Lindblad resonance of a short bar or by the corotation resonance of a longer bar). However, recent works seem to indicate that a long bar with pattern speed of $\sim$40 km s^{-1} kpc^{-1} is consistent with both direct observations (Clarke et al. 2019; Sanders et al. 2019), and can explain many of the moving groups that we detect in the SN (Monari et al. 2019; D'Onghia & L. Aguerri 2020; Trick et al. 2021). D'Onghia & L. Aguerri (2020) proposed a model with a bar of length 4.5 kpc and pattern speed of 40 km s^{-1} kpc^{-1}, and showed that Hercules is reproduced by stars at the corotation resonance with the bar. In this scenario, Hercules' stars are librating around the bar's Lagrange points L4/L5 thus leading to a stream of stars with coherent velocity (slower than the Sun) in the SN (see their Figure 4). As shown in our Figs 5 and 6, Hercules is extended in radius around the SN. Moreover, Fig. 6 shows that Hercules grows to cover a significant portion of the kinematic plane for $R < R_\odot$. In the models of D'Onghia & L. Aguerri (2020), the bar's corotation radius is around 6 kpc, so if the stars of Hercules are formed through trapping at corotation, we would expect Hercules to become more significant at smaller radii, consistent with the data.

The model of a long bar presented in Monari et al. (2019) also shows that five regions of in the kinematic plane correspond to resonances with the bar. To compare with this work, we performed the WT on the *Gaia* DR3 data transformed into U, V, W coordinates.[3] Fig. 8 shows this WT image and the corresponding overdensities numbered by their corresponding group in Table 1. The coloured lines show the locations of the resonances from the long bar model of Monari et al. (2019): red, blue, and purple correspond to the 2:1 (OLR), 4:1 (outer ultra-harmonic resonance, OUH), and 6:1 resonances, while the green and yellow lines mark the corotation resonance. In addition to Hercules being stars at corotation with the bar, the authors find that the Hat aligns with OLR, Sirius with the OUH, and the Horn with the 6:1 resonances. All of these groups are shown in our Fig. 5 and are still prominent across Galactocentric radius. Moreover, Fig. 6 shows Sirius becoming more prominent at larger radii (opposite of Hercules). For a bar with a pattern speed of $\sim$40 km s^{-1} kpc^{-1}, the location of the OUH is at 8.5–9 kpc (D'Onghia & L. Aguerri 2020). Therefore, we expect more stars comprising Sirius as we look towards the outer Galactic disc, which is shown in the data.

There are several other groups that we detect with significant radial extent, many of which are also identified being in resonance with the bar (Monari et al. 2019) shown in Fig. 8. Antoja12-16, Antoja12-GCSIII-13, γLeo, Zhao09-9, and possibly Antoja12-12 fall on the OUH resonance along with Sirius. Dehnen98-6 aligns well with the 6:1 resonance along with the Horn. Finally, ϵInd and Hercules and Liang17-9 are all at corotation.

This leaves four groups with radial extent greater than 0.5 kpc unaccounted for: the Hyades, GMG 1, GMG 3, and Kushniruk17-J4-19. While Hyades doesn't seem to have formed through any known bar resonance, works focusing on the kinematic signatures of spiral arm resonances have been able to reproduce Hyades along with several other features of the SN kinematic plane (Michtchenko et al. 2018; Barros et al. 2020; including low -V_ϕ features like GMG 1,3, and Kushniruk17-J4-19). However, these models predict that the moving groups are significantly extended in ϕ, and less extended in R. Further work will be required to constrain the groups in ϕ to test this theory. Additionally, our detection of Hyades throughout a large range of Galactocentric radii could be simply the detection of the main mode in each neighbourhood. We expect a smooth evolution of V_ϕ across radius with stars being mostly on circular orbits. Therefore, while the main mode might be identified as Hyades locally, at different radii, the detected peak could simply be the bulk motion of the disc. This would also explain why it is unique in its double slope in $V_{\rm R}$ in Fig. 1 (discussed further below).

There are also five groups detected that have small radial extent ($<$0.5 kpc): Coma Berenices, the Pleiades, HR1614, Boblyev16-23, and DR3G-21 (which was briefly discussed above). It has been shown previously that Coma Berenices and the Pleiades are open clusters (e.g. Odenkirchen, Soubiran & Colin 1998; Tang et al. 2018; Heyl, Caiazzo & Richer 2022). Fig. 5 and Table 2 corroborates this result by showing that these objects are detected only locally within the SN. While HR1614 has long been considered an open

---

[3] We used the default Galactic coordinate frame in the Astropy PYTHON module (Astropy Collaboration et al. 2022)

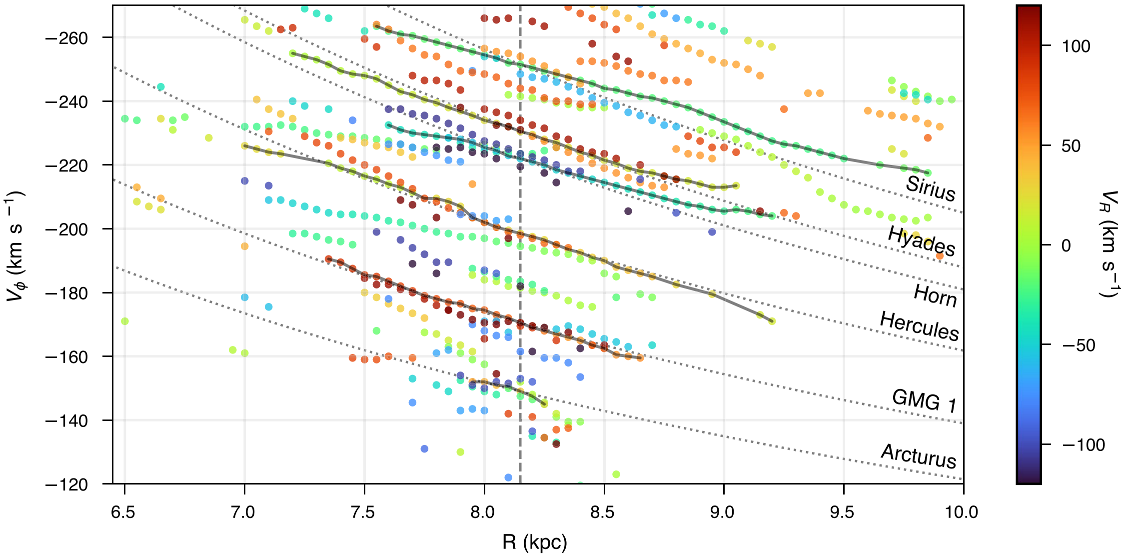

Figure 7. The variation of V_ϕ with R. Each point is a detected overdensity in the kinematic plane coloured by V_R. The SN is shown with a vertical dashed line at 8.15 kpc. The continuous streams associated with Sirius, Hyades, the Horn, Hercules, GMG 1, and Arcturus are shown as connected points, and curves of constant angular momentum are shown as dashed lines. Note that only those points with $P_{MC} \geq 0.8$ are shown.

cluster (e.g. Feltzing & Holmberg 2000; De Silva et al. 2007) recent works suggest that its metallicity spread matches that of the MW disc population (Kushniruk et al. 2020). Further investigation is required to unravel the true origin of HR1614.

We apply our *MGwave* code to *Gaia* DR3. Fig. 7 shows the azimuthal velocity of the known moving groups of the SN displayed as a function of Galactocentric radius. Each moving groups is coloured by radial velocity. Bernet et al. (2022) showed the same plot but using a 1D WT technique applied to the previous *Gaia* data release (eDR3). The authors found that all major groups deviate from the predicted $V_\phi \propto R^{-1}$. Note that our results obtained with DR3 seem to confirm a deviation from the constant angular momentum curve (dashed line) for most of the known moving groups with the exception of GMG 1. This general outcome is not surprising as the constant angular momentum curve is expected for small radial oscillations of the stars within the epicycle approximation. Therefore, a deviation is expected for highly eccentric stars. Additionally, even with the improved data of *Gaia* DR3, we are unable to trace our groups much inwards of $R \sim 7$ kpc while Bernet et al. (2022) find groups extending down to 5 kpc. This discrepancy could be due to the difference in the wavelet method (searching for arches versus search for circular features). However it is also clear that the data become less accurate at these radii. While the WT is able to detect significant overdensities even at these small radii, many of them have small P_{MC} values indicating that they are not robust detections against the *Gaia* errors (see Section 2.4).

Our Fig. 5 shows that there is also a significant variation in V_R with R. Notably most groups have a shift in V_R as they move in radius, however the direction of this shift (the slope of the connected points in Fig. 5) can be positive, negative, or both. Four groups have strong positive slopes (e.g. Liang17-9, Dehnen98-6, the Horn, and the majority of Hercules) in which they move to larger V_R at higher radii, and three have strong negative slopes (GMG 3, GMG 1, and Kushniruk17-J4-19) with smaller V_R at higher radii. Several other groups have slight slopes in either direction, or multiple slopes at different radii. Notably, Hyades moves to larger V_R until it reaches the SN at which point it decreases again, and Hercules, Sirius, and Dehnhn98-6 exhibit breaks or strong variations in the slope throughout radius.

For the positive slope groups, the inner portion (smaller R) has an inward velocity relative to the centroid, while the outer portion (larger R) has an outward velocity. This will inevitably lead to the group spreading out and possibly breaking apart. Consequently, negative slope groups exhibit the opposite trend and therefore are condensing. These two different behaviours of groups could possibly indicate environmental effects operating at different radii like tidal effects, but further analysis of the data in comparison with simulations is required to fully explore the possible causes of these slopes.

Looking at the larger structure of the WT images, previous works (e.g. Skuljan, Hearnshaw & Cottrell 1999; Antoja et al. 2008) have noted several distinct kinematic branches visible in the V_R–V_ϕ plane. Note that these features have been explored at smaller scales that those discussed throughout most of this paper. In the following paragraphs, we will be referencing our results from the WT with scale $j = 3$. Antoja et al. (2008) found that these branches are inclined at an angle of $\sim 16^\circ$, and the four most prominent are aligned with the Hercules, Hyades/Pleiades, Coma Berenices, and Sirius groups. These branches are still clearly visible in our data (see Fig. 1c), however thanks to *Gaia*'s immense volume of data, we can now view these structures across larger ranges of V_R. Gaia Collaboration et al. (2018) and R18 extended these branches into arches, most of which follow constant kinetic energy. In contrast to the uniformly inclined branches found in Antoja et al. (2008), *Gaia*'s increased data has elongated and straightened out many of these structures. However, as discussed in R18, several of the arches are still inclined to one side; notably their A5 and A7 corresponding to Hyades/Pleiades and Coma Berenices. Several models have shown that these arches of constant kinetic energy can be formed through

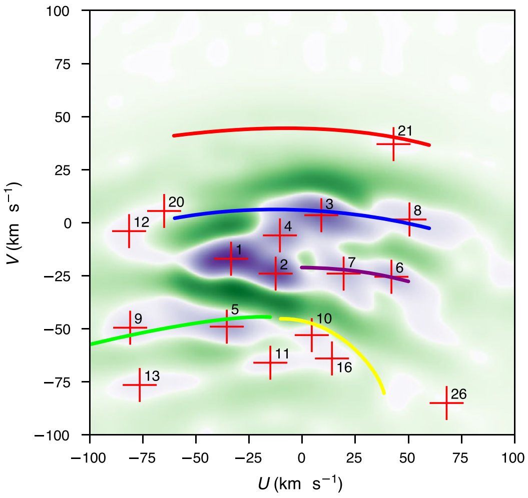

Figure 8. The $j = 4$ wavelet transformed image of the SN in U, V, W coordinates. Coordinates were transformed from *Gaia* DR3 source data to the Astropy default Galactic coordinate system (in the cartesian representation). The overdensities are numbered as in Fig. 4. Overlaid are the bar resonance locations from Monari et al. (2019) (c.f. their Figure 9). 'The green and yellow lines correspond to the corotation, the red line to the 2:1 (OLR) resonance for the m = 2 mode,. . . the blue line to the 4:1 resonance of the m = 4 mode, and the purple line to the 6:1 resonance of the m = 6 mode.

phase mixing (Minchev et al. 2009; Gómez et al. 2012, R18), which could play a role in the formation of the moving groups as well. However further investigation is required to constrain this paradigm.

In this study, we have returned to the method of Antoja et al. (2008) of summing the wavelet transformed image along V_R to obtain a histogram as a function of V_ϕ. We have explored this histogram both with and without the 16° rotation that was performed in Antoja et al. (2008). These results can be seen in Fig. 9 (Panels (a) show the results without rotation and Panels (b) include the 16° rotation). With the increased volume of data provided by *Gaia*, we can see that while the Hyades/Pleiades, Coma Berenices, and Sirius branches do still appear inclined (and we see γLeo appear in the rotated histogram as well), there are several other structures that do not follow this trend. Most dramatically, we see three strong peaks in the non-rotated histogram corresponding to various components of Hercules. By looking at the wavelet plane, the horizontal alignment of these branches is clearly visible, while in the rotated plane (bottom panels) Hercules becomes muddled. We also see slight peaks in the non-rotated histogram corresponding to the Hat at very high V_ϕ and Arcturus at very low V_ϕ. While some of the these tilted features have been reproduced in past simulations (e.g. Antoja et al. 2009; Hunt et al. 2018; Barros et al. 2020), further modelling is required to determine their source specifically in the context of a long, slow bar.

5 CONCLUSIONS

The wavelet transform is an invaluable tool for precise, quantitative analysis of images. Our new code, *MGwave*, is an open-source PYTHON module for performing wavelet transformations on 2D images while detecting extrema and determining their significance. Additionally, we have implemented Monte Carlo sampling to propagate errors and uncertainties through to the wavelet extrema detections. *MGwave* is able to reproduce the findings of R18 (using *Gaia* DR2 data) and improves upon previous codes by detecting underdensities in addition to overdensities, and implementing a minimum n cutoff in the significance calculation.

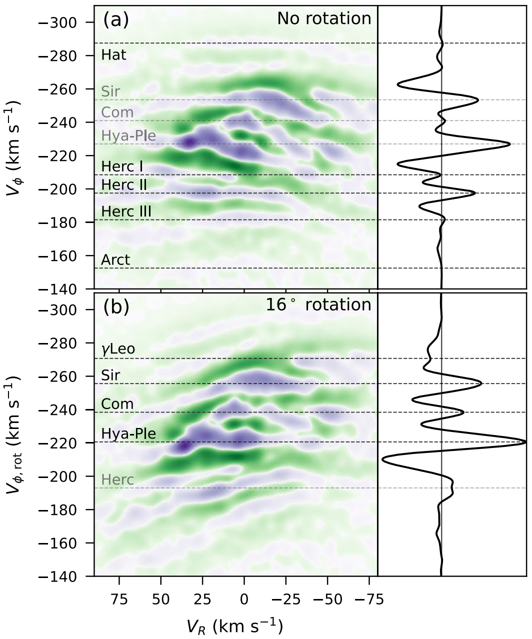

Figure 9. The wavelet plane and its histogram along V_ϕ for $j = 3$, structures of size 4–8 km s^{-1}. In the top panels, the wavelet plane is identical to that shown in Fig. 3, however on the bottom panels, the plane has been rotated by 16° counter-clockwise. As done in Antoja et al. (2008), this is to better align the Hyades–Pleiades, Coma Berenices, and Sirius overdensities with the x-axis. However, as shown in the top panel, there are several structures (Hercules, the Hat, and Arcturus) which do not match this distinctive rotation. The line plots on the right show the sums of wavelet coefficients across all V_R as a function of V_ϕ. These panels show that the Hyades–Pleiades, Coma Berenices, and Sirius overdensities are stronger and more prominent after a 16° rotation of the plane, whereas Hercules, the Hat, and Arcturus are stronger without the rotation.

We performed the WT on *Gaia* DR3 data to detect moving groups in the kinematic plane (V_R–V_ϕ) of the SN (Fig. 1). With the improved data, we have several main conclusions:

(i) We have detected three new statistically significant candidate moving groups: one within Arcturus, and two in regions without much substructure at low V_R.

(ii) We have been able to perform the WT on different regions within the MW disc. Exploring the structure of the kinematic plane in sections of the disc ranging in Galactocentric radius from 6.5 to 10 kpc, we find that the majority of the moving groups detected within the SN are radially extended (Fig. 5). The elongation of these groups indicate that they are dynamical structures possibly outcome by the effects of resonances of the MW's non-axisymmetric features.

(iii) By mapping contours in wavelet space, we can track the variation in the kinematic shape of these groups through radius (Fig. 6). We find Hercules becoming more prominent towards the Galactic Centre in agreement with the models of D'Onghia & L. Aguerri (2020) that predicted that Hercules is comprised of stars at corotation with the bar.

(iv) Mapping WT contours also reveals an opposite trend for Sirius, it gets more prominent towards the outer disc. This is consistent with Sirius being in resonance with the OUH located outside the solar radius (Monari et al. 2019).

Gaia DR3 has greatly expanded our view of the MW. By looking at the kinematics of moving groups throughout a significant portion of the disc, we can unravel many of the mysteries of the MW's non-axisymmetric features and their associated resonances.

ACKNOWLEDGEMENTS

The authors thank the anonymous referee for their constructive comments on the manuscript. The authors also thank Eric Slezak for useful discussions on the implementation of the wavelet significance calculations. This work made use of Astropy:[4] a community-developed core PYTHON package and an ecosystem of tools and resources for astronomy (Astropy Collaboration et al. 2013, 2018, 2022).

DATA AVAILABILITY

The data underlying this article will be shared on reasonable request to the corresponding author.

REFERENCES

Alves J. et al., 2020, Nature, 578, 237
Antoja T. et al., 2012, MNRAS, 426, L1
Antoja T. et al., 2018, Nature, 561, 360
Antoja T., Figueras F., Fernández D., Torra J., 2008, A&A, 490, 135
Antoja T., Valenzuela O., Pichardo B., Moreno E., Figueras F., Fernández D., 2009, ApJ, 700, L78
Asano T., Fujii M. S., Baba J., Bédorf J., Sellentin E., Portegies Zwart S., 2020, MNRAS, 499, 2416
Astropy Collaboration et al., 2013, A&A, 558, A33
Astropy Collaboration et al., 2018, AJ, 156, 123
Astropy Collaboration et al., 2022, ApJ, 935, 167
Bailer-Jones C., Rybizki J., Fouesneau M., Demleitner M., Andrae R., 2020, Gaia eDR3 lite distances subset, VO resource provided by the GAVO Data Center, http://dc.zah.uni-heidelberg.de/tableinfo/gedr3dist.litewithdist (accessed September 6, 2022)
Bailer-Jones C. A. L., Rybizki J., Fouesneau M., Demleitner M., Andrae R., 2021, AJ, 161, 147
Barros D. A., Pérez-Villegas A., Lépine J. R. D., Michtchenko T. A., Vieira R. S. S., 2020, ApJ, 888, 75
Bernet M., Ramos P., Antoja T., Famaey B., Monari G., Al Kazwini H., Romero-Gómez M., 2022, A&A,667, A116
Bobylev V. V., Bajkova A. T., 2016, Astron. Lett., 42, 90
Clarke J. P., Wegg C., Gerhard O., Smith L. C., Lucas P. W., Wylie S. M., 2019, MNRAS, 489, 3519
Craig P., Chakrabarti S., Newberg H., Quillen A., 2021, MNRAS, 505, 2561
D'Onghia E., L. Aguerri J. A., 2020, ApJ, 890, 117
Da Rocha C., Mendes de Oliveira C., 2005, MNRAS, 364, 1069
Da Rocha C., Ziegler B. L., Mendes de Oliveira C., 2008, MNRAS, 388, 1433
De Silva G. M., Freeman K. C., Bland-Hawthorn J., Asplund M., Bessell M. S., 2007, AJ, 133, 694
Debattista V. P., Gerhard O., Sevenster M. N., 2002, MNRAS, 334, 355
Dehnen W., 1998, AJ, 115, 2384
Dehnen W., 2000, AJ, 119, 800
Eggen O. J., 1996, AJ, 112, 1595
Einasto J. et al., 2011, A&A, 531, A75
Feltzing S., Holmberg J., 2000, A&A, 357, 153
Fragkoudi F. et al., 2019, MNRAS, 488, 3324
Fujii M. S., Bédorf J., Baba J., Portegies Zwart S., 2019, MNRAS, 482, 1983
Gaia Collaboration et al., 2016, A&A, 616, A11
Gaia Collaboration et al., 2018, A&A, 616, A11
Gaia Collaboration, Vallenari A., Brown A., Prusti T., 2022a, preprint (arXiv:2208.00211)
Gaia Collaboration, Drimmel R., Romero-Gómez M., Chemin L., Ramos P., Poggio E., Ripepi V., 2022b, preprint (arXiv:2206.06207)
Girardi M., Escalera E., Fadda D., Giuricin G., Mardirossian F., Mezzetti M., 1997, ApJ, 482, 41
Gómez F. A., Minchev I., Villalobos Á., O'Shea B. W., Williams M. E. K., 2012, MNRAS, 419, 2163
Hergt L., Amara A., Brandenberger R., Kacprzak T., Réfrégier A., 2017, JCAP, 06, 004
Heyl J., Caiazzo I., Richer H. B., 2022, ApJ, 926, 132
Hunt J. A. S., Hong J., Bovy J., Kawata D., Grand R. J. J., 2018, MNRAS, 481, 3794
Kushniruk I., Schirmer T., Bensby T., 2017, A&A, 608, A73
Kushniruk I., Bensby T., Feltzing S., Sahlholdt C. L., Feuillet D., Casagrande L., 2020, A&A, 638, A154
Liang X. L., Zhao J. K., Oswalt T. D., Chen Y. Q., Zhang L., Zhao G., 2017, ApJ, 844, 152
Michtchenko T. A., Lépine J. R. D., Pérez-Villegas A., Vieira R. S. S., Barros D. A., 2018, ApJ, 863, L37
Minchev I., Quillen A. C., Williams M., Freeman K. C., Nordhaus J., Siebert A., Bienaymé O., 2009, MNRAS, 396, L56
Monari G., Kawata D., Hunt J. A. S., Famaey B., 2017, MNRAS, 466, L113
Monari G., Famaey B., Siebert A., Wegg C., Gerhard O., 2019, A&A, 626, A41
Odenkirchen M., Soubiran C., Colin J., 1998, New A, 3, 583
Pérez-Villegas A., Portail M., Wegg C., Gerhard O., 2017, ApJ, 840, L2
Price-Whelan A., 2018, adrn/pyia: v0.2(accessed July 1, 2021)
Quillen A. C., Dougherty J., Bagley M. B., Minchev I., Comparetta J., 2011, MNRAS, 417, 762
Ramos P., Antoja T., Figueras F., 2018, A&A, 619, A72
Reid M. J. et al., 2014, ApJ, 783, 130
Reid M. J. et al., 2019, ApJ, 885, 131
Rogers K. K., Peiris H. V., Leistedt B., McEwen J. D., Pontzen A., 2016, MNRAS, 463, 2310
Sanders J. L., Smith L., Evans N. W., 2019, MNRAS, 488, 4552
Sanz J. L., Argüeso F., Cayón L., Martínez-González E., Barreiro R. B., Toffolatti L., 1999, MNRAS, 309, 672
Schönrich R., Binney J., Dehnen W., 2010, MNRAS, 403, 1829
Skuljan J., Hearnshaw J. B., Cottrell P. L., 1999, MNRAS, 308, 731
Slezak E., de Lapparent V., Bijaoui A., 1993, ApJ, 409, 517
Starck J.-L., Murtagh F., 1994, A&A, 288, 342
Starck J.-L., Murtagh F., 2006, Astronomical Image and Data Analysis (Astronomy and Astrophysics Library). Springer-Verlag, Berlin, Heidelberg
Starck J.-L., Murtagh F., Bijaoui A., 1998, Image Processing and Data Analysis. The Multiscale Approach. Cambridge University Press, Cambridge, UK
Tang S.-Y., Chen W. P., Chiang P. S., Jose J., Herczeg G. J., Goldman B., 2018, ApJ, 862, 106
Thulasidharan L., D'Onghia E., Poggio E., Drimmel R., Gallagher John S. I., Swiggum C., Benjamin R. A., Alves J., 2021, A&A, 660, L12
Trick W. H., 2022, MNRAS, 509, 844
Trick W. H., Fragkoudi F., Hunt J. A. S., Mackereth J. T., White S. D. M., 2021, MNRAS, 500, 2645
van der Walt S. et al., 2014, PeerJ, 2, e453
Waskom M. L., 2021, J. Open Source Softw., 6, 3021
Xia Q., Liu C., Xu Y., Mao S., Gao S., Hou Y., Jin G., Zhang Y., 2015, MNRAS, 447, 2367
Yang Y., Zhao J., Zhang J., Ye X., Zhao G., 2021, ApJ, 922, 105
Zhao J., Zhao G., Chen Y., 2009, ApJ, 692, L113
Zhao J.-K., Zhao G., Chen Y.-Q., Tan K.-F., Gao M.-T., Yang M., Zhang Y., Hou Y.-H., 2015, Res. Astron. Astrophys., 15, 1378

---

[4] http://www.astropy.org

Zhao J. K., Zhao G., Chen Y. Q., Oswalt T. D., Tan K. F., Zhang Y., 2014, ApJ, 787, 31

SUPPORTING INFORMATION

Supplementary data are available at *MNRAS* online.

Fig1_movie.mp4

Please note: Oxford University Press is not responsible for the content or functionality of any supporting materials supplied by the authors. Any queries (other than missing material) should be directed to the corresponding author for the article.

APPENDIX

Table A1. Moving groups detected using our new wavelet transform on *Gaia* DR2 data. Compare with those found in R18. Groups marked with an asterisk (∗) are those that have been previously discovered but were not present in the wavelet analysis of R18. Bold lines are groups newly discovered in this work. Columns 5–9 list the output of our analysis: CL denotes the confidence level that a given group is not due to Poisson noise (see Section 2.3); P_{MC} gives the percentage of Monte Carlo simulations in which the peak appeared when varying the stellar velocities within Gaia errors (see Section 2.4); Wavelet gives the magnitude of the wavelet coefficient at the peak; *n* lists the number of stars used in computing the wavelet coefficient; Stars lists the number of stars in a region of kinematic space around the peak corresponding to the scale of the wavelet transformation performed (in this case within a circle of radius 16 km s^{-1}).

	V_{R}	V_{ϕ}	Name	CL	P_{MC}	Wavelet	*n*	Stars
1	22.5	−236.0	Hyades	3	1.00	7.6596	394	130 982
2	1.5	−228.5	Pleiades	3	1.00	5.6223	438	162 864
3	−20.0	−256.5	Sirius	3	1.00	4.9166	376	87 694
4	−1.0	−247.0	Coma Berenices	3	1.00	3.0033	538	130 122
5	24.0	−203.5	Hercules II	3	1.00	2.0458	157	58 368
6	−54.0	−227.5	Dehnen98-14	3	1.00	1.5060	141	44 723
7	−31.0	−228.5	Dehnen98-6	3	1.00	1.2256	293	90 548
8	−64.0	−253.5	γLeo	3	1.00	0.5601	68	20 072
9	70.5	−203.0	ϵInd	3	1.00	0.5349	43	17 400
10	−53.0	−258.0	Kushniruk17-J5-2∗	3	0.93	0.4607	112	23 082
11	−16.5	−199.5	Liang17-9	3	1.00	0.2771	109	38 112
12	70.0	−250.5	Antoja12-GCSIII-13	3	1.00	0.1807	24	9614
13	64.0	−239.0	Dehnen98-11∗	3	0.99	0.1570	61	17 261
14	66.0	−175.5	GMG 1	3	1.00	0.1473	20	9255
15	−7.0	−187.5	GMG 2	3	1.00	0.1293	102	31 186
16	**−68.0**	**−210.0**	**Unknown**	**3**	**0.47**	**0.1248**	**54**	**22 073**
17	−108.5	−229.0	Antoja12-12	3	1.00	0.1208	11	3764
18	106.5	−239.5	Antoja12-16	3	1.00	0.1111	6	2233
19	2.5	−186.0	Kushniruk17-J4-19∗	3	0.60	0.1077	76	33 118
20	47.0	−178.0	Arifyanto05	3	0.86	0.0898	34	14 832
21	88.5	−174.5	GMG 3	3	0.98	0.0708	6	3 953
22	36.0	−153.5	ηCep	3	0.93	0.0602	12	5041
23	−51.0	−291.0	GMG 4	3	1.00	0.0529	6	1345
24	−28.5	−189.0	HR1614∗	1	0.81	0.0314	59	20 115
25	−26.0	−150.0	Antoja12-17	3	1.00	0.0311	7	3087
26	48.0	−259.5	Zhao09-9∗	0	1.00	0.0292	71	14 006
27	−56.0	−176.0	GMG 5	3	1.00	0.0276	14	5037
28	106.0	−272.5	GMG 6	3	0.99	0.0254	1	318
29	−134.0	−225.5	GMG 7	3	1.00	0.0173	1	535
30	**2.5**	**−157.5**	**Unknown**	**2**	**0.98**	**0.0170**	**14**	**6182**
31	**−14.0**	**−153.0**	**Unknown**	**1**	**0.37**	**0.0159**	**17**	**4305**
32	129.0	−237.5	GMG 8	3	1.00	0.0159	1	496
33	**112.5**	**−155.0**	**Unknown**	**3**	**0.68**	**0.0123**	**3**	**1078**
34	**−88.0**	**−233.0**	**Unknown**	**0**	**1.00**	**0.0120**	**40**	**10 436**
35	73.0	−282.0	GMG 11	2	1.00	0.0112	4	770
36	−108.0	−152.0	GMG 12	3	0.99	0.0106	1	345
37	125.5	−175.0	GMG 14	3	1.00	0.0104	3	654
38	−78.0	−130.5	GMG 13	2	0.97	0.0101	4	500
39	**83.5**	**−143.5**	**Unknown**	**2**	**0.97**	**0.0095**	**2**	**1285**
40	**−79.0**	**−166.5**	**Unknown**	**1**	**0.99**	**0.0092**	**8**	**1671**
41	−1.0	−120.0	GMG 17	1	0.97	0.0090	6	709
42	−24.0	−91.0	GMG 16	3	1.00	0.0085	1	219
43	**71.0**	**−142.5**	**Unknown**	**2**	**0.49**	**0.0082**	**3**	**1431**
44	**−59.0**	**−138.0**	**Unknown**	**3**	**0.44**	**0.0070**	**1**	**1019**

Table A1 – *continued*

	$V_{\rm R}$	V_ϕ	Name	CL	$P_{\rm MC}$	Wavelet	n	Stars
45	−39.0	−139.0	Antoja12-19∗	1	0.90	0.0067	6	1568
46	13.5	−82.0	GMG 19	3	0.85	0.0067	1	158
47	122.0	−202.5	GMG 20	1	0.96	0.0065	5	837
48	**−96.5**	**−158.5**	**Unknown**	**1**	**0.78**	**0.0063**	**4**	**636**
49	**−66.5**	**−108.0**	**Unknown**	**3**	**0.97**	**0.0061**	**1**	**298**
50	−42.5	−119.0	GMG 22	1	1.00	0.0040	2	591
51	**125.0**	**−146.5**	**Unknown**	**1**	**0.49**	**0.0037**	**2**	**472**
52	**−26.5**	**−107.0**	**Unknown**	**1**	**0.83**	**0.0033**	**1**	**384**
53	**137.5**	**−164.5**	**Unknown**	**1**	**0.66**	**0.0028**	**1**	**381**
54	**−98.5**	**−135.0**	**Unknown**	**1**	**0.88**	**0.0028**	**1**	**304**
55	**136.5**	**−138.0**	**Unknown**	**1**	**0.93**	**0.0025**	**2**	**248**
56	**−127.5**	**−184.5**	**Unknown**	**0**	**0.89**	**0.0022**	**2**	**486**
57	−70.5	−174.0	Antoja12-15∗	0	0.42	0.0022	6	3081
58	**109.0**	**−118.5**	**Unknown**	**1**	**0.60**	**0.0021**	**1**	**203**
59	**140.0**	**−83.0**	**Unknown**	**1**	**0.96**	**0.0020**	**1**	**42**
60	**50.5**	**−106.0**	**Unknown**	**1**	**0.54**	**0.0017**	**1**	**260**
61	**−47.5**	**−88.0**	**Unknown**	**0**	**0.28**	**0.0016**	**2**	**180**
62	**72.5**	**−78.0**	**Unknown**	**1**	**0.22**	**0.0015**	**1**	**113**
63	−109.0	−340.0	GMG 27	1	0.98	0.0012	1	6
64	47.0	−342.0	GMG 26	0	0.73	0.0012	2	13
65	**129.5**	**−125.0**	**Unknown**	**1**	**0.87**	**0.0011**	**1**	**200**
66	**−114.5**	**−320.0**	**Unknown**	**1**	**0.96**	**0.0011**	**1**	**8**
67	**−35.5**	**−74.0**	**Unknown**	**0**	**0.75**	**0.0011**	**2**	**139**
68	**80.0**	**−116.5**	**Unknown**	**0**	**0.58**	**0.0010**	**3**	**306**
69	**−25.0**	**−122.0**	**Unknown**	**0**	**0.88**	**0.0010**	**3**	**837**
70	**−24.0**	**−326.5**	**Unknown**	**0**	**0.69**	**−0.0000**	**1**	**36**
71	**−62.0**	**−153.0**	**Unknown**	**0**	**0.21**	**−0.0012**	**5**	**1823**
72	**−102.5**	**−183.5**	**Unknown**	**0**	**0.97**	**−0.0018**	**7**	**1449**
73	**−56.5**	**−161.5**	**Unknown**	**0**	**0.25**	**−0.0022**	**8**	**2953**
74	**−113.5**	**−199.0**	**Unknown**	**0**	**0.85**	**−0.0026**	**8**	**1330**

This paper has been typeset from a TEX/LATEX file prepared by the author.

MNRAS **000**, 1–5 (2023) Preprint 9 May 2023 Compiled using MNRAS LaTeX style file v3.0

Constraining the Milky Way bar length using Hercules and *Gaia* DR3

Scott Lucchini[1†], Elena D'Onghia[1,2], J. Alfonso L. Aguerri[3,4]
[1]*Department of Physics, University of Wisconsin - Madison, Madison, WI, USA*
[2]*Department of Astronomy, University of Wisconsin - Madison, Madison, WI, USA*
[3]*Instituto de Astrofísica de Canarias; C/ Vía Láctea s/n, 38200, La Laguna, Spain*
[4]*Departamento de Astrofísica, Universidad de La Laguna, E-38206 La Laguna, Spain*
[†]*lucchini@wisc.edu*

Accepted XXX. Received YYY; in original form ZZZ

ABSTRACT

The distribution of moving groups in the solar neighborhood has been used to constrain dynamical properties of the Milky Way for decades. Unfortunately, the unique bimodality between the main mode (Hyades, Pleiades, Coma Berenices, and Sirius) and Hercules can be explained by two different bar models – via the outer Lindblad resonance of a short, fast bar, or via the corotation resonance of a long, slow bar. In this work, we break this degeneracy by using *Gaia* DR3 to explore the variation of Hercules across Galactic azimuth. We find that Hercules increases in V_ϕ and becomes stronger as we move towards the minor axis of the bar, and decreases in V_ϕ and becomes weaker as we move towards the major axis of the bar. This is in direct agreement with theoretical predictions of a long, slow bar model in which Hercules is formed by the corotation resonance with stars orbiting the bar's L4/L5 Lagrange points.

Key words: Galaxies – Stars – Galaxy: kinematics and dynamics < The Galaxy – stars: kinematics and dynamics < Stars – Galaxy: structure < The Galaxy – (Galaxy:) solar neighbourhood < The Galaxy

1 INTRODUCTION

Being embedded within the Milky Way (MW) makes it difficult to observe its properties. We must use indirect methods to determine the distribution of mass, and corresponding nonaxisymmetric features in our Galaxy. Specifically, the properties of our own Galactic bar – an oblong stellar overdensity at the center of our Galaxy – are still not known for sure. There have been two main models proposed throughout the past decade, one in which we have a short bar that rotates very quickly ($R_{\rm bar} \sim 3$ kpc, $\Omega_p \sim 55$ km s^{-1} kpc^{-1}; Dehnen 2000; Debattista et al. 2002; Monari et al. 2017; Fragkoudi et al. 2019), and one in which we have a long bar that rotates relatively slowly ($R_{\rm bar} \sim 5$ kpc, $\Omega_p \sim 40$ km s^{-1} kpc^{-1}; Pérez-Villegas et al. 2017; Monari et al. 2019a; Asano et al. 2020; D'Onghia & L. Aguerri 2020).

Originally, the short, fast bar scenario proposed by Dehnen (2000) was supported by an application of the Tremaine-Weinberg method (Tremaine & Weinberg 1984) modified for use with radial velocities in which Debattista et al. (2002) used OH/IR stars to measure a pattern speed of $\Omega_p \sim 60$ km s^{-1} kpc^{-1}. The gas motions measured in H I Galactic longitude vs velocity (lv-diagram) in the inner Galaxy were also consistent with a fast bar scenario (Englmaier & Gerhard 1997; Fux 1999). However, star counts have indicated that the bar may be long, extending near or past the proposed corotation resonance of a fast bar (Benjamin et al. 2005; Wegg et al. 2015; Clarke et al. 2019). Moreover, recent studies using more accurate velocity data have found lower values of $\Omega_p \sim 40$ km s^{-1} kpc^{-1}consistent with a longer bar (Sanders et al. 2019; Bovy et al. 2019). A more thorough parameter-space exploration using 2D isothermal simulations in external potentials have also shown that slow bars actually provide the best match to all the lv-diagram features (Sormani et al. 2015).

An additional constraint on the properties of the MW's nonaxisymmetric features came from the motions (in full 3D) of the stars near the Sun (e.g. Dehnen 1998; Antoja et al. 2012). How these stars cluster in velocity space (moving groups) contains a wealth of information about the evolution of our Galaxy's disk and the forces these stars are feeling. Specifically, the bimodality in the Galactocentric azimuthal velocity versus radial velocity plot has been one of the main features models have attempted to reproduce. The main mode (at $V_\phi \sim 230$ km s^{-1}) contains the moving groups of Hyades, Pleiades, Coma Berenices, and Sirius, while Hercules (at $V_\phi \sim 200$ km s^{-1}) is separated by a gap (a strong underdensity).

This bimodality has been explained through resonances of the MW's bar. Since the bar contributes a nonaxisymmetric gravitational potential, it has an associated pattern speed, as discussed above. Over time, the bar perturbs the stars to align the frequencies of the stellar orbits with the bar's frequency. These stars are "in resonance" with the bar. A bar's strongest resonances are the corotation resonance (CR; in which the stellar and bar frequencies match exactly), and the inner and outer Lindblad resonances (ILR and OLR; in which the star completes two radial oscillations for every orbit around the galaxy). Unfortunately, both proposed models of the Galactic bar can produce this bimodality through different resonances. For a short bar, the OLR falls just inside the solar neighborhood and is able to trap stars to form Hercules (Dehnen 2000; Fragkoudi et al. 2019). For a long bar, the CR is able to create Hercules through stars orbiting the bar's Lagrange points (Pérez-Villegas et al. 2017; D'Onghia & L. Aguerri 2020). Both models agree with the observations near the Sun,

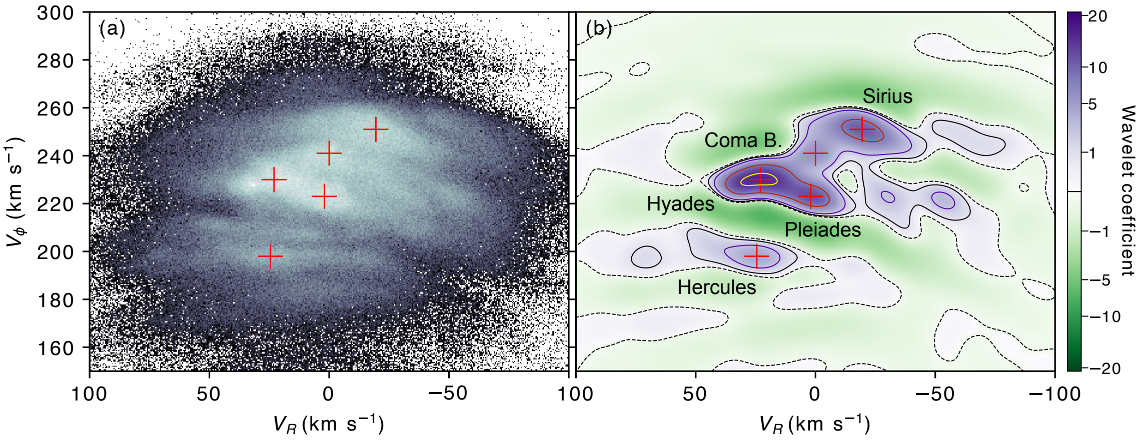

Figure 1. Panel a shows the 2D histogram of all the solar neighborhood stars in the $V_R - V_\phi$ kinematic plane using *Gaia* DR3 with a bin size of 0.5 km s^{-1}. Panel b shows the resultant wavelet transformed image at a scale of 8-16 km s^{-1}. The purple and green regions depict the relative strength of the positive and negative wavelet coefficients, respectively. Contours are shown at the -0.1% (dashed), 5%, 15%, 50%, and 90% levels. The red markers denote the locations of the five major moving groups as detected by our wavelet transformation – Hyades, Pleiades, Coma Berenices, Sirius, and Hercules.

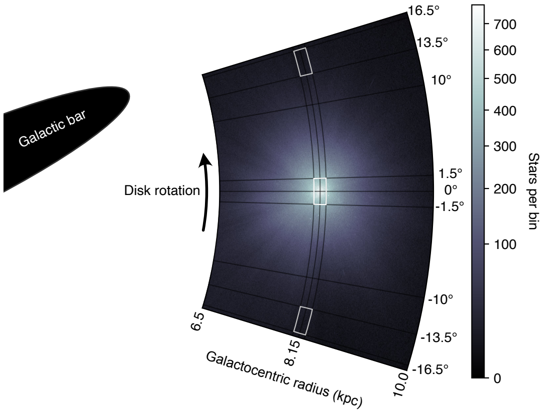

Figure 2. *Gaia* DR3 dataset in the context of the MW disk. This region extends from Galactocentric radius $R = 6.5$ kpc to $R = 10$ kpc, and from median azimuth $\phi = -15°$ to $\phi = 15°$. An approximation of the Galactic bar is also shown. The MW disk is rotating counter-clockwise (in the direction of $+\phi$), and the solar neighborhood is trailing behind the major axis of the bar. The white boxes also show the size of our neighborhood regions, extending 0.2 kpc in R and 3° in ϕ.

however as we move throughout the Galactic disk their predictions change.

With *Gaia*'s latest data release (Data Release 3; Gaia Collaboration et al. 2016, 2018, 2022a), we can finally begin to differentiate between these two models by looking at full 3D stellar motions across the Galactic disk. In this paper, we explore how Hercules changes as we move around the disk in azimuth, breaking the degeneracy between these two models for the MW's bar.

2 METHODS

We follow the methods outlined in Lucchini et al. (2023) (hereafter Paper I) for *Gaia* selection and analysis using the wavelet transformation. Figure 1 shows the solar neighborhood velocity plane and its corresponding wavelet transformed image. The red marks denote the five most significant classical moving groups as detected by local maxima in the wavelet image. Starting with the 33,653,049 stars with radial velocities and geometric distances computed by Bailer-Jones et al. (2021) (Bailer-Jones et al. 2020), we transformed the six-dimensional data into Galactocentric cylindrical coordinates[1]. See Figure 2 for a schematic defining our coordinate system with R increasing away from the Galactic center, ϕ increasing in the direction of rotation, and Z increasing towards the Galactic north pole. With the Sun located at $\phi_\odot = 0°$, this means the major axis of the Milky Way's bar is at $\phi \sim 20°$ (Gaia Collaboration et al. 2022b). Figure 2 also shows the extent of the *Gaia* DR3 data that we used: $6.5 < R < 10$ kpc, and $-15° < \phi < 15°$. As in Paper I, we used the PYIA[2] code to propagate the errors (including correlations) from the source properties (right ascension, declination, proper motions, and radial velocities) to the final properties (Galactocentric cylindrical coordinates; Price-Whelan 2018).

For the analysis of Hercules in this paper, we broke up this region into 31 overlapping bins in ϕ of size $\phi = 3°$, $R = 0.2$ kpc, and $Z = 1$ kpc, centered on $R = 8.15$ kpc and $Z = 0$, spaced every 1° (e.g. ranges of $(-16.5°, -13.5°)$, $(-15.5°, -12.5°)$, etc). The solar neighborhood bin contains nearly 10^6 stars, while the bins at the edge of our sample (±15°) contain more than 10^4 stars.

We use the wavelet transform code, *MGwave*[3] (described in Paper I), to analyze the velocity distributions of these different neighborhoods. Each velocity plane histogram ($V_R - V_\phi$) is transformed using

---

[1] We assume the Sun is located at $R_\odot = 8.15$ kpc, $\phi_\odot = 0°$, and $Z_\odot = 5.5$ pc, with velocity $(V_R, V_\phi, V_Z) = (10.6, 246.7, 7.6)$ km s^{-1}.

[2] `https://github.com/adrn/pyia`

[3] `https://github.com/DOnghiaGroup/MGwave`

the Starlet transform (Starck & Murtagh 1994; Starck & Pierre 1998; Starck & Murtagh 2006) and the relative significance of the results are evaluated with respect to Poisson noise (Slezak et al. 1993) and errors in the source *Gaia* data (using Monte Carlo simulations). In this paper, we used a wavelet scale of 8-16 km s^{-1} to best identify the Hercules group. See Paper I for more details on the wavelet code and methodology.

3 RESULTS

We track Hercules across the Galactic disk using *Gaia* DR3. In particular, we are looking for variations in the size and strength of the Hercules moving group as we vary the azimuth. Figure 3 shows the velocity plane for five different neighborhoods: $\phi = \pm 15°$, $\pm 9°$, and $0°$ (corresponding to the solar neighborhood shown in Figure 1). These angles were chosen to show the full extent of usable data from *Gaia* DR3 ($\pm 15°$, where the number of stars per bin reaches $\sim 10^4$), while showing an intermediate region in which Hercules is just beginning to merge with the main mode ($-9°$). The upper panels are towards the major axis of the bar ($+\phi$), and the lower panels are towards the minor axis of the bar ($-\phi$). The left column shows the $V_R - V_\phi$ histogram of all the stars in the specified neighborhood. The center column shows the wavelet transform of these data in which purple represents overdensities and green represents underdensities (as in Figure 1). The right-most column shows a plot of wavelet coefficient as a function of V_ϕ obtained by summing the wavelet transformed image along V_R (the "1D summed wavelet histogram"). From these plots, we are able to clearly see the location of Hercules in each neighborhood as the peak in this histogram around $V_\phi \sim 200$ km s^{-1}.

Figure 4 summarizes the properties of Hercules as a function of azimuth. Figure 4a shows the azimuthal velocity of Hercules as a function of ϕ. This is identified by the location of the peak in the 1D summed wavelet histogram (right panels in Figure 3). A linear fit to V_ϕ of Hercules versus azimuth gives $V_{\phi,\mathrm{Herc}} = -0.74\,\phi + 198$ (with $V_{\phi,\mathrm{Herc}}$ in km $\mathrm{s}^{-1}$and ϕ in degrees) decreasing from 211 km s^{-1}at $\phi = -15°$ to 190 km s^{-1}at $\phi = +15°$. Figure 4b shows the strength of the Hercules overdensity relative to the main mode. This is measured by the value of the peak in the 1D summed wavelet histogram corresponding to Hercules. A larger value means that the overdensity is stronger. In Figure 3c, we also show the percentage of stars that constitute Hercules in each neighborhood. This is determined by selecting all the stars within ± 15 km $\mathrm{s}^{-1}$of the V_ϕ of Hercules (Figure 4a) and dividing by the total number of stars in the given bin. Examples of this 30 km s^{-1}region are shown bounded by the dashed horizontal lines in Figure 3. In the solar neighborhood, Hercules constitutes 20.0% of stars. As we move towards the bar's major axis (upwards in Figure 3), this percentage decreases to 15.0% at $\phi = 15°$. As we move towards the bar's minor axis (downwards in Figure 3), this percentage increases to 35.7% at $\phi = -15°$.

If Hercules was formed through interaction with the Galactic bar's outer Lindblad resonance, we would expect its strength to be relatively constant across azimuth (see Figure 12, left panel, in Fragkoudi et al. 2019). However, if the corotation resonance is responsible for Hercules, its member stars would be orbiting around the Galactic bar's L4/L5 Lagrange points (Pérez-Villegas et al. 2017; D'Onghia & L. Aguerri 2020) located along the bar's minor axis. Therefore, we should expect to see a larger population of stars in Hercules as we approach L4/L5 (in the $-\phi$ direction; see Figure 4 from D'Onghia & L. Aguerri 2020). The behavior identified here in *Gaia* DR3, mimics exactly the predictions of D'Onghia & L. Aguerri (2020) (see their

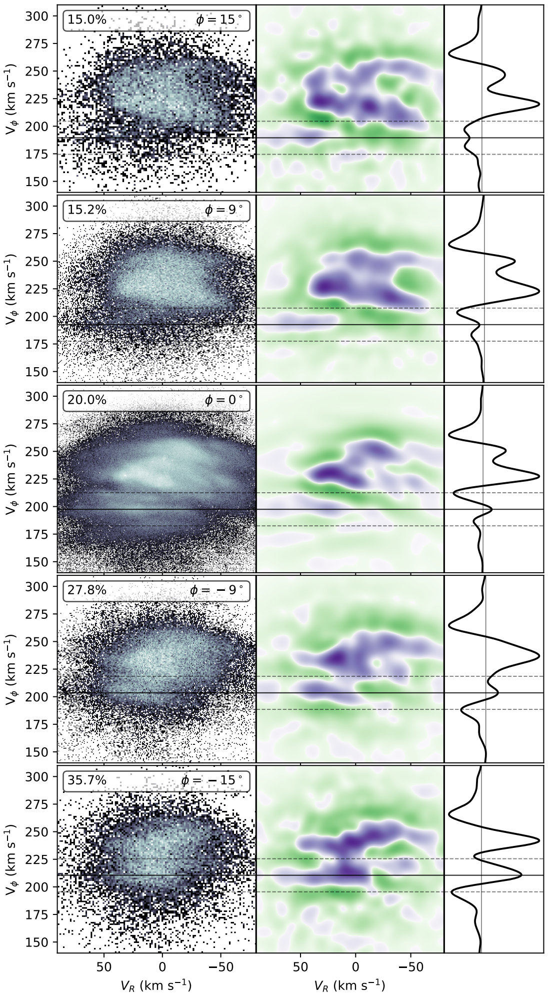

Figure 3. The velocity plane and its wavelet transformation for five neighborhoods located at $\phi = -15°$, $-9°$, $0°$, $9°$, and $15°$. $\phi = 0°$ corresponds to the location of the Sun, and positive ϕ is in the direction of rotation, while negative ϕ is counter to the direction of rotation. The left column shows the $V_R - V_\phi$ histogram for each region, the center column shows the wavelet transformed kinematic plane as in Figure 1, and the right column shows the wavelet histogram summed along V_R. In the left column, the number of bins in the histogram has been scaled to the total number of stars such that we use 200 bins in each dimension at $\phi = \pm 15°$, and we use 600 bins at $\phi = 0°$. Hercules is denoted by a horizontal line across each plot in a row, identified as a peak in the summed wavelet histogram (right column). Additionally, the percentage of stars that constitute Hercules (defined as all stars within 15° of Hercules' V_ϕ) is printed in the top right of the left plots. In the direction of rotation (i.e. $+\phi$, towards the major axis of the MW bar) Hercules diminishes and the percentage drops, while moving towards the minor axis of the bar ($-\phi$, towards the Lagrange points) Hercules grows and merges in with the main mode. We additionally see that V_ϕ of Hercules increases as we approach the Lagrange points, as predicted by models (D'Onghia & L. Aguerri 2020; Monari et al. 2019b; see also Figure 4a).

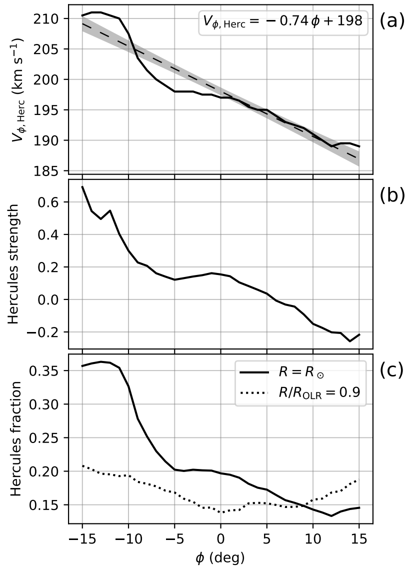

Figure 4. Properties of Hercules as a function of azimuth. The top panel shows the mean V_ϕ for the Hercules group as detected using the location of the peak in the wavelet histogram. A linear fit with the 95% confidence interval is shown as a dashed line and grey shading. The best fit equation is shown in the top right. The middle panel shows the relative strength of the Hercules overdensity normalized against the strength of the main mode. This is the value of the peak in the summed 1D wavelet histogram (see right panels in Figure 3). The bottom panel shows the percentage of stars in the given neighborhood that have V_ϕ values within 15 km s^{-1}of Hercules. The dotted line shows the percentage of stars within 175−205 km s^{-1}at R = 12 kpc (such that R/R_{OLR} = 0.9, as in Dehnen 2000). At the OLR, we see no variation in intensity as a function of ϕ. These three plots clearly show that in the $-\phi$ direction (towards the bar's minor axis), Hercules sees an increase in angular momentum and becomes stronger and more dominant as predicted by the long, slow bar model (D'Onghia & L. Aguerri 2020).

Figure 8). Along the bar's major axis, Hercules diminishes (for both the fast and slow bar scenarios). However, along the minor axis, we are able to discriminate between these two models. For the short, fast bar, Hercules should remain subdominant and separated from the main mode. While in the long, slow bar model, Hercules should become extremely prominent, even merging with the main mode, which is what we see in the data.

Figures 4b and c show that Hercules increases in strength and fraction as we move towards the bar's minor axis ($-\phi$). Figure 4c also shows the fraction of stars within 175−205 km s^{-1}at R = 12 kpc (corresponding to R/R_{OLR} = 0.9, as in Dehnen 2000) to show the angular dependence due to the OLR. As expected, the fraction of stars trapped by the OLR (at R = 12 kpc) is relatively constant in azimuth, while at the solar radius, there is a sharp increase in the $-\phi$ direction, indicating that Hercules is comprised of stars trapped at the Lagrange points.

Moreover, as shown in Monari et al. (2019b), we would expect the angular momentum of Hercules to vary with azimuth. Figure 3 shows that the Hercules overdensity in the data changes its value of V_ϕ with angle decreasing from V_ϕ = 211 km s^{-1}at $\phi = -15°$, to V_ϕ = 190 km s^{-1}at $\phi = +15°$. Monari et al. (2019b)[4] predicted a slope of −0.96 km s^{-1}deg^{-1}, whereas here the data show a slope of -0.74 ± 0.04 km s^{-1}deg^{-1}. This difference could be due to additional effects of spiral arms not included in the model of Monari et al. (2019b). However, it is clear that the slope is < 0, consistent with Hercules being formed by corotation, not the OLR.

4 CONCLUSIONS

Here we have used *Gaia* DR3 to track the properties of Hercules through Galactic azimuth. Exploring $-15° < \phi < 15°$ either side of the Sun, we see that there is a strong variation in the azimuthal velocity and strength of Hercules. Hercules becomes stronger and constitutes a larger fraction of stars per bin as we move towards the minor axis of the bar ($-\phi$). This is in direct agreement with predictions of a long, slow bar model in which Hercules is formed through stars trapped at corotation, orbiting the L4/L5 Lagrange points. This corroborates recent direct observations of the bar from *Gaia* DR3 (Gaia Collaboration et al. 2022b).

With the next release from *Gaia*, DR4, we can expect further significant improvements using this technique. While DR3 extended our view out to $\phi = \pm 15°$, we can hope to get similar signal to noise results out to $\phi = \pm 30°$ and beyond. This will allow us to get a direct measurement of the bar angle with respect to the Sun's position, by looking for a minimum in Hercules' strength and V_ϕ.

ACKNOWLEDGEMENTS

J.A.L.A. has been founded by The Spanish Ministerio de Ciencia e Innovacion by the project PID2020-119342GB-I00. This work made use of Astropy:[5] a community-developed core Python package and an ecosystem of tools and resources for astronomy (Astropy Collaboration et al. 2013, 2018, 2022).

DATA AVAILABILITY

The data underlying this article will be shared on reasonable request to the corresponding author.

---

[4] Monari et al. (2019b) give a value of −8 km s^{-1}kpc deg^{-1} for the fit of the angular momentum versus azimuth. In their model the Sun is located at 8.2 kpc giving us a predicted slope of $-8/8.2 = -0.96$ km s^{-1}deg^{-1}.

[5] http://www.astropy.org

REFERENCES

Antoja T., et al., 2012, MNRAS, 426, L1
Asano T., Fujii M. S., Baba J., Bédorf J., Sellentin E., Portegies Zwart S., 2020, MNRAS, 499, 2416
Astropy Collaboration et al., 2013, A&A, 558, A33
Astropy Collaboration et al., 2018, AJ, 156, 123
Astropy Collaboration et al., 2022, apj, 935, 167
Bailer-Jones C., Rybizki J., Fouesneau M., Demleitner M., Andrae R., 2020, Gaia eDR3 lite distances subset, VO resource provided by the GAVO Data Center, `http://dc.zah.uni-heidelberg.de/tableinfo/gedr3dist.litewithdist`
Bailer-Jones C. A. L., Rybizki J., Fouesneau M., Demleitner M., Andrae R., 2021, AJ, 161, 147
Benjamin R. A., et al., 2005, ApJ Letters, 630, L149
Bovy J., Leung H. W., Hunt J. A. S., Mackereth J. T., García-Hernández D. A., Roman-Lopes A., 2019, MNRAS, 490, 4740
Clarke J. P., Wegg C., Gerhard O., Smith L. C., Lucas P. W., Wylie S. M., 2019, MNRAS, 489, 3519
D'Onghia E., L. Aguerri J. A., 2020, ApJ, 890, 117
Debattista V. P., Gerhard O., Sevenster M. N., 2002, MNRAS, 334, 355
Dehnen W., 1998, AJ, 115, 2384
Dehnen W., 2000, AJ, 119, 800
Englmaier P., Gerhard O., 1997, MNRAS, 287, 57
Fragkoudi F., et al., 2019, MNRAS, 488, 3324
Fux R., 1999, A&A, 345, 787
Gaia Collaboration et al., 2016, A&A, 595, A1
Gaia Collaboration et al., 2018, A&A, 616, A11
Gaia Collaboration Vallenari A., Brown A., Prusti T., 2022a, A&A
Gaia Collaboration Drimmel R., Romero-Gómez M., Chemin L., Ramos P., Poggio E., Ripepi V., 2022b, arXiv e-prints, p. arXiv:2206.06207
Lucchini S., Pellett E., D'Onghia E., Aguerri J. A. L., 2023, MNRAS, 519, 432
Monari G., Kawata D., Hunt J. A. S., Famaey B., 2017, MNRAS, 466, L113
Monari G., Famaey B., Siebert A., Wegg C., Gerhard O., 2019a, A&A, 626, A41
Monari G., Famaey B., Siebert A., Bienaymé O., Ibata R., Wegg C., Gerhard O., 2019b, A&A, 632, A107
Pérez-Villegas A., Portail M., Wegg C., Gerhard O., 2017, ApJ Letters, 840, L2
Price-Whelan A., 2018, adrn/pyia: v0.2, doi:10.5281/zenodo.1228136, `https://doi.org/10.5281/zenodo.1228136`
Sanders J. L., Smith L., Evans N. W., 2019, MNRAS, 488, 4552
Slezak E., de Lapparent V., Bijaoui A., 1993, ApJ, 409, 517
Sormani M. C., Binney J., Magorrian J., 2015, MNRAS, 454, 1818
Starck J.-L., Murtagh F., 1994, A&A, 288, 342
Starck J.-L., Murtagh F., 2006, Astronomical Image and Data Analysis (Astronomy and Astrophysics Library). Springer-Verlag, Berlin, Heidelberg
Starck J. L., Pierre M., 1998, A&A Supplement, 128, 397
Tremaine S., Weinberg M. D., 1984, ApJ Letters, 282, L5
Wegg C., Gerhard O., Portail M., 2015, MNRAS, 450, 4050